Three-Dimensional Body Volume Measurement From Two-Dimensional Images

Towards A Smartphone Application

Division of Biomedical Engineering
Department of Human Biology
Faculty of Health Sciences
University of Cape Town

Master's Dissertation

In partial fulfilment of the requirements for the degree:
MSc in Biomedical Engineering

Prepared by:
Khwezi Majola
MJLKHW001

Supervisor: Dr. Tinashe Mutsvangwa
Co-Supervisors: Prof. Tania Douglas
Prof. Vicki Lambert

January 2020

Declaration

1. I know that plagiarism is wrong. Plagiarism is to use another's work and pretend that it is one's own.
2. I have used the UCT-Harvard for citation and referencing. Each contribution to, and quotation in, this proposal from the work(s) of other people, has been attributed and has been cited and referenced.
3. This report is my own work.
4. I have not allowed, and will not allow, anyone to copy my work with the intention of passing it off as their own work or part thereof

Name: **Khwezi Majola**

Signature: Signed by candidate **Date:** 17 January 2020

Abstract

Obesity poses a public health threat worldwide and is associated with a higher mortality, increased likelihood of diabetes, and an increased risk of cancer. When treating obesity, regular monitoring of metrics such as body mass index (BMI) and waist circumference has been found to result in improved health outcomes for patients. Three-dimensional (3D) scanners provide a useful tool to provide body measurements based on 3D images in obesity management. However, such scanners are often inaccessible due to cost. A smartphone image-based method able to produce 3D images may provide a more accessible measuring tool. As a step towards developing such a smartphone application, this project developed a method for 3D reconstruction of body images from two-dimensional (2D) images, using a full body 3D Gaussian process morphable model (GPMM).

Separate GPMMs were trained to learn the shape of female and male human bodies. Gaussian process regression of the three-dimensional (3D) GPMM models onto two-dimensional (2D) images is performed. Corresponding landmarks on the 3D shapes and in the 2D images are employed in reconstruction. Measurements of body volume, waist circumference and height are then performed to extract information that is useful in obesity management. Different model configurations (shape model with arms; modified shape model with arms; shape model without arms; marginalised shape model without arms; shape model with different landmarks) were used to ascertain the most promising approach for the reconstruction. Each reconstructed body was tested for accuracy using the surface-to-surface distance per vertex, modified Hausdorff distance, and assessment of the measurements. Tests were performed using data from the same dataset used to build the model and generalised data from a different dataset.

In all test cases, the best performing approach used shape models without arms when considering surface distances. However, the surface-to-surface distances errors were larger than those seen in literature. For body measurements, the best performing models varied with different models performing best for different measurements. For the measurements, the errors were larger than the allowable errors and larger than those found in literature. Landmark positions were evaluated separately and found to be imprecise.

There are a few sources that contribute towards the reconstruction errors. Possible sources of error include an inability to interpret pose and landmark position errors. The major recommendations for future work are to use a model that incorporates both shape and pose and to use automatic landmarking methods. Regarding a pathway to a smartphone app, camera parameter information should be considered to improve processing of the images and smartphone orientation information should be considered to correct for distortions due to a tilted phone.

Acknowledgements

I would like to express my gratitude to the following people:

My supervisor Dr Tinashe Mutsvangwa for the guidance and motivation that enabled me to understand this work and complete this research.

My co-supervisor Prof Tania Douglas for the advice that contributed greatly towards the completion of the research.

To Prof Vicki Lambert and Dr Nathaniel Narra for their contribution in developing the proposal.

To my colleagues in the Mi^2d^2 research group for their ideas and critique as well as the laughter and friendship shared throughout.

To the staff, students, and friends from the Division of Biomedical Engineering at the University of Cape Town for creating the wonderful environment for this work to be done.

To my friends who provided many great distractions throughout and an opportunity to get away from it all.

To my loving family without whom I would not be where I am today.

Table of Contents

List of Figures

List of Tables

List of Abbreviations

AP	Anteroposterior
API	Application programming interface
BIA	Bioelectrical impedance analysis
BMI	Body mass index
BV	Body volume
BVI	Body Volume Indicator
CC	Correlated correspondence
CNN	Convolutional neural network
CT	Computed tomography
DXA	Dual-energy X-ray absorptiometry
EXIF	Exchangeable Image File format
GP	Gaussian process
GPMM	Gaussian process morphable model
GPA	Generalized Procrustes analysis
ICC	Intraclass correlation coefficient
ICP	Iterative closest point
IDE	Integrated development environment
ISAK	International Society for the Advancement of Kinanthropometry
ISO	International Organization for Standardization
LAT	Lateral
LED	Light emitting diode
MAD	Mean absolute difference
MCMC	Markov Chain Monte Carlo
MD	Mean difference
MH	Metropolis-Hastings
MRI	Magnetic resonance imaging
PCA	Principal component analysis
PDM	Point distribution model
PPP	Purchasing power parity
SCAPE	Shape completion and animation of people
SMPL	Skinned Multi-Person Linear
SSM	Statistical shape model
WC	Waist circumference

1. Introduction

1.1 Background

Weight gain and obesity pose a public health threat worldwide (World Health Organization, 2000). Since 1980, the obesity rate has doubled in more than 70 countries alongside a general increase in prevalence (GBD Obesity Collaborators, 2017). This imposes direct costs in the form of increased healthcare spending and indirect costs in the form of reduced economic productivity (Dee et al., 2014). That cost is estimated to be R16.4 trillion per year globally and cost is R701 billion per year in South Africa (Discovery Limited, 2017).

Obesity is the accumulation of excess fat in adipose tissue with excess abdominal fat presenting as great a health risk as excess fat (World Health Organization, 2000). Thus, obesity can be diagnosed by assessing fat levels and additional risks can be measured by assessing abdominal fat. Studies measuring the risk of excess fat use techniques such as dual-energy X-ray absorptiometry (DXA), body mass index (BMI), and bioelectrical impedance analysis (BIA) (Brownell & Walsh, 2017). Body mass index is more widely used due to its simplicity and lower cost compared to the other methods (Brownell & Walsh, 2017).

There is a relationship between BMI values and health risks. For example, a high BMI (BMI >25 kg/m^2) is associated with an a higher chance of diabetes (Abramowitz et al., 2018), a greater risk of cancer (Renehan et al., 2008), and a higher mortality (Prospective Studies Collaboration, 2009). The strategies executed to treat and prevent obesity are referred to as obesity management (Plourde & Prud'homme, 2012). Effective management includes a comprehensive analysis of the patient's obesity, an appropriate weight loss plan, and behavioural therapy to address contributing behaviours towards obesity (Yumuk et al., 2015). An analysis of obesity management techniques and found that regular monitoring of BMI and metrics such as waist circumference (WC) improved the patient outcomes (Plourde & Prud'homme, 2012). Patients can measure themselves; however self-reported values contain errors (Bigaard et al., 2005, Spencer, Roddam & Key, 2004, Spencer et al., 2002).

Three-dimensional (3D) scanners have been used in multiple studies to assess the shape and composition and have been relatively accurate (Adler et al., 2017, Jaeschke, Steinbrecher & Pischon, 2015, Koepke et al., 2017, Simenko & Cuk, 2016). However, the cost of 3D scanners is high. The prices of scanners assessed by Tzou et al. (2014) ranged from €1590 to €37000 in June 2013. When converting to rand using purchasing power parity values from OECD (2018), the range is R10283 to R239304. Cheaper scanners are available for R2062 ($400) or less but they are less accurate (Daanen & ter Haar, 2013). The smartphone has a potential as a more accessible method to assess body volume (BV).

Globally, there are 2.5 billion smartphone connections the number is expected to grow further (GSMA Intelligence, 2017b). Health oriented applications (apps) that aim to facilitate weight loss have been shown to be effective (Allen et al., 2013, Chin et al., 2016). Currently 51% of South Africans own a smartphone (Poushter, Bishop & Chwe, 2018). With the an average price of $115 (R700) in 2017 (GSMA Intelligence, 2017a), smartphones are cheaper than some low-cost scanners (see Appendix). Smartphones may therefore be more accessible than scanners. Additionally, patients may already have a smartphone and will not necessarily face additional costs to access scanning capabilities. A smartphone-based solution for body measurement can exploit current levels of smartphone penetration to assist enable obesity management without imposing an additional cost on patients.

This project investigated the development of a system that measures BV from 2D images towards the development of a smartphone application.

1.2 Aim and Objectives

The aim of the project was the development of a GPMM statistical shape model (SSM) that can be used to perform 3D reconstruction from 2D images and measure BV from the reconstructed body. In order to achieve this aim, the following objectives were outlined:

- Develop a database containing 3D scans, anatomical measurements, and 2D images of people.
- Develop a GPMM that describes full body shape.
- Develop a 3D from 2D reconstruction algorithm and algorithms to measure BV, WC, and height.
- Validate the model and evaluate the accuracy of the reconstruction.

1.3 Scope and Limitations

The envisioned complete system would be composed of a frontend and a backend. The frontend would consist of the smartphone application used to take the photos. The backend would consist of the software to perform 3D from 2D reconstruction. This project is only concerned with the development of the backend. The development of the frontend is out of scope for this project. The main reason for the exclusion of the frontend relates to the roles the frontend and backend will play in a fully developed system. The backend is responsible for most of the processing necessary for reconstruction with the frontend mainly serving as an interface to the system. Due to time constraints, it was decided to focus on the backend as it is the core and will enable further development.

Similarly, as the focus of the project was on developing a reconstruction pipeline, existing datasets were identified and used in the development of the backend. Due to time constraints and a lack of access to the necessary resources to collect data, it was decided to not collect data and rather focus on existing datasets.

1.4 Structure of Dissertation

The rest of the dissertation is structured as follows: Chapter 2 presents a review of relevant literature. Chapter 3 outlines the overall methodology and the database used for the project. Chapter 4 outlines the GPMM development. Chapter 5 describes the landmarks used and their reliability. The body measurement methodologies are described in Chapter 6. Chapter 7 presents the 3D reconstruction methodology. Chapter 8 provides a summary of the findings and recommendations for future work.

2. Literature Review

This section describes the literature relevant to the project with descriptions of the importance of body composition assessment as well as describing the various techniques used to assess composition. It then details shape models with descriptions of the underlying mathematics, measures of quality, and the application of shape models in assessing body shape from limited information.

2.1 Body Composition Measurement Techniques

Widely used techniques to measure body composition include dual-energy x-ray absorptiometry (DXA), body mass index (BMI), and bioelectrical impedance analysis (BIA) (Brownell & Walsh, 2017).

2.1.1 Dual-Energy X-Ray Absorptiometry

Dual-energy X-ray absorptiometry is a method for measuring body composition through the use of dual-energy X-rays. According to Lehmann et al. (1981), a high and low energy X-ray pair are used to produce two images that independently characterise differing attenuation components. By combining the images, the mass and composition of known materials can be determined. Figure 2.1 shows a DXA scan being administered. The scanning arm seen above the table moves over the body and is the source of the X-rays.

Figure 2.1: DXA scan being administered. (Image: (Smith, 2011), Licensed under Creative Commons Attribution-Share Alike 3.0 Unported (Creative Commons, 2009))

When used to determine body composition, a high and low energy attenuation pair that correspond to fat mass and fat-free mass are used (Kelly, Berger & Richardson, 1998). Prior et al. (1997) found that DXA produced accurate body composition estimates when using a four-compartment model (4C) considering fat, water, mineral, and protein content. An additional consideration when using DXA is the selection of the machine. Plank (2005) found DXA to be a viable technique for composition measurement. However, they found differences in the values reported by different machines and recommended inter-machine comparison and validation. A concern with DXA is radiation exposure (Wilson et al., 2011).

2.1.2 *Bioelectrical Impedance Analysis*

Bioelectrical impedance analysis involves the application of an alternating current and relies on the principle that at lower frequencies (~1 kHz), electrical currents pass mainly through fat-free mass whilst at higher frequencies (500-800 kHz), they pass through fat-free mass and fat mass (Lukaski et al., 1985). This behaviour can be exploited for body composition assessment by measuring the difference in conductivity when using high and low frequencies. The difference in the values can be used to determine the level of fat tissue mass. Figure 2.2 shows a model for BIA with the electrode placement. The distal red electrodes are used to apply the current and the proximal black electrodes are used to measure the voltage drop across that region. The voltage drops are used in calculating the impedance. The difference between the results when using high and low frequencies are used to assess body composition.

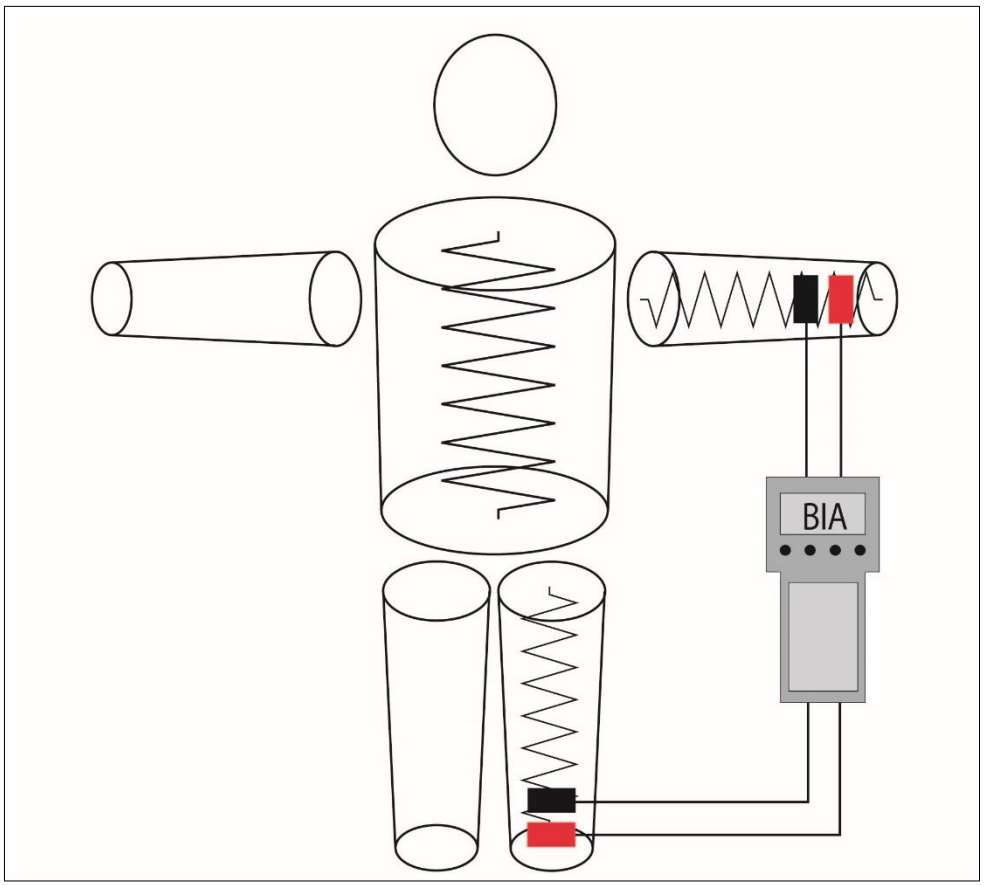

Figure 2.2: BIA cylindrical model electrode placement. (Image adapted from (Engel, 2012), Licensed under Creative Commons Attribution-Share Alike 3.0 Unported (Creative Commons, 2009))

Kyle et al. (2004a) reviewed BIA use and found it to be used widely but lacking a standardised method and appropriate quality controls. They also reported that a variety of equations are used to determine fat-free mass with the appropriateness of the equation dependent on the population, age, or pathology. Bioelectrical impedance analysis is appropriate when the equation used has been validated for the specific population being studied, and inappropriate for studies with diverse populations (Dehghan & Merchant, 2008). Additionally, BIA is appropriate in patients with a stable water and electrolyte balance when using an appropriate, validated BIA equation (Kyle et al., 2004b). An additional consideration when using BIA are the extensive preparations. A patient is required to fast for at least 4-6 hours beforehand, not to participate in any athletic activity on the day of the test, and the area on the body for the electrodes needs to be shaved and cleaned (Mialich, Sicchieri & Junior, 2014). These steps and the complexity of equation selection increase the difficulty of using BIA.

2.1.3 *Body Mass Index*

Body mass index is a useful way to measure obesity and weight gain (WHO, 2000). BMI is defined as follows:

$$\boldsymbol{BMI} = \frac{\boldsymbol{mass\ (kg)}}{\boldsymbol{height^2\ (m^2)}} \tag{2.1}$$

A range table is used to classify the patient based on the calculated value. The reliance on a height and weight ratio means people of differing heights and weights can have similar BMIs. Figure 2.3 shows the relationship between height, weight, and BMI. The coloured sections correlate to the classification categories and the dashed lines indicate further subdivision within those categories. Classifications range from underweight to obese class III.

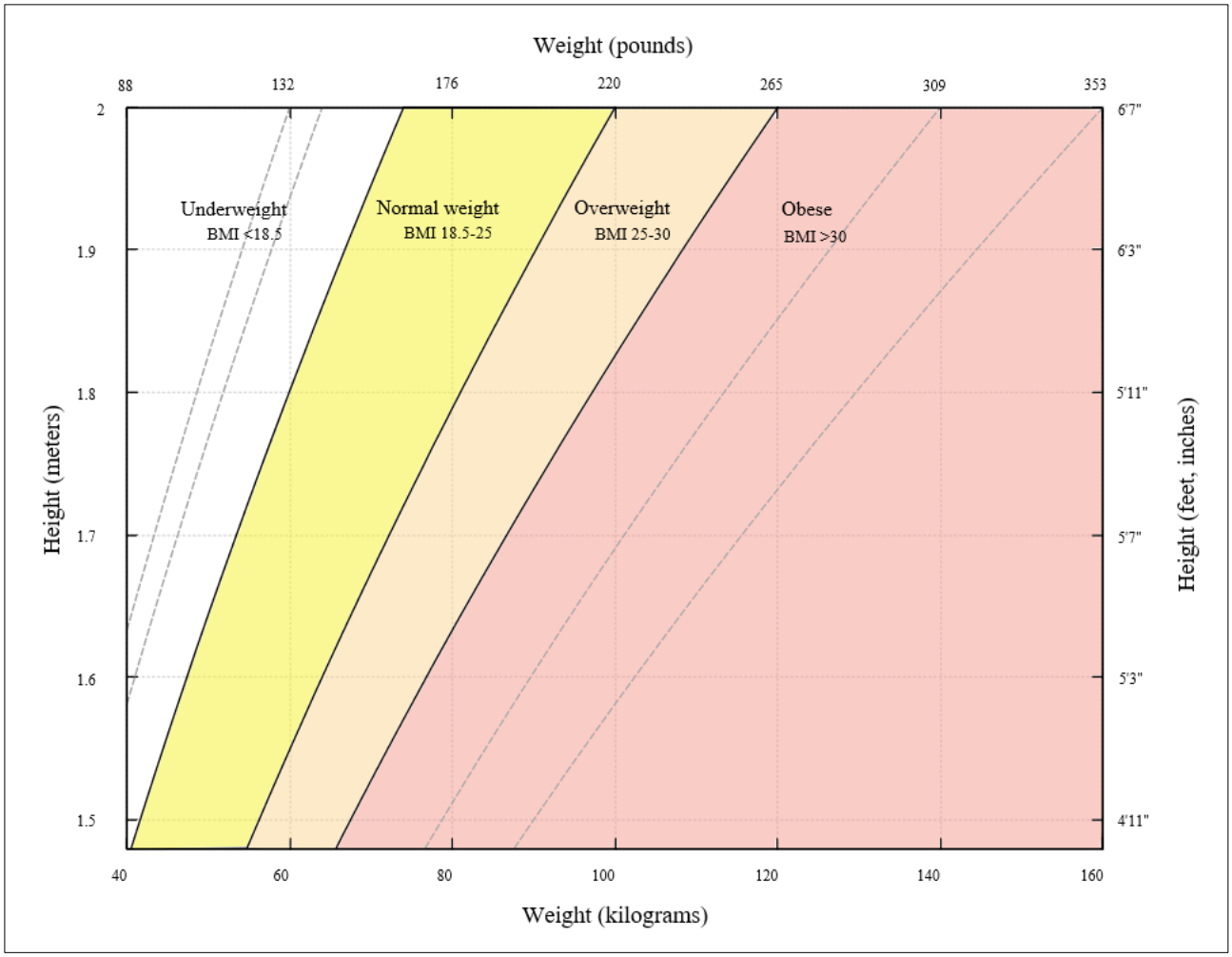

Figure 2.3: Weight versus height chart showing the BMI cut-offs. The dashed lines show the subdivisions within a major category. (Image: (Amfucla, 2017))

The appropriateness of these cut-offs for different populations has been studied. It has been shown that the cut-offs differ from real-world values for Surinamese South Asian children (de Wilde, van Dommelen & Middelkoop, 2013), Brazilian women (Wollner et al., 2017), and Cambodian adults (An et al., 2013). It has been recommended by a World Health Organization (WHO) expert consultation that each country identify BMI levels where public health action is most appropriate whilst retaining the use of existing categories to facilitate international comparisons (WHO Expert Consultation, 2004).

In addition to population variability, there are other limitations with BMI. Body mass index is associated with both fat and lean mass and cannot differentiate between them (Wells, Ruto & Treleaven, 2008).

Abramowitz et al. (2018) examined the association between muscle mass and the BMI-mortality relationship. They found that after adjusting for muscle mass, higher BMI related to increased fat. The influence of muscle mass on BMI has been described elsewhere with examples of obese muscular persons (Prentice & Jebb, 2001) and different body types having similar BMIs (WHO Expert Consultation, 2004). With the health risks of obesity generally due to abdominal fat (Wells, Ruto & Treleaven, 2008), using additional metrics, such as waist circumference (WC), can improve the reliability of BMI (Janssen, Katzmarzyk & Ross, 2004, WHO Expert Consultation, 2004).

Waist circumference has been shown to be an appropriate method of identifying people at risk from being overweight and having a high central fat distribution (Lean, Han & Morrison, 1995). Lean, Han & Morrison (1995) further argue that using multiple body measures can provide a better method of assessing the health of an individual and that these measurements can be performed manually by patients. However, underreporting occurs for self-reported measures of WC (Bigaard et al., 2005, Spencer, Roddam & Key, 2004) and weight (Spencer et al., 2002). Overreporting occurs for height (Spencer et al., 2002). Errors in self-reported data will propagate into any calculations such as BMI. An existing tool that limits errors associated with self-reporting is the 3D scanner.

2.2 3D Scanner Body Measurement

Three-dimensional scanners are tools for body measurement that contribute towards obesity research and clinical use (Wells, Ruto & Treleaven, 2008). Three-dimensional scanning is preferred to techniques such as DXA, magnetic resonance imaging (MRI), or computed tomography (CT) due to factors such as a low scan time and a relatively lower cost (Heymsfield et al., 2018, Wells, Ruto & Treleaven, 2008). Disadvantages include the absolute cost and additional hardware requirements (Tzou et al., 2014). Three-dimensional scanning for body measurement consists of the steps of data acquisition, data processing, and anatomical measurement (Heymsfield et al., 2018).

2.2.1 3D Scanning Steps

i. Data Acquisition

Whole body scanners typically consist of four components. These are light source(s) projected on the body, cameras to capture the light reflected from the body, software to construct the model from the images, and a computer to view the model (Daanen & van de Water, 1998). The light source(s) and cameras are involved in data acquisition. Four types of light sources have been identified in the literature. These are structured light systems, multi-view camera systems, laser based systems, and millimetre wave systems (Daanen & ter Haar, 2013). Table 2.1 below shows a description for each of the technologies mentioned.

Table 2.1: 3D scanner technology types and their descriptions. Adapted from Bragança, Arezes & Carvalho (2015).

Technology	Description
Structured Light	A structured pattern is projected onto the body. The deformation of the pattern is detected and used to construct a 3D model.
Multi-view Camera	Images are recorded from two or more cameras, simultaneously. The images are used to determine the depth to the body and produce a 3D model.
Laser	A laser line is projected onto the body from different angles and viewed by cameras at fixed angles. A sensor detects the deformation of the two-dimensional (2D) line on the 3D object which are used to create the 3D model.
Millimetre Wave	Active scanners use the reflection of millimetre waves projected onto the body. Passive scanners use millimetre waves emitted by the body and reflected from the surroundings by the body (Yujiri, Shoucri & Moffa, 2003).

The advantages of laser over structured light include better accuracy in capturing the proportions of the body (Daanen & ter Haar, 2013) and that only one deformation line needs to be analysed resulting in simpler software decoding (Daanen & van de Water, 1998). Structured light systems have the advantage of having no moving parts and as a result, longer device lifespans (Daanen & van de Water, 1998). However, they are sensitive to light interference (Daanen & ter Haar, 2013). The decision to use either is thus dependent on accuracy requirements, scanning environment, and cost factors. Multi-view systems are not sensitive to light interference but they are not as accurate as laser or structured light systems (Daanen & ter Haar, 2013). Millimetre wave systems are advantageous as they can scan through clothing but are less accurate than the other systems (Daanen & ter Haar, 2013) and genitals can be seen which presents a privacy concern (Bragança, Arezes & Carvalho, 2015). The lower accuracy and privacy concerns make these systems less suitable for body scanning. Figure 2.4 shows an example of a full body 3D scanning system. The subject stands in the centre of the device in a scanning position. The white stickers are on key anatomical sites and act as reference points when taking measurements from the scan data.

Figure 2.4: 3D scan data acquisition process with a subject in a scan pose and covered in white stickers at key anatomical sites. (Image credit: (Gulliford, 2006), Image licensed for reuse with modification).

ii. Data Processing

Software is often involved in image acquisition, with repair of the scanned images as well as database management being the main software-related tasks (Daanen & ter Haar, 2013). Additional tasks include point cloud processing and meshing (Daanen & van de Water, 1998). Most vendors often bundle proprietary software with their hardware (Tzou et al., 2014).

iii. Anatomical Measurements

Once a 3D model has been created, anatomical measurements can be taken. Measurements are performed by first identifying landmarks to define body regions and applying mathematical operations to determine the measurements (Heymsfield et al., 2018) The metrics of interest identified are body volume (BV), height, and WC. The accuracy of the measurements is largely dependent on the performance of the scanners as any errors will propagate through the calculations. The performance of scanners varies, and it is necessary to evaluate their performance against established standards.

iv. Allowable Error

Gordon et al. (2014) describe allowable errors for a range of anthropometric measurements. Table 2.2 shows the allowable errors for height and WC measurements.

Table 2.2: Allowable errors for height (stature) and WC measurement (Gordon et al., 2014).

Measurement	Allowable error – (mm)
Stature (Height)	6
Waist circumference	12

When assessing the accuracy in a dataset, the mean difference (MD) and mean absolute difference (MAD) can be calculated (Gordon et al., 1989). The MD describes the average difference between the 3D scan measurements and the ground truth. The MAD describes the absolute average difference and informs the distribution of errors in terms of over- or underestimation. They are quantified as follows:

$$\boldsymbol{MD(mm)} = \frac{\mathbf{1}}{\boldsymbol{n}}\sum \boldsymbol{m_{syn}^{i} - m_{man}^{i}} \tag{2.2}$$

$$\boldsymbol{MAD(mm)} = \frac{\mathbf{1}}{\boldsymbol{n}}\sum \left|\boldsymbol{m_{syn}^{i} - m_{man}^{i}}\right| \tag{2.3}$$

Where m_{man}^{i} is the i^{th} manual measurement and m_{syn}^{i} the i^{th} measurement from the model. Mean absolute differences should be within the allowable deviations.

2.2.2 Scanner Performance

Adler et al. (2017) compared the performance of a VitusSmart XXL 3D scanner against the performance of air displacement plethysmography BOD POD *(COSMED, Rome, Lazio, Italy)* in determining BV. They found that the 3D scanner BV was higher by 1.1 ± 0.9 *l* for standard scans. Nonetheless, the 3D scanner-based BV correlated strongly with the air displacement plethysmography -based BV. The performance of 3D scanners has been further validated with scanners showing good performance when evaluating body measurements (Jaeschke, Steinbrecher & Pischon, 2015, Koepke et al., 2017, Medina-Inojosa et al., 2017, Simenko & Cuk, 2016).

2.2.3 Low-Cost Scanners

A drawback associated with 3D scanners is cost. Efforts to address this include the introduction of cheaper scanners and repurposing of existing devices.

i. Microsoft Kinect

Originally designed as an input device for the Xbox 360 game console (Microsoft, 2009), the Microsoft Kinetic has been adapted for other uses including computer vision applications (Han, Jungong et al., 2013, Tong et al., 2012). It consists of an infrared (IR) projector, an IR camera, and a colour camera (Han, Jungong et al., 2013). The IR projector and IR camera act as a structured light scanner. Tong et al. (2012) presented a system for scanning whole bodies. It uses three Microsoft Kinect devices that scan the upper, middle, and lower parts of the body, respectively. The accuracy of the reconstruction varied with the error ranging from 15 mm to 62 mm depending on the part of the body scanned. The low resolution, a complex registration procedure, and complex reconstruction algorithms limited the accuracy of the system. Clarkson et al. (2016) used four Kinects arranged in a vertical orientation and tested it against International Organization for Standardization (ISO) and International Society for the Advancement of Kinanthropometry (ISAK) standards for measuring the girth of body segments. Using manufactured cylinders to represent different segments, they found that the measurements complied with ISO standards for larger segments but were non-compliant for smaller segments. Furthermore, they found the system compliant to ISAK standards for practitioners.

ii. Occipital Structure Sensor

The Occipital Structure Sensor *(Occipital, Boulder, CO, United States)* is an iPad *(Apple, Cupertino, CA, United States)* attachment that incorporates IR sensors, IR light emitting diodes (LEDs), and an additional camera to enable 3D scanning on an iPad (Knoops et al., 2017). Figure 2.5 shows the Structure Sensor. The blue box contains the sensing apparatus whilst the black bar is the attachment mechanism. Figure 2.6 shows the Structure Sensor attached to an iPad. The sensing apparatus housing lies adjacent to the iPad camera when attached. The iPad retains its mobility when the Structure Sensor is attached.

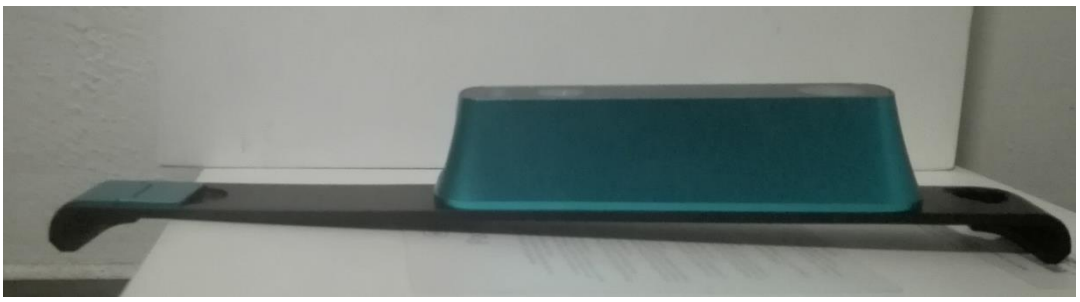

Figure 2.5: Occipital Structure Sensor

Figure 2.6: iPad with the Structure Sensor attached.

Dessery & Pallari (2018) analysed the performance of the Structure Sensor versus the relatively more expensive handheld Artec Eva *(Artec, Luxembourg City, Luxembourg, Luxembourg)* when scanning the knee. The results of each scan were also compared against conventional measurement techniques. The authors found that the Structure Sensor overestimated circumferences by 13 mm compared to the Artec Eva which overestimated by 2.5 mm. The use of low-cost scanners is dependent on the accuracy requirements of the application.

2.2.4 Photograph-Based Reconstruction

There exists another class of low-cost scanning implementation that performs photograph-based reconstruction. These implementations exist as applications and web services that use images taken by cameras or smartphones to reconstruct 3D models. There is a mixture of freely available and commercial applications and web services that perform photograph-based 3D reconstruction. Examples include Arc3D *(VISICS, Leuven, Flanders, Belgium)* and Autodesk 123D *(Autodesk, San Rafael, California,*

United States) (Bemis et al., 2014). The applications take images as input with processing and reconstruction performed externally and the results transferred to the user. Photograph-based reconstruction using methods such as structure from motion (Häming & Peters, 2010) and statistical shape models (SSMs) (Ballester et al., 2016, Schönborn et al., 2017) has been previously demonstrated.

2.3 Shape Models

Statistical shape models are a method of statistically representing shape using an average shape and the common variations associated with that shape (Heimann & Meinzer, 2009). Shape is defined to be any geometric information after accounting for scale, translation, and rotation (Dryden & Mardia, 2016). The most common method for representing shape is as a set of points distributed across a surface as a point distribution model (PDM) (Heimann & Meinzer, 2009). Shape is described by the following equation:

$$\boldsymbol{V} = (\boldsymbol{x_1}, \boldsymbol{y_1}, \boldsymbol{z_1}, \dots, \boldsymbol{x_i}, \boldsymbol{y_i}, \boldsymbol{z_i})^{\boldsymbol{T}} \tag{2.4}$$

A vector V contains *i* 3D points. The points are connected to one another to create a mesh. According to Cootes et al. (1995), PDMs can be used to describe the shape of an object and the variability of the object. They state that this is achieved using landmark points and training data. The training data must be registered and in correspondence.

2.3.1 Registration and Establishing Correspondence

Registering and establishing correspondence between 3D meshes in building shape models has been demonstrated (Anguelov et al., 2005b, Ballester et al., 2016, Pishchulin et al., 2017). Anguelov et al. (2005b) deploy a three-stage pipeline for nonrigid registration in the development of their shape completion and animation of people (SCAPE) model. They begin with a manually landmarked reference mesh, use the correlated correspondence algorithm (Anguelov et al., 2005a) to establish correspondence, and use a modified iterative closest point (ICP) algorithm (Haehnel, Thrun & Burgard, 2003) to perform nonrigid registration. Their method requires appropriate subsampling of meshes to ensure they have the same number of points and triangles. An extension to SCAPE called S-SCAPE (Jain et al., 2010) has been used by Pishchulin et al. (2017) in a registration and correspondence process.

The process employed by Pishchulin et al. (2017) requires a registered dataset to perform rigid alignment and human intervention to reject unsuitable results. Rigid alignment can be performed through a standard rigid alignment algorithm. Popular algorithms include the standard ICP (Heimann & Meinzer, 2009) described by Besl & McKay (1992). Following alignment, they use the method described by for nonrigid template fitting alignment to establish correspondence.

Ballester et al. (2016) employ a method that is not dependent on an S-SCAPE dataset. They use a reconstruction and parameterisation algorithm a modified ICP algorithm (Amberg, Romdhani & Vetter, 2007), and a deformation transfer algorithm (Sumner & Popović, 2004). However, it is not clear how the algorithms are combined. The result of the process is a homologous dataset that is then aligned using rotations and translations through Generalized Procrustes analysis (GPA) (Gower, 1975). Unlike Anguelov et al. (2005b), their process requires the manual placement of 35 landmarks per mesh where as Anguelov et al. (2005b) only requires 4-12 per mesh to initialise the correlated correspondence algorithm. However, it can operate on unaligned, non-parameterised meshes. The methods deployed by Anguelov et al. (2005a), Ballester et al. (2016), Pishchulin et al. (2017) further go on to use principal component analysis (PCA) to define the shape model.

2.3.2 Principal Component Analysis

When using PCA, a mean shape, $\bar{x}$, is determined using the following equation (Heimann & Meinzer, 2009):

$$\bar{\boldsymbol{x}} = \frac{\mathbf{1}}{\boldsymbol{N}} \sum_{\boldsymbol{i}=\mathbf{1}}^{\boldsymbol{N}} \boldsymbol{x_i} \tag{2.5}$$

Where $\bar{x}$ is the mean shape, N is the total number of shapes used to determine the mean, and x_i is the ith shape in the training data. For each shape, the deviation from the mean is calculated. These deviations are then used to calculate a covariance matrix, S given by:

$$\boldsymbol{S} = \frac{\mathbf{1}}{\boldsymbol{N}} \sum_{\boldsymbol{i}=\mathbf{1}}^{\boldsymbol{N}} \boldsymbol{dx_i dx_i}^{\boldsymbol{T}} \tag{2.6}$$

Where dx_i is the difference between the ith shape and the mean. An eigen decomposition results in eigenvectors that correspond to the modes of variation and eigenvalues that correspond to the variances. This allows for the definition of any shape by the following equation:

$$\boldsymbol{x} = \bar{\boldsymbol{x}} + \sum_{\boldsymbol{i}=\mathbf{1}}^{\boldsymbol{c}} \boldsymbol{b_i \phi_i} \tag{2.7}$$

The value ϕ is the matrix of eigenvectors and b is a vector of weights. The vector contains values within a weighted range of the variances. The strength of an SSM is proportional to the quantity of training data; however, the amount of data is always too low and problems related to manual segmentation, poor sample size estimates, and over-constrained models exist (Heimann & Meinzer, 2009). Lüthi et al. (2018) attempt to overcome the training data issue through a generalised PDM called a GPMM.

2.3.3 Gaussian Process Morphable Model

Gaussian Process Morphable Models make use of Gaussian processes (GP) in modelling the shape variations (Lüthi et al., 2018). In that paradigm a shape, s, is defined by a deformation, u, from a reference shape Γ_R with x being an element of the reference shape. The formulation is as follows:

$$\boldsymbol{s} = \{\boldsymbol{x} + \boldsymbol{u}(\boldsymbol{x}) | \boldsymbol{x} \in \boldsymbol{\Gamma_R}\} \tag{2.8}$$

$$\boldsymbol{\Gamma_R} \subset \mathbb{R}^{\mathbf{3}}$$
$$\boldsymbol{u}: \boldsymbol{\Omega} \rightarrow \mathbb{R}^{\mathbf{3}}$$

The reference shape is a subset of 3D space and the deformation follows on from that. Additionally, the reference shape can be defined continuously. The deformations, modelled as a GP, are defined as follows:

$$\boldsymbol{u} \sim \boldsymbol{GP}(\boldsymbol{\mu}, \boldsymbol{k}) \tag{2.9}$$

$$\boldsymbol{\mu}: \boldsymbol{\Omega} \rightarrow \mathbb{R}^{\mathbf{3}}$$
$$\boldsymbol{k}: \boldsymbol{\Omega} \times \boldsymbol{\Omega} \rightarrow \mathbb{R}^{\mathbf{3}}$$

Where μ is the deformation field and k is the covariance function. Computational complexity is managed by discretisation of the mean function into a form similar to the PDM mean. The Karhunen-Loève (Karhunen, 1946, Loève, 1955) expansion of the GP results in the following equation:

$$\tilde{\boldsymbol{u}} \sim \boldsymbol{\mu}(\boldsymbol{x}) + \sum_{\boldsymbol{i}=\mathbf{1}}^{\infty} \boldsymbol{\alpha_i} \sqrt{\boldsymbol{\lambda_i}} \boldsymbol{\phi_i}(\boldsymbol{x}), \boldsymbol{\alpha_i} \in \mathbb{N}(\mathbf{0}, \mathbf{1}), \tag{2.10}$$

In the expansion, the GP is represented as a linear combination of orthogonal functions. The terms λ_i and ϕ_i represent the eigenvalues and eigenfunctions. Variance is represented by the sum of the eigenvalues. A low-rank variant that sums *r* orthogonal functions can be used. The authors make use of the Nyström method (Nyström, 1930) to approximate the eigenvalue/eigenfunction integral with a weighted sum. Before use of GPMM, there is a need to define the GP mean and a suitable kernel function (Lüthi et al., 2018).

i. *GPMM Mean*

The mean can be determined using a PDM form (Lüthi et al., 2018). Deformation fields are determined from a reference shape and used to calculate the GP mean as follows:

$$\boldsymbol{\mu_{PDM}(x) = \frac{1}{n}\sum_{i=1}^{n} u_i(x)} \tag{2.11}$$

Where μ is the mean and u_i is a deformation field calculated from a reference shape Γ_R.

ii. *GPMM Kernel*

A kernel function can be approximated using the mean (Lüthi et al., 2018). It is defined as follows:

$$\boldsymbol{k_{PDM}(x,y) = \frac{1}{n-1}\sum_{i=1}^{n}\big(u_i(x) - \mu_{PDM}(x)\big)\big(u_i(y) - \mu_{PDM}(y)\big)^T} \tag{2.12}$$

Where k is the kernel, u_i is the deformation field for x and y, and μ_{PDM} is the mean. Additionally, kernels can be combined to create news kernels for bias reduction and variation localisation (Lüthi et al., 2018). In building the shape model, the measures of accuracy must be considered.

2.3.4 *Accuracy Measures*

The quality of a model is dependent on its ability to represent shapes of the same class (Davies, 2002). The establishment of deep correspondence across the object class to ensure sufficient parameterisation of the shape affect the quality (Styner et al., 2003). Styner et al. (2003) describe three measures for correspondence quality in SSMs. They are:

- Generalisation – The ability to describe shape instances not in the training data.
- Specificity – The ability to represent only valid instances of an object.
- Compactness – The ability to use a minimal set of parameters to describe an instance.

These measures describe how well the model can represent shapes in the class whilst using as few parameters as possible.

2.3.5 *Dataset*

A dataset is necessary in constructing the GPMM. There are existing datasets of full body 3D scans (Bogo et al., 2014a, Durá-GIl et al., 2018, Robinette et al., 2002a). These datasets have been used for shape modelling (Ballester et al., 2016, Bogo et al., 2014b, Pishchulin et al., 2017). The datasets contain 3D scans and a series of manual measurements. However, a database containing 3D scans, manual measurements, and 2D images has not been identified. Once the GPMM has been built using an appropriate dataset, reconstruction can take place.

2.3.6 *3D Reconstruction From 2D Images*

The goal of 3D from 2D reconstruction is to estimate an appropriate 3D model from 2D images. Reconstruction involves the steps of image collection, camera parameter computation, 3D geometry reconstruction, and optionally, texture reconstruction (Furukawa & Hernández, 2015). The use of the

final step is dependent on the intended application. Successful examples of 3D from 2D reconstruction are described below.

Schönborn et al. (2017) describe reconstruction as a process of finding a synthetically generated image that best matches an input image. This is formulated as an optimisation problem characterised by the following equation:

$$\boldsymbol{\theta}^* = \left(\mathbf{arg}\,\boldsymbol{min}_{\boldsymbol{\theta}}\boldsymbol{C}\left(\boldsymbol{I}(\boldsymbol{\theta}),\tilde{\boldsymbol{I}}\right) + \boldsymbol{\mathcal{R}}(\boldsymbol{\theta})\right) \tag{2.13}$$

Where θ^* is the parameters that best explain the image, C is the cost function evaluating the distance between the generated image I and the target $\tilde{I}$ with a regularisation term $\mathcal{R}$. Methods to solve the problem include stochastic gradient descent (Blanz & Vetter, 1999), a feed-forward setup (Aldrian & Smith, 2013), and a machine learning based descent method (Xiong & De la Torre, 2013). Each of the methods rely on good initialisation, good update steps, and are only suitable for some probabilistic inferencing tasks (Schönborn et al., 2017). Schönborn et al. present a probabilistic propose-and-verify fitting approach for face fitting based on a Markov Chain Monte Carlo (MCMC) method. The propose-and-verify architecture evaluates proposed surfaces and accepts or rejects using a stochastic method which makes it suitable for incorporating uncertain information and provides robustness against local optimisations. They make use of the Metropolis-Hastings algorithm (Hastings, 1970, Metropolis et al., 1953) in building the Markov Chain through an acceptance/rejection framework. Gerig et al. (2018) apply the method in a pipeline for face registration based on a GPMM that incorporates face image analysis. The registration process relies on the construction of a posterior model for the already identified landmarks. An iterative process to find the best fit surface is then performed. Identified landmarks can also be used when performing GP regression as described by Rasmussen (2003) and demonstrated by Lüthi et al. (2018).

The goal of regression is to compute a suitable posterior model. Regression requires a reference and a target. The GP acts as a prior for Bayesian inference and is used to calculate a probability distribution over the data (Rasmussen, 2003). The evidence is derived from the image landmarks $L_T = \{l_T^1, \dots, l_T^n\}$ which are compared to the shape model landmarks $L_R = \{l_R^1, \dots, l_R^n\}$. The deformation $\hat{u}^i$ can be calculated for each landmark as follows:

$$\boldsymbol{L} = \left\{\left(\boldsymbol{l_R^1}, \boldsymbol{l_T^1} - \boldsymbol{l_R^1}\right), \dots, \left(\boldsymbol{l_R^n}, \boldsymbol{l_T^n} - \boldsymbol{l_R^n}\right)\right\} = \left\{\left(\boldsymbol{l_R^1}, \boldsymbol{\hat{u}^1}\right), \dots, \left(\boldsymbol{l_R^n}, \boldsymbol{\hat{u}^n}\right)\right\} \tag{2.14}$$

Additionally, each deformation $\hat{u}^i$ is subject to Gaussian noise $\epsilon \sim \mathcal{N}(0, \sigma \mathrm{I}_{3x3})$. The joint distribution $u|l_R^1, \dots, l_R^n, \hat{u}_R^1, \dots, \hat{u}_R^n$ is a Gaussian process $GP(\mu_p, k_p)$. Thus, by providing 3D landmarks, deformations from the reference GP can be calculated and a posterior GP can be determined. Additionally, GP regression does not require an iterative process like MCMC. For reconstruction, the mean of the posterior is taken as the most likely solution to the reconstruction problem as done by Lüthi, Jud & Vetter (2011).

Examples of full body reconstruction are described below.

2.3.7 Body Volume Reconstruction

The 3D specialist company Select Research[1] (Select Research, 2018) developed an application called Body Volume Indicator (BVI) (Body Volume, 2018). The application uses two images of a person to produce a 3D model of the body. The model is used to determine BV and additional health indicators such as WC. The application is available commercially through an iPad application or an application

[1] https://www.selectresearch.com/

programming interface (API) to be integrated into custom applications. The method used in reconstruction is not publicly available nor are there validation studies.

Ballester et al. (2016) describe a method for 3D reconstruction using two images taken with a smartphone. The method uses a PCA-based shape model built from the scans of 761 participants that is represented by 60 principal components. The smartphone application uses information provided by the user (age, gender, weight, and height) to create an outline to estimate a body outline. Furthermore, camera sensor information (orientation and camera specifications) is used to perform calibration. Fitting is performed through an optimisation process that searches the PCA space and finds a body shape that best matches the image outlines. The method produced a surface-to-surface distance per vertex of 2.1 mm as an error. Boisvert et al. (2013) also apply a PCA space search to reconstruct bodies using silhouettes. The surface-to-surface distance per vertex was 8 mm. The limitation of these systems is the requirement for the person to be in a specific pose. Song et al. (2018) described a similar system that made use of two photos. Their method is targeted towards the fashion industry and allows users to be dressed in casual clothes. Furthermore, they used learned regressions to perform body reconstruction on the smartphone. The mean error for chest/waist/hip is 2.89/1.93/2.22cm. These applications demonstrate the feasibility of a smartphone application. A potential concern with mobile implementations is processing time. Reconstruction time has been found to range from 10-15 minutes for general reconstruction (Tzou et al., 2014) and up to 20 minutes for face reconstruction (Gerig et al., 2018). An exception is body reconstruction performed in 30 seconds (Body Volume, 2018). In each instance the images are uploaded to a server to perform reconstruction.

2.4 Chapter Summary

Conventional methods of measuring body composition such as DXA and BIA are inaccessible and complex to use. The preferred alternative of BMI does not suffer from the same drawbacks. However, there are limitations to using BMI. Alternate measures such as BV in conjunction with other metrics may be more useful in assessing body composition. Three-dimensional scanners can provide these alternate measures, but they are inaccessible due to cost. Smartphones may provide an alternative to traditional 3D scanners. The costs for certain smartphones are lower than for some 3D scanners. Additionally, the low-cost scanners still require the purchase of additional hardware. Three-dimensional from 2D reconstruction can exploit existing levels of smartphone ownership and has been demonstrated previously with a healthcare focused application available for commercial use. However, the methodology and validation are not publicly available. The other examples of reconstruction have not translated into an available application for health-related use. An open source, validated methodology of sufficient accuracy for BV evaluation has not been encountered in the literature. Additionally, a dataset containing 3D scans, manual measures, and 2D images necessary for development and validation has not been identified.

3. Methodology Overview

3.1 Methodology

Figure 3.1 below shows the methodology overview. The objectives are in blue, the steps are in grey, and the objective outputs are in yellow.

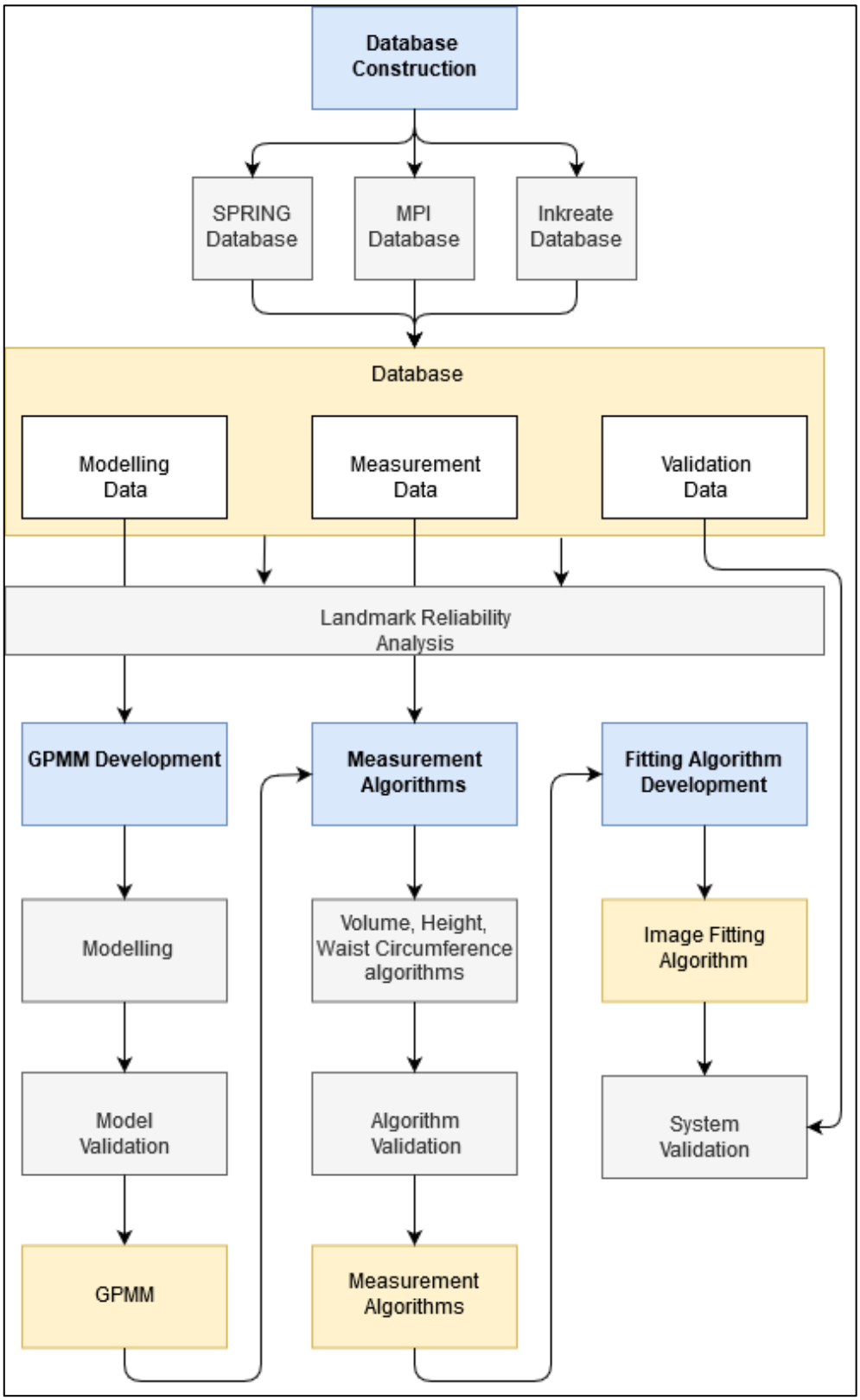

Figure 3.1: Developed methodology consisting of of database construction, GPMM development, fitting algorithm development, and system validation.

The developed methodology consisted of the steps of database construction, Gaussian process morphable model (GPMM) development, measurement algorithm development, and fitting algorithm development. The database contains data from three 3D scan repositories. The output was a database with data for modelling, measurement data, and images for validation. Landmark reliability was then assessed. The GPMM development used the modelling data and involved modelling and validation. The output was a GPMM describing the human body. Algorithms to measure height, volume, and waist circumference were then developed and tested. This was followed by fitting algorithm development and system validation.

3.2 Database

An important part of shape modelling is the quality and quantity of the modelling and test data (Heimann & Meinzer, 2009). The database draws from existing repositories. The first is the Semantic Parametric Reshaping of Human Body Models (SPRING) dataset (Yang et al., 2014). The dataset contains 3048 registered meshes with point-to-point correspondences established. Each mesh was converted to the STL format using Blender (*Blender Foundation, Amsterdam, North Holland, Netherlands*). The second repository is the MPI-FAUST dataset (Bogo et al., 2014a). The dataset contains 300 registered meshes with point-to-point correspondences established. The dataset is made of ten individuals in 30 different poses. From this, 10 scans in the 3D scan position described in ISO 20685:2010 (International Organization for Standardization, 2010) were selected. Screenshots from the anteroposterior (AP) view and lateral (LAT) views were taken to produce 20 2D images. The AP and LAT view images are considered to be biplanar images. The third repository is the Inkreate dataset (Durá-GIl et al., 2018). It contains 56 body meshes without established correspondence in the STL format, a document containing gender and measurements for each mesh, and a document explaining the measurements. Figure 3.2 shows example meshes from the Inkreate and SPRING datasets. The Inkreate mesh is light yellow. An example of a female and male mesh from the SPRING dataset are also shown. Figure 3.3 shows an example of a mesh from the MPI dataset. Biplanar images are shown to match the format used in the reconstruction process.

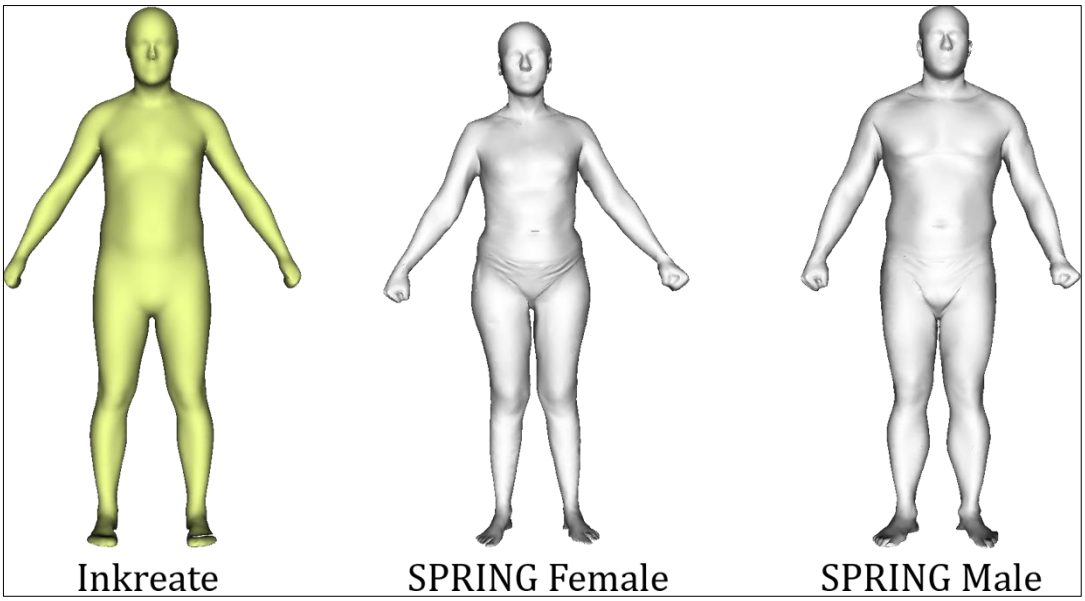

Figure 3.2: Example meshes from the Inkreate and SPRING datasets.

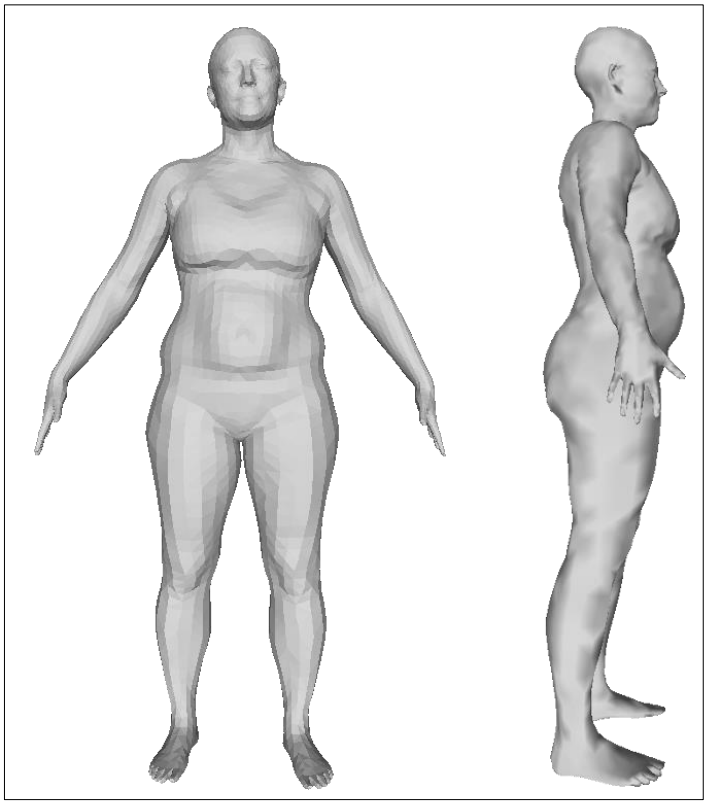

Figure 3.3: Biplanar images of mesh in MPI dataset.

3.3 Development Environment

The system was developed using the Scala programming language. Scala is statically typed and supports object-oriented and functional programming design (Odersky et al., 2004). The Scalismo[2] (Graphics and Vision Research Group University of Basel, 2018) library was used. Scalismo is a Scala library and includes GPMMs and functions for model building, surface registration and active shape model fitting (Lüthi et al., 2018). The IntelliJ IDEA (*JetBrains, Prague, Prague, Czech Republic*) integrated development environment (IDE) was used for programming.

[2] https://github.com/unibas-gravis/scalismo

4. GPMM Development

The basis of the project is the Gaussian process morphable model (GPMM). The model is used to capture the statistics of the human body shape and is used as the basis for reconstruction. This presents an overview of the modelling process as well as tests to assess the model quality.

4.1 Dataset

The development of the GPMM used the SPRING dataset. The dataset's split into male and female meshes was maintained in the development.

4.2 Modelling

The GPMMs were modelled using the PDM approximation described in section 2.3.3. The mean is characterised by equation $\boldsymbol{\mu_{PDM}(x) = \frac{1}{n}\sum_{i=1}^{n} u_i(x)}$ (2.11) and the kernel by equation $\boldsymbol{k_{PDM}(x,y) = \frac{1}{n-1}\sum_{i=1}^{n}\left(u_i(x) - \mu_{PDM}(x)\right)\left(u_i(y) - \mu_{PDM}(y)\right)^T}$ (2.12) . Separate GPMMs were developed for the female and male datasets. As a part of the process, each set of meshes was aligned to a reference mesh (randomly selected for each gender) using Generalized Procrustes analysis (GPA). The reference meshes were then landmarked. Table 5.1 in section 5.1 shows a list of the landmarks with descriptions. Following the calculation of the mean and kernel, a low-rank GP approximation was created using the Nyström approximation and a random mesh sampler. The low-rank GP was then used to create the final GPMM. Following the example by Pishchulin et al. (2017), the first three modes of variation were qualitatively inspected to examine the modes of variation. Each mode was inspected at three standard deviations away from the mean. Figure 4.1 and Figure 4.2 below show the first three modes for both the female and male GPMMs. The mean is in light grey, the first mode in red, the second mode in blue, and the third mode in green.

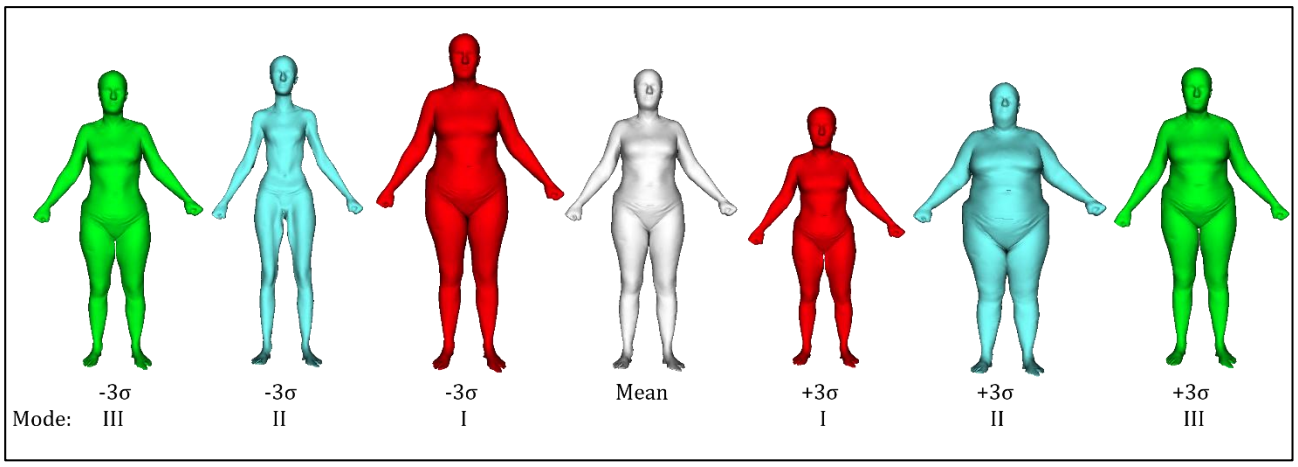

Figure 4.1: First three modes of variation at three standard deviations for the female GPMM.

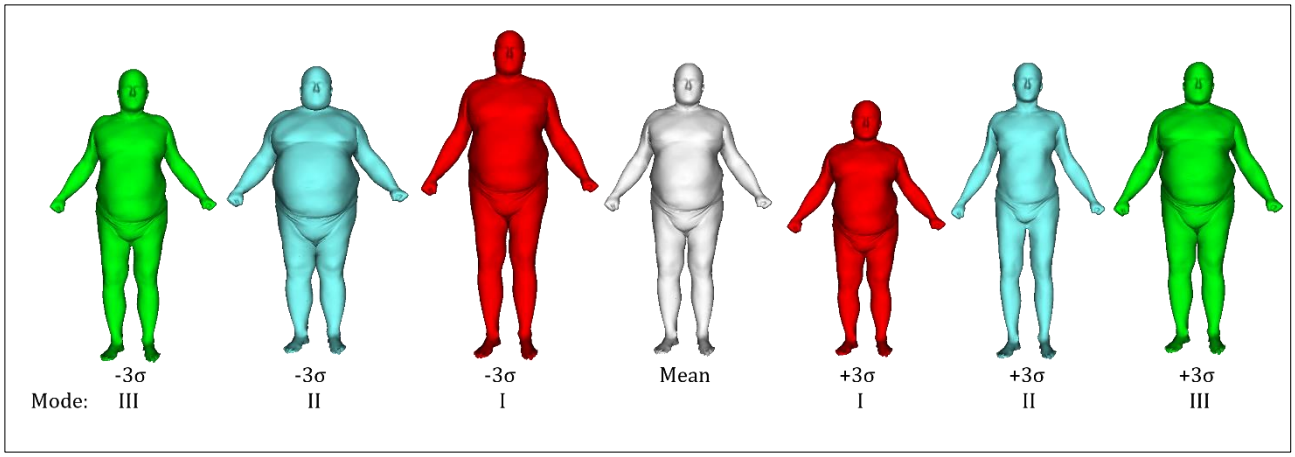

Figure 4.2: First three modes of variation at three standard deviations for the male GPMM.

The shapes produced appear consistent with the shape of the human body. In addition to the visual inspection, generalisation, specificity, and compactness were assessed to evaluate the model quality.

4.3 Testing model quality

Generalisation and specificity were tested on a random sample of the total training data. For both female and male, 100 shapes were randomly selected. This was done to significantly reduce the runtime. Generalisation and specificity values were compared to those seen in literature for similar shape models. Compactness was assessed using the eigenvalues of each model.

4.3.1 Generalisation

Generalisation testing began with an instance being withdrawn from the dataset. The remaining data was then used to build a GPMM. The surface-to-surface distance per vertex between the withdrawn instance and its projection onto the GPMM was then evaluated. The same process was repeated for each of the remaining instances from the dataset. Figure 4.3 below shows an illustration of surface-to-surface distance per vertex.

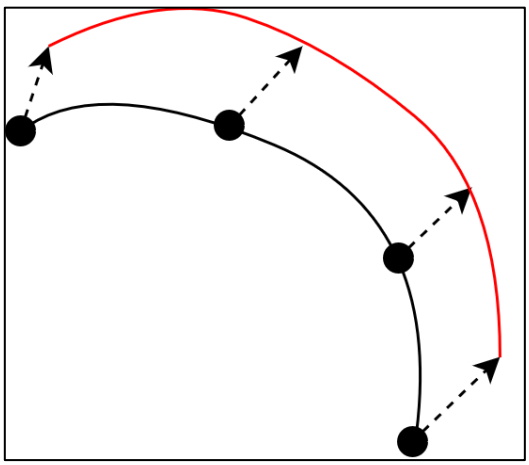

Figure 4.3: Surface-to-surface distance per vertex illustration.

As described in section 2.3, the shape is represented by points or vertices connected to one another to form a mesh with the connections becoming the surface. The black line represents the withdrawn instance, the black dots represent the vertices on the surface, and the red line the projected instance. For each vertex, the shortest distance from it to the red surface is calculated. These values are then averaged to calculate the surface-to-surface distance per vertex. The distance is used to measure the error between the original mesh and the projected instance. Figure 4.4 and Figure 4.5 below show the

generalisation results for the female and male models. Each figure shows the error versus the number of training shapes. For both models, the average error decreases as the number of training shapes increases. The decrease in distance lessens as the curve begins to plateau. The female model plateaued at 27.1 mm and the male model plateaued at 24.9 mm.

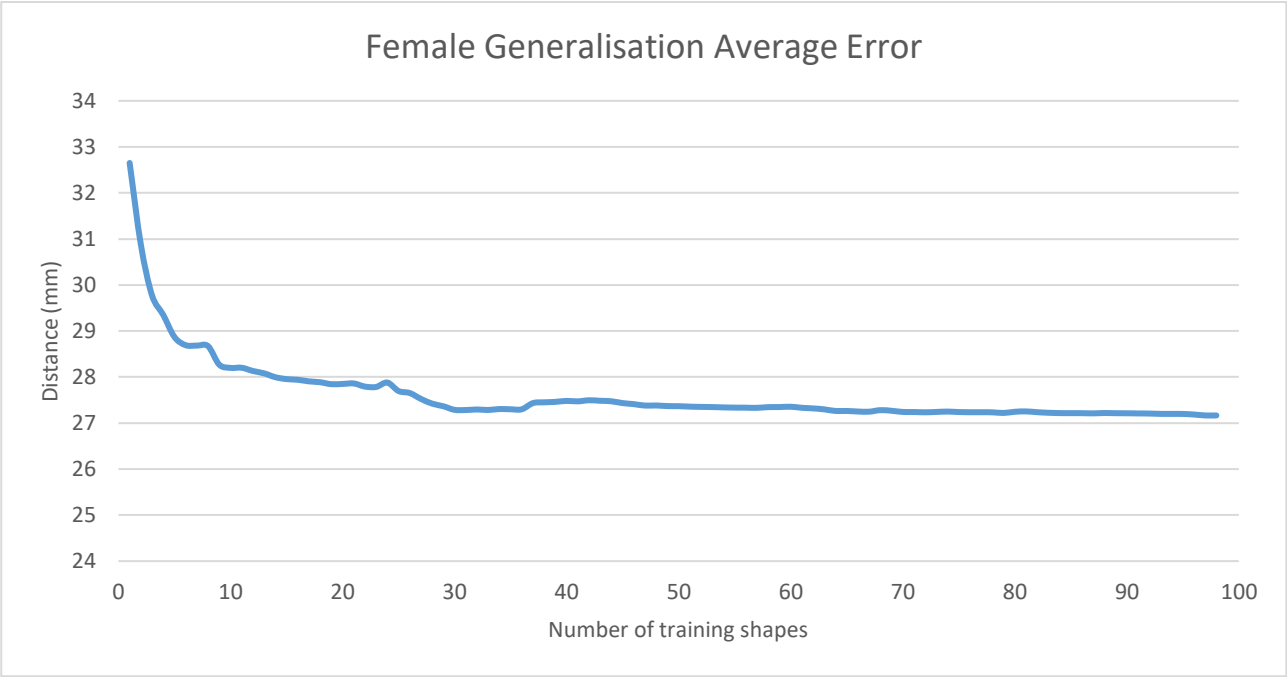

Figure 4.4: Female GPMM generalisation curve.

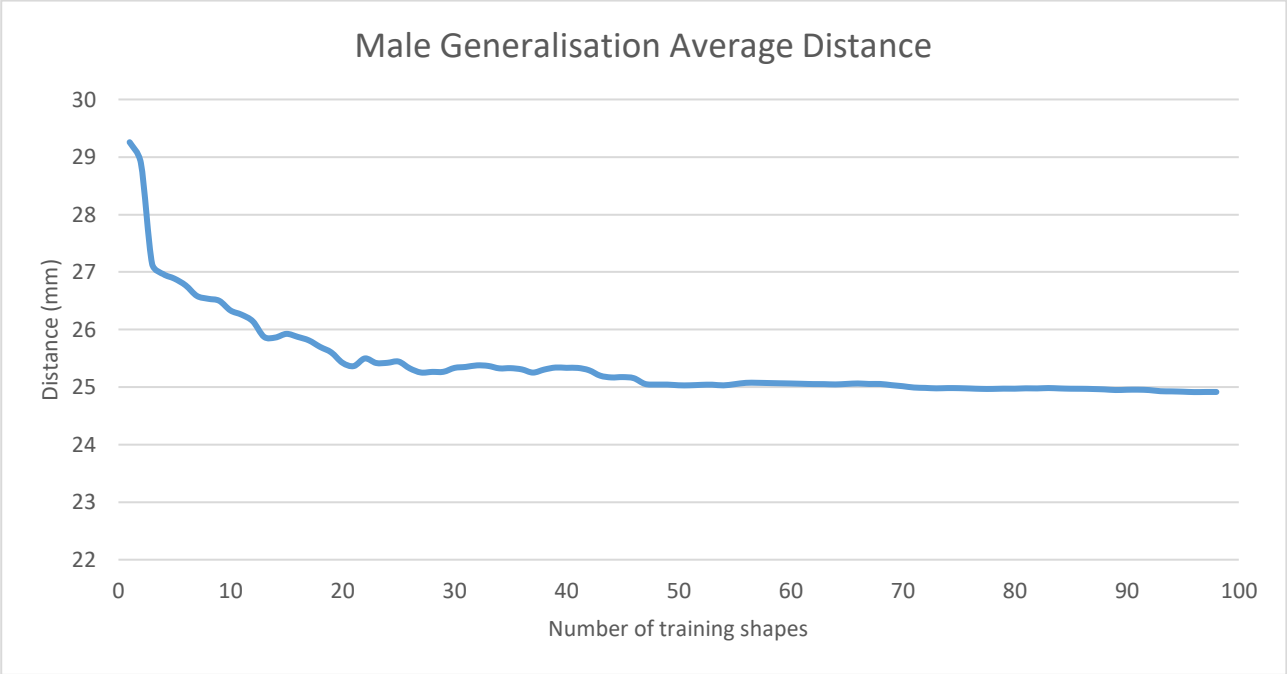

Figure 4.5: Male GPMM generalisation curve.

4.3.2 Specificity

The dataset was divided into training and testing datasets. The training data was used to build a model. The testing data was compared against to see whether the shapes produced by the model are all valid instances of body shapes. Testing began with building a GPMM using the training dataset. Several shapes were sampled and tested against the testing dataset to find the closest distance to a testing dataset

shape. The rank of the GPMM was then reduced by a ratio between the number of training and testing shapes. Sampling and distance evaluation are repeated. The surface-to-surface distance per vertex was used to evaluate the error between a mesh and its projected instance. Figure 4.6 and Figure 4.7 below show the specificity results for the female and male models. Each figure shows the average distance versus the number of modes. For both models, the average distance increases as the number of modes increases. The increase in distance lessens as the curve begins to plateau. The female model plateaued at 18.2 mm and the male model plateaued at 14.12 mm.

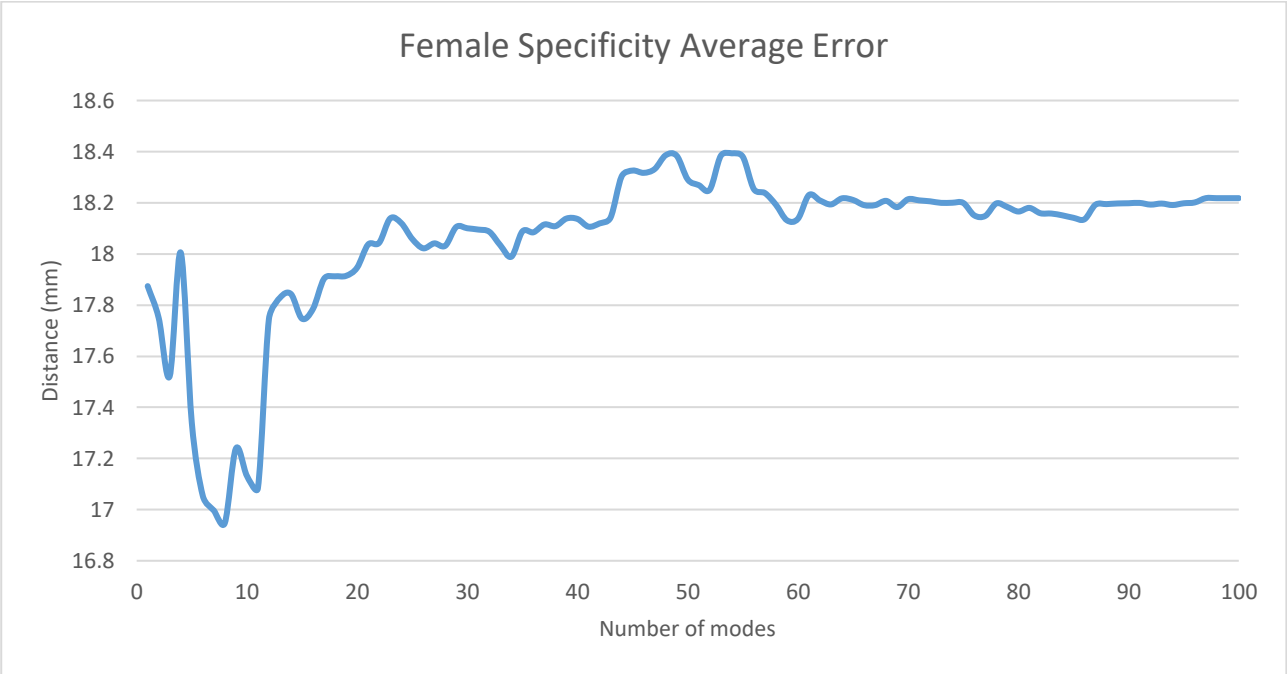

Figure 4.6: Female GPMM specificity curve.

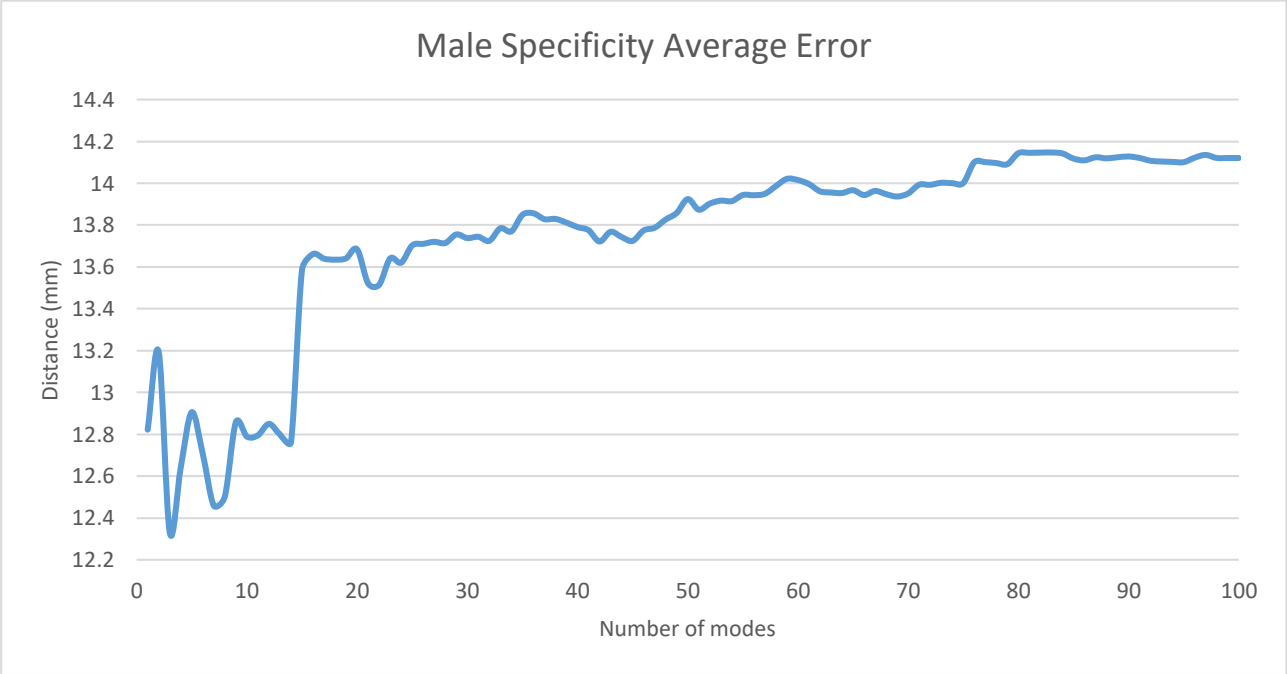

Figure 4.7: Male GPMM specificity curve.

4.3.3 *Compactness*

Compactness was assessed using the cumulative variance. The standard cumulative variance error was assessed to understand the error range when assessing how compact the model is (Davies, 2002). The equations are defined as follows (Styner et al., 2003). The cumulative variance is defined as:

$$\boldsymbol{C(M) = \sum_{i=1}^{M} \lambda_i} \tag{4.1}$$

Where λ_i is the i^{th} eigenvalue and M the number of modes. The standard error is defined as follows:

$$\boldsymbol{\sigma_{C(M)} = C(M)\sqrt{\frac{2}{n_s}}} \tag{4.2}$$

Where $C(M)$ is the cumulative variance and n_s the training set size. Following the example by Davies (2002), the number of modes containing 95% of the variance was assessed. Figure 4.8 and Figure 4.9 below show the cumulative variance versus the number of modes for both the female and male models, respectively. For the female model, the first 34 modes contain 95% of the model's variance. When considering the standard error, the range of modes is mode 21 to mode 81. For the male model, the first 33 modes contain 95% of the model's variance. When considering the standard error, the range of modes is mode 21 to mode 79.

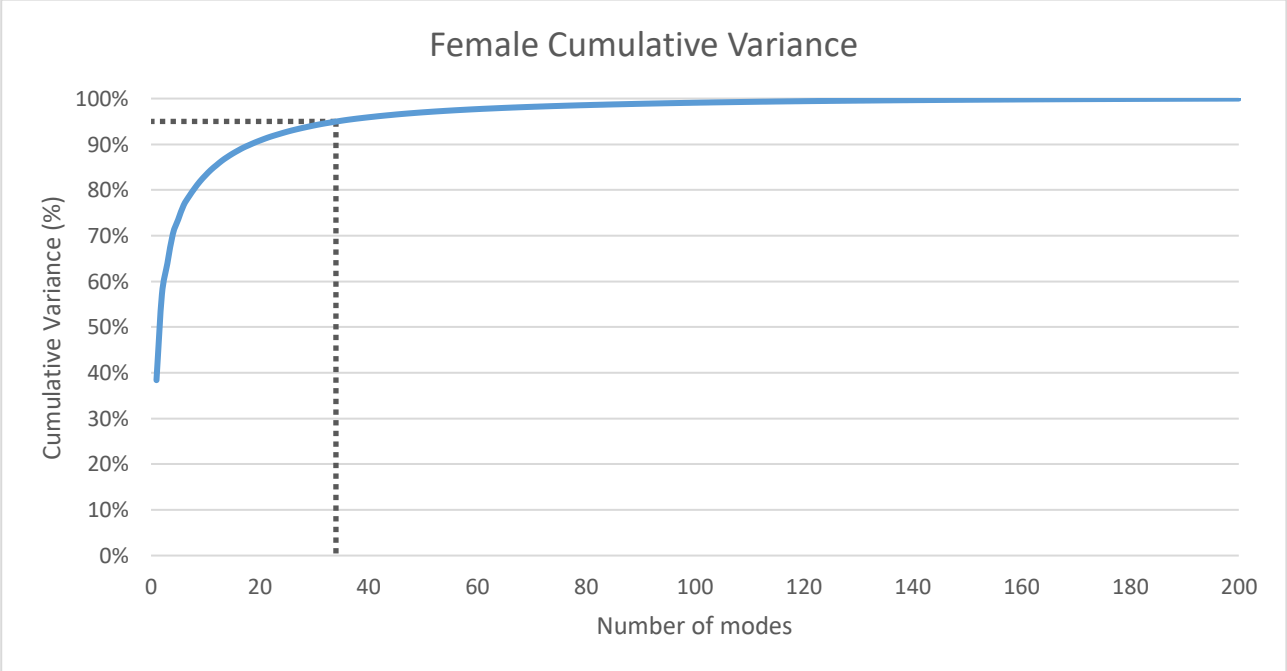

Figure 4.8: Female GPMM cumulative variance versus the number of modes.

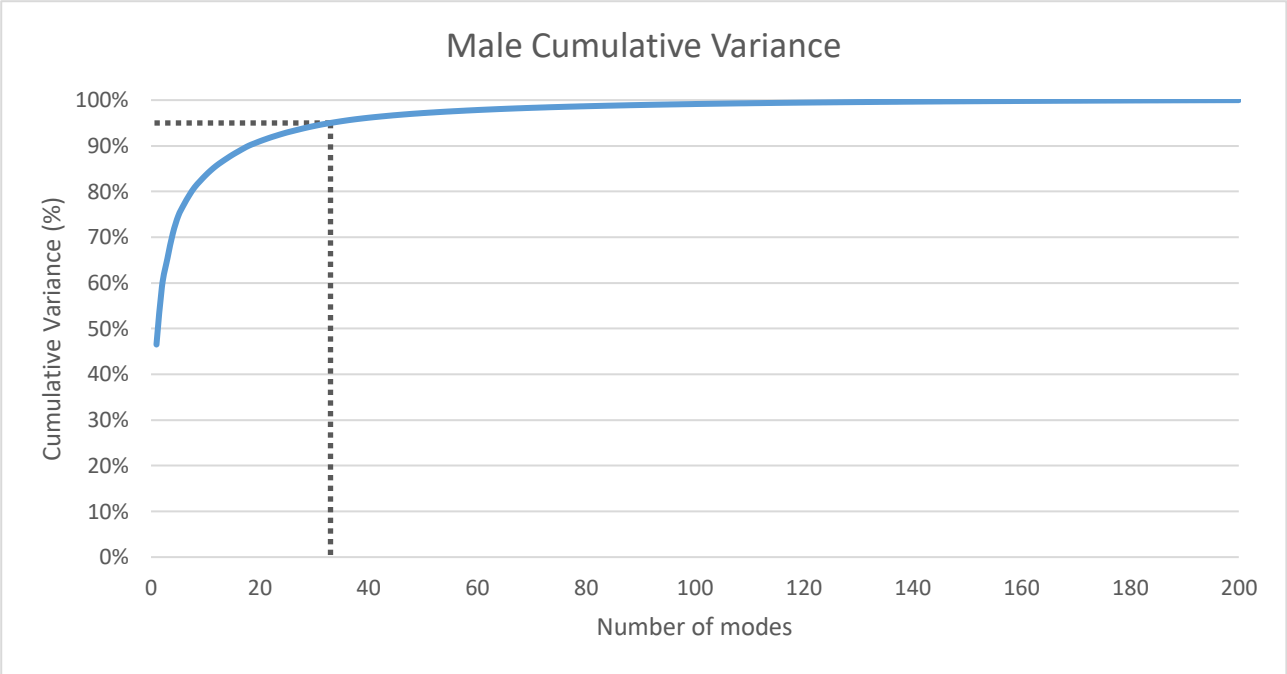

Figure 4.9: Male GPMM cumulative variance versus the number of modes.

4.4 Chapter Discussion

The GPMM produced models whose samples appear consistent with the human body shape. The quality of the models was assessed using generalisation, specificity, and compactness.

The generalisation average distance decreased as the number of training shapes used increased. This shape follows instances seen in shape modelling literature (Loper et al., 2015, Pishchulin et al., 2016, Styner et al., 2003). However. the errors value where the graphs plateaued are larger than those of 5 mm and 3 mm encountered in human body shape modelling literature (Loper et al., 2015, Pishchulin et al., 2017). Thus, the models display less generalisation compared to those in literature.

The specificity average distance increased as the number of training shapes increased. This shape follows instances seen in shape modelling literature (Pishchulin et al., 2017, Styner et al., 2003). However, the error values where the graphs plateaued are larger than the 5 mm encountered in human body shape modelling literature (Pishchulin et al., 2017). Thus, the models display less specificity compared to those in literature.

The compactness values showed that for the female and male models, 95% of the variation is contained within the first 34 and the first 33 modes, respectively. This shows that each model can use fewer modes without significant loss in variability. Even when considering the errors, 95% of the variation is contained in the first 81 and first 71 modes for the female and male models, respectively. Fewer modes than the current 200 can be used for the models.

There are limitations with the method used. The first limitation relates to the requirement for the training data to be in correspondence. This limits the possible datasets on which this method can be applied. However, this method can be used with the output of a registration and correspondence procedure. An additional limitation is the inability to describe pose variation. This limits the possible datasets and the potential applications of the models. Areas where improvements can be made include reducing the number of modes. Compactness and specificity showed the diminishing returns from having additional modes. The number of modes used is important as it affects the accuracy of the low-

rank approximation. The number of modes required for a desired accuracy for the low-rank approximation can be determined analytically as demonstrated by Lüthi et al. (2016).

The generalisation and specificity errors are larger than those identified in human body shape modelling literature (Loper et al., 2015, Pishchulin et al., 2017). A potential cause of the larger errors is the nature of the dataset, which was produced by Yang et al. (2014). Both Pishchulin et al. (2017) and Yang et al. (2014) made use of the same raw scan data when developing their datasets. However, in establishing registration and correspondence, the processes they applied differ. Pishchulin et al. (2017) included what they call bootstrapping - a manual check by a human who discarded unsatisfactory outputs. Outputs were considered unsatisfactory when they contained unrealistic shape and pose deformations. Additionally, they made use of pose normalisation to further minimise unrealistic pose deformations. Yang et al. (2014) did not make use of such checking and normalisation. This may have resulted in more unrealistic shape and pose deformations in their data. Pose differences were identified in the dataset and are described in detail later. The pose differences are incorrectly modelled as shape differences and may contribute to the lower performance of the model. Thus an additional source of error may be the lack of pose modelling.

Assessing the role of GPMMs in the error is difficult due to a lack of comparable applications with the full human body in the literature. However, comparisons can be made when considering specific body parts. Ploumpis et al. (2020) modelled the human head using GPMMs and compared the quality measures to the principal component analysis (PCA) based Liverpool-York Head Model (LYHM) (Dai et al., 2017). For generalisation, their model had an error of less than 1 mm compared to the LYHM which had an error of 2 mm. For specificity, their model error was 4 mm and that of the LYHM was 3.4 mm. Based on this comparison, the GPMM performs satisfactorily when assessing model quality.

The GPMM is unlikely to be a significant cause of error. The main source of error is most likely the inability to properly account for pose. This inability is magnified by a dataset which is known to contain pose differences.

5. Landmarks Used and their Reliability

Landmarks are used to define body dimensions and perform statistical analysis of the human body shape (Kouchi & Mochimaru, 2011). The accuracy of the landmarks will affect the accuracy of body dimensions and the results of analysis such as reconstruction. Therefore, it is important to assess the reliability of the manual placement of the landmarks. This chapter details the landmarks used in the research and describes the reliability tests performed for the landmarks that were used for model building, waist circumference (WC) tests, and reconstruction.

5.1 Landmarks

The full list of landmarks used in the research is in Table 5.1 below. Each row contains the name of the landmark, which image orientations they appear in, the definition, and a reference for the definition. The landmarks were mostly selected based on those used in traditional anthropometry and 3D anthropometry as described by Robinette et al. (2002b) with relevance to the measurements being considered. The list was refined by considering landmarks that lie along the silhouette of the body in the anteroposterior (AP) and lateral (LAT) views with the hope that tracing the silhouette would improve reconstruction and increase the accuracy of the body volume (BV) measurement.

Table 5.1: Landmarks used in research with descriptions and references (Robinette et al., 2002b).

Landmark	Images	Definition
acromion.lt	AP	Most lateral point of the lateral edge of the acromial process of the scapula (left)
acromion.rt	AP/LAT	Most lateral point of the lateral edge of the acromial process of the scapula (right)
crown	AP/LAT	The highest point of the head in the midsagittal plane
femoral-lateral-epi.lt	AP	Lateral point on the lateral epicondyle of the femur (left)
femoral-lateral-epi.rt	AP/LAT	Lateral point on the lateral epicondyle of the femur (right)
femoral-medial-epi.lt	AP	Medial point on the medial epicondyle of the femur (left)
femoral-medial-epi.rt	AP	Medial point on the medial epicondyle of the femur (right)
metatarsal-phalangeal.i.lt	AP	Maximum protrusion of the inside of the foot at the head of Metatarsus I (left)
metatarsal-phalangeal.i.rt	AP	Maximum protrusion of the inside of the foot at the head of Metatarsus I (right)
metatarsal-phalangeal.v.lt	AP	Maximum protrusion of the inside of the foot at the head of Metatarsus V (left)
metatarsal-phalangeal.v.rt	AP/LAT	Maximum protrusion of the inside of the foot at the head of Metatarsus V (right)
radial-styloid.lt	AP	Distal tip of the radius (left)
radial-styloid.rt	AP/LAT	Distal tip of the radius (right)
supramenton	AP/LAT	Point of the greatest indentation of the jaw in the horizontal midpoint
thelion-bustpoint.lt	AP	Most anterior protrusion of the bra cup on women or centre of nipple on men (right)
thelion-bustpoint.rt	AP/LAT	Most anterior protrusion of the bra cup on women or centre of nipple on men (left)
trochanterion.lt	AP	Top of the bony lateral protrusion of the proximal end of the femur (left)
trochanterion.rt	AP	Top of the bony lateral protrusion of the proximal end of the femur (right)
waist.anterior	AP/LAT	Marked at the midpoint between the lower margin of the last palpable rib and the top of the iliac crest. Marked on the anterior

waist.lt	AP	Marked at the midpoint between the lower margin of the last palpable rib and the top of the iliac crest. Marked on the subject's left side at the waist level
waist.posterior	LAT	Marked at the midpoint between the lower margin of the last palpable rib and the top of the iliac crest. Marked on the posterior of the subject
waist.rt	AP/LAT	Marked at the midpoint between the lower margin of the last palpable rib and the top of the iliac crest. Marked on the subject's right side at the waist level

5.2 Method

For each set of landmarks, guides were created containing the landmark definitions. Two trained operators placed landmarks across two sessions more than 24 hr apart. Intra- and inter-operator variability were determined using the distance between the mean position and the observed position (Altman & Bland, 1983). Intra- and inter-operator variability were calculated using the following equations (Victor et al., 2009):

$$\bar{P}(\bar{x},\bar{y},\bar{z}) \rightarrow \begin{matrix} \bar{x} = \dfrac{x_1 + x_2}{2} \\ \bar{y} = \dfrac{y_1 + y_2}{2}, \\ \bar{z} = \dfrac{z_1 + z_2}{2} \end{matrix} \qquad D_i = \|\bar{P} - P_i\| = \sqrt{(\bar{x} - x_i)^2 + (\bar{y} - y_i)^2 + (\bar{z} - z_i)^2} \tag{5.1}$$

The mean landmark position $\bar{P}$ is determined from the mean coordinate values. The distances D_i are the difference between the mean position and a given landmark. The mean of the distances D_i was used to measure the overall intra-operator error. For inter-operator variability, the mean positions were calculated using the mean for each operator.

$$\bar{\bar{P}}(\bar{\bar{x}},\bar{\bar{y}},\bar{\bar{z}}) \rightarrow \begin{matrix} \bar{\bar{x}} = \dfrac{\overline{x_1} + \overline{x_2}}{2} \\ \bar{\bar{y}} = \dfrac{\overline{y_1} + \overline{y_2}}{2}, \\ \bar{\bar{z}} = \dfrac{\overline{z_1} + \overline{z_2}}{2} \end{matrix} \qquad D_i = \left\|\bar{\bar{P}} - \overline{P_i}\right\| = \sqrt{(\bar{\bar{x}} - x_i)^2 + (\bar{\bar{y}} - y_i)^2 + (\bar{\bar{z}} - z_i)^2} \tag{5.2}$$

The same calculations are performed but the mean position and distances are derived from the intra-operator means. For the 2D images, the *x* and *y* coordinates are considered, and the values are in pixels. It is necessary to define a standard to understand the landmark errors. Mutsvangwa et al. (2009) define the following thresholds when considering the precision of landmarks on 3D face scans:

- $<$ 1 mm – highly precise
- $\leq$ 1 mm & $\leq$ 1.5 mm – precise
- $\leq$ 1.6 mm & $\leq$ 2 mm – moderately precise
- $<$ 2 mm – less precise

Kouchi & Mochimaru (2011) consider landmark errors above 10 mm to be large errors. Based on this, the following criteria for body landmark precision are defined:

- $<$ 5 mm – highly precise
- $\leq$ 5 mm & $\leq$ 7.5 mm – precise
- $\leq$ 7.6 mm & $\leq$ 10 mm – moderately precise
- $<$ 10 mm – less precise

When considering the image landmarks, it is important to note that the size of a pixel is dependent on the specifications of the display. The real-world distance in those pixels is further dependent on the pixel size, magnification of the image, and the real-world size of the object. Thus, global criteria in pixels cannot be defined as the real-world size will vary for each body. However, once these factors are accounted for and the pixel distance converted to real-world distance then the criteria can be applied. Section 5.4.3 provides an example of the conversion from pixels to millimetres.

The coordinate values were used to measure intra- and inter-operator reliability. Reliability was tested using the intraclass correlation coefficient (ICC). The formulas for ICC were selected using the criteria defined by Koo & Li (2016). The ICC test used a two-way random effects model, it used the mean of k raters, and it sought absolute agreement. These classifications led to the following equation (McGraw & Wong, 1996):

$$\boldsymbol{ICC = \frac{MS_R - MS_E}{MS_R + \frac{MS_C - MS_E}{n}}} \tag{5.3}$$

Where MS_R is the mean square for rows, MS_E is the mean square error, MS_C is the mean square for columns, and n is the number of subjects. Intraclass correlation coefficient values were calculated using SPSS Statistics (*IBM, Armonk, New York, United States*). SPSS implements ICC calculations based on the terminology by McGraw & Wong (1996). The ICC values were assessed classified using the following criteria (Koo & Li, 2016):

- < 0.5 – poor reliability
- ≤ 0.5 & < 0.75 – moderate reliability
- ≤ 0.75 & < 0.9 – good reliability
- ≤ 0.9 – excellent reliability

5.3 Results

5.3.1 Model Landmarks

Intra-operator ICC for the model landmarks was 0.99 for *x*, 1.00 for *y*, and 0.99 for *z*. Figure 5.1 below shows the mean inter-operator distance for each landmark. The smallest distance was 4.00 mm and was for the supramenton. The largest distance was 37.99 mm and was for the right femoral lateral epicondyle. The mean distance for all landmarks was 12.87 mm.

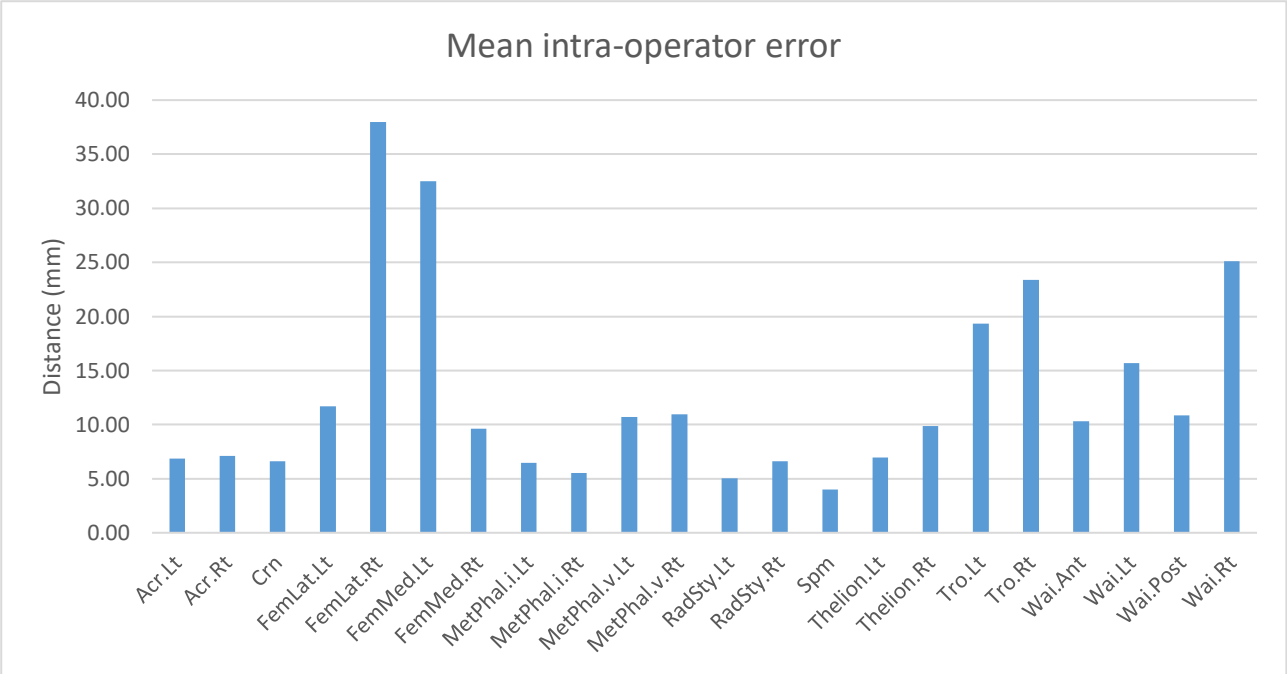

Figure 5.1: Mean intra-operator distance for model landmarks.

Inter-operator ICC for the model landmarks was 0.99 for *x*, 1.00 for *y*, and 0.99 for *z*. Figure 5.2 below shows the mean inter-operator distance for each landmark. The smallest distance was 6.13 mm and was for the supramenton. The largest distance was 41.12 mm and was for femoral lateral epicondyle right. The mean distance for all landmarks was 15.14 mm.

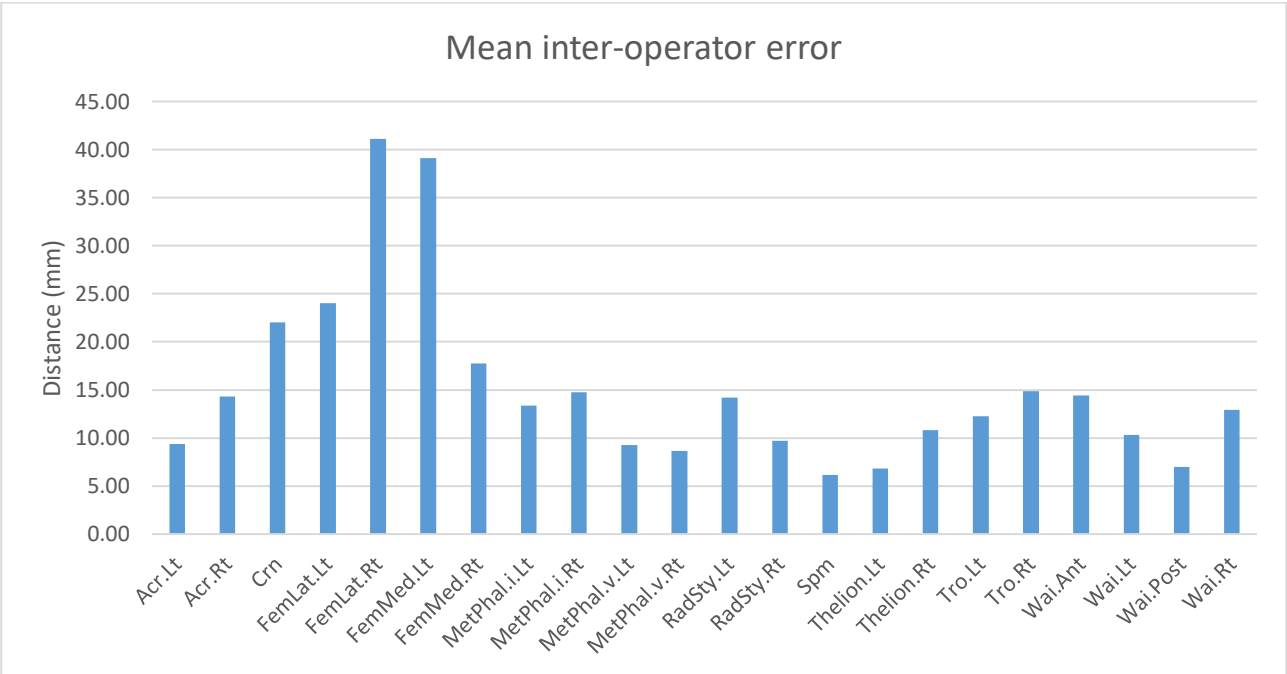

Figure 5.2: Mean inter-operator distance for model landmarks.

5.3.2 Waist Circumference Landmarks

The landmarks used for WC measurement are waist anterior, waist posterior, and waist right. Intra-operator ICC for the waist circumference landmarks was 1.00 for *x*, 0.87 for *y*, and 1.00 for *z*. Figure 5.3 below shows the mean inter-operator distance for each landmark. The mean distance was 11.69 mm for waist anterior, 9.39 mm for waist posterior, and 15.15 mm for waist right.

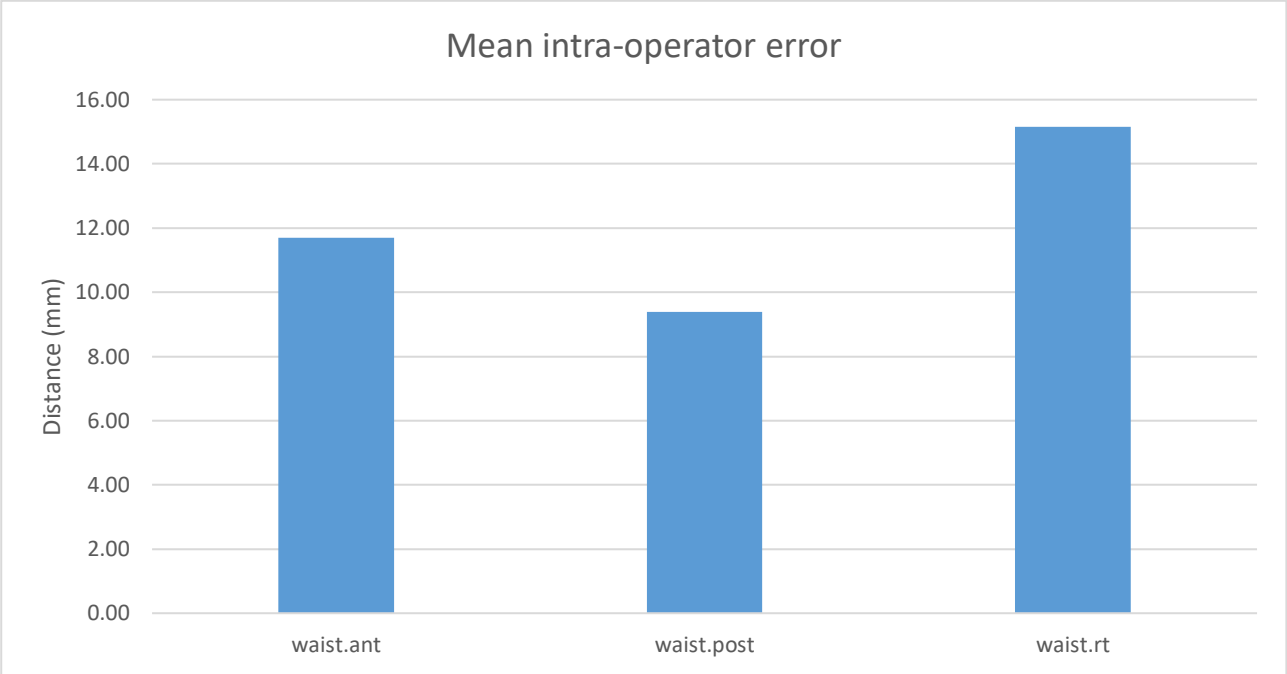

Figure 5.3: Mean intra-operator distance for WC landmarks.

Inter-operator ICC for the waist circumference landmarks was 1.00 for *x*, 0.24 for *y*, and 1.00 for *z*. Figure 5.4 below shows the mean inter-operator distance for each landmark. The mean distance was 25.83 mm for waist anterior, 25.93 mm for waist posterior, and 30.16 mm for waist right.

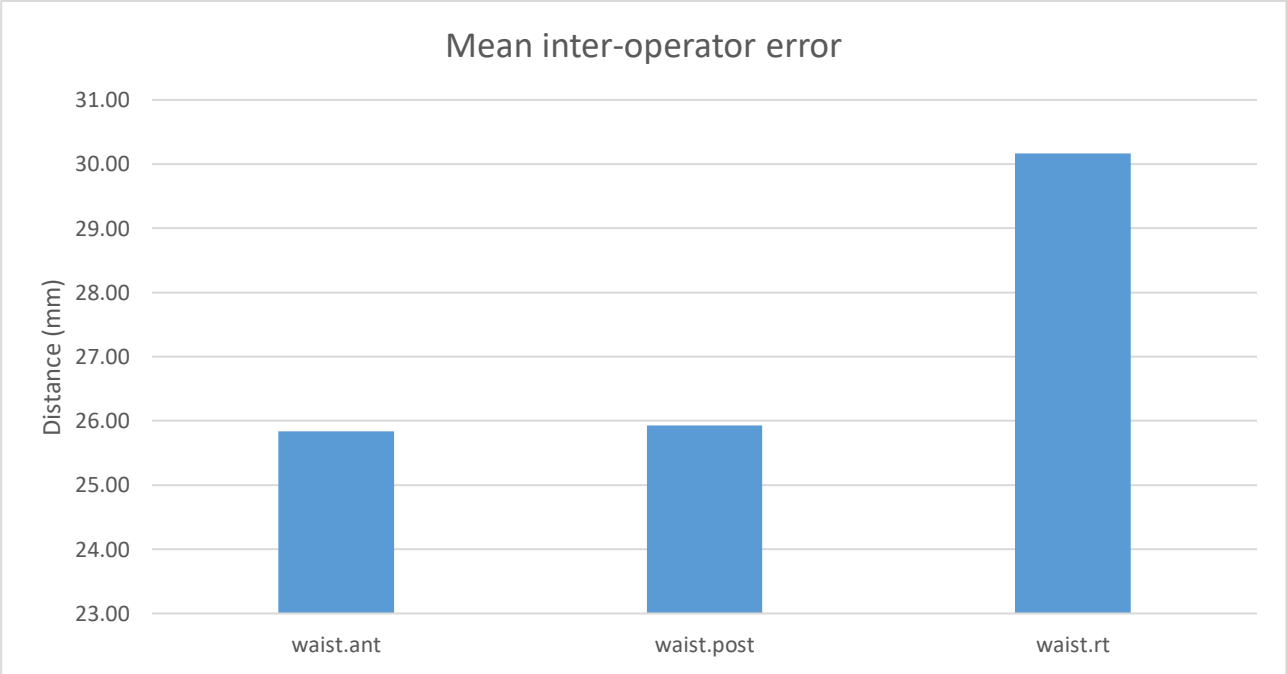

Figure 5.4: Mean inter-operator distance for WC landmarks.

5.3.3 Image Landmarks

Intra-operator ICC for the image landmarks was 1.00 for *x* and 1.00 for *y*. Figure 5.5 below shows the mean inter-operator distance for each landmark. The mean distance for all landmarks was 2.84 px.

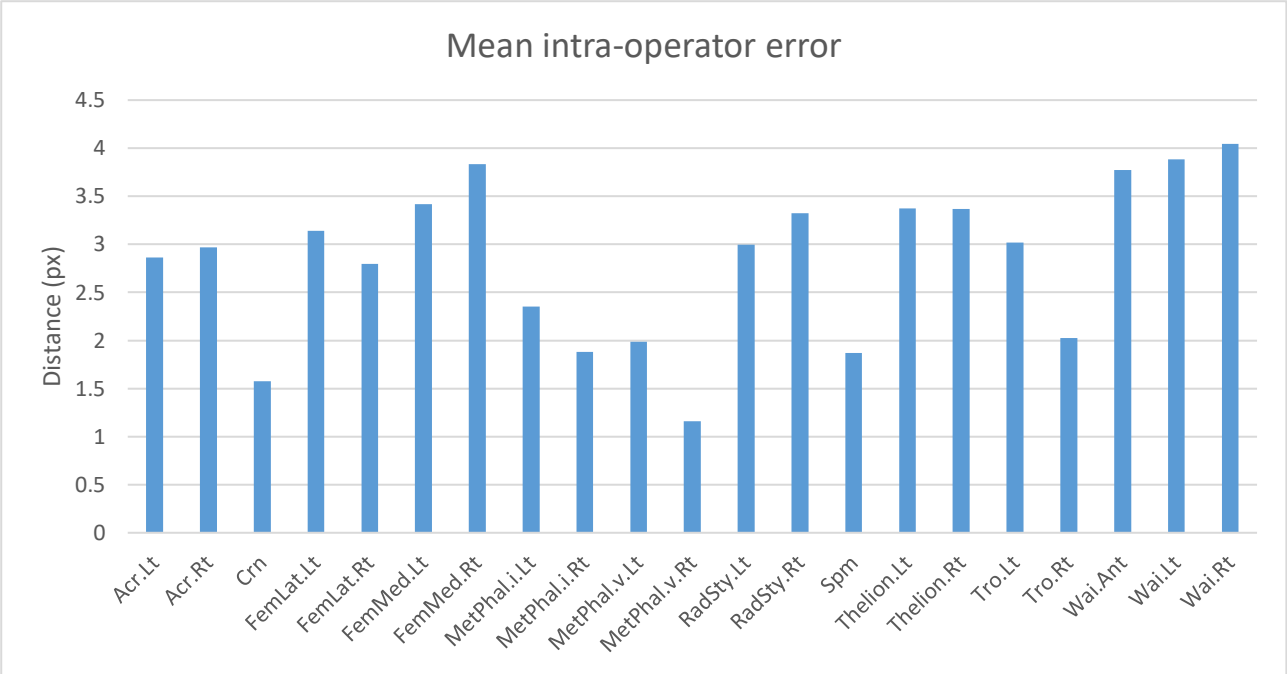

Figure 5.5: Mean intra-operator distance for image landmarks.

Inter-operator ICC for the image landmarks was 1.00 for *x* and 1.00 for *y*. Figure 5.6 below shows the mean inter-operator distance for each landmark. The mean distance for all landmarks was 4.14 px.

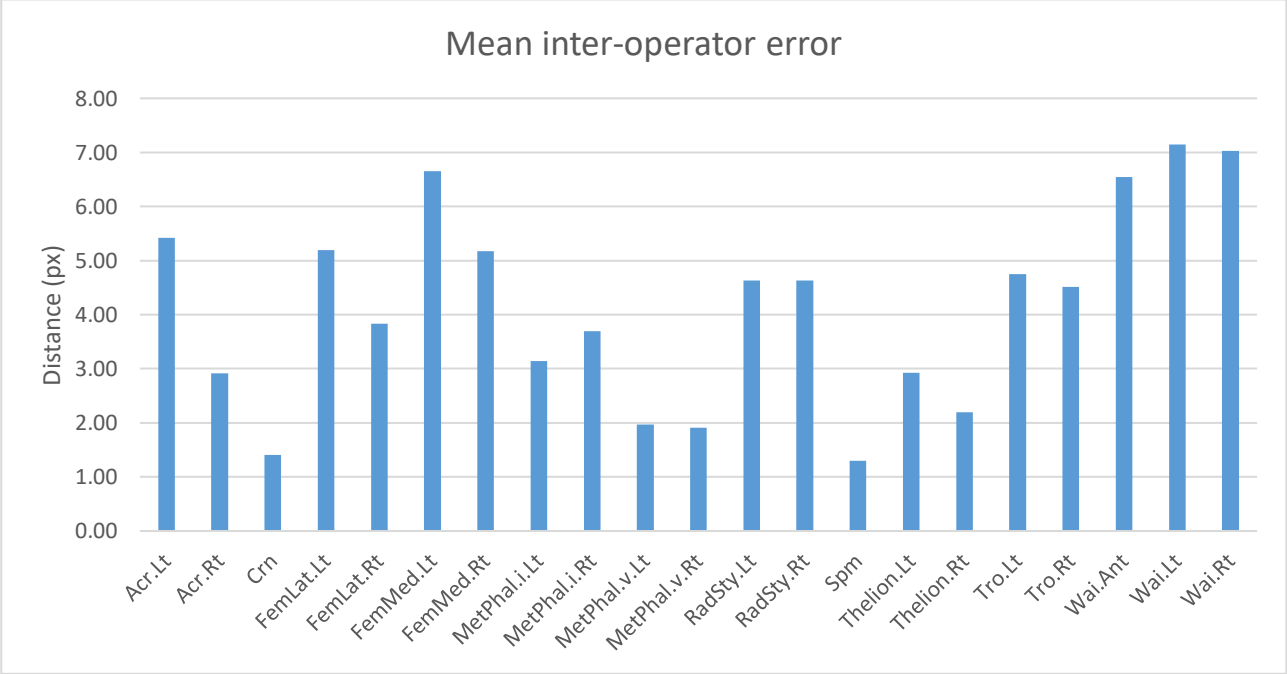

Figure 5.6: Mean inter-operator distance for image landmarks.

5.4 Chapter Discussion

5.4.1 Model Landmarks

The model landmarks showed excellent intra- and inter-operator reliability. The high ICC values are consistent with prior findings (Kouchi & Mochimaru, 2011, Victor et al., 2009, Zancanaro et al., 2015). Despite the high reliability, intra- and inter-operator errors of 12.87 mm and 15.14 mm were recorded.

These errors indicate low precision. Altogether this means the landmarks are consistently placed but in the wrong position.

The literature reports wide variation in precision. Errors of 20 mm were reported by Azouz, Shu & Mantel (2006), while Xiaohui et al., 2018) reported errors of 0.62 mm. The error varied from landmark to landmark. Landmarks such as the supramenton and metatarsal-phalangeal V had intra- and inter-operator errors less than 10 mm and can considered to be moderately precise. Landmarks such as femoral-epicondyle had errors greater than 20 mm and 35 mm in some cases. The differences across landmarks may be the result of varying levels of difficulty in identifying different landmarks.

5.4.2 Waist Circumference Landmarks

The WC landmarks showed excellent intra- and inter-operator reliability for most coordinates. However, the *y* coordinate showed good intra-operator reliability and poor inter-operator reliability. The mean error values are considered less precise based on the precision criteria. The comparisons to literature match what was seen for the model landmarks regarding precision and reliability. The consistency in error for both intra- and inter-operator appears to stem from the landmark selection procedure. The first landmark selected is waist anterior. Its horizontal position is the midpoint of the coronal plane. The vertical position is defined by the most concave point on the right side of waist when viewed from the front (International Organization for Standardization, 2016). Waist right and waist posterior are then selected with the vertical position corresponding to waist anterior. An inability to correctly locate the vertical point of the greatest curvature is demonstrated by the poor inter-operator reliability for the *y* coordinate. Most errors were above 10 mm indicating less precise landmarks.

5.4.3 Image Landmarks

The image landmarks showed excellent intra- and inter-operator reliability. The mean differences were 2.84 px and 4.14 px for intra- and inter-operator. In quantifying the errors, it is necessary to evaluate the size of a pixel. The size of the pixel displayed is further dependent on the display and the magnification of the images. Each image was displayed on a Samsung S24E930HL monitor[3] (*Samsung, Seoul, Gyeonggi-do, South Korea*). The height and width of each pixel is 0.2715 mm (Samsung, 2019). A range for real-world distance range can be calculated using the size of a pixel or the distance from the centre of a pixel to a corner. Assuming each image was at 100% magnification, the real-world distances are less than 1 mm for both intra- and inter-operator. However, the images undergo scaling based on the real height of the person. Therefore, the overall scale of the landmark error is dependent on the height of the person. To illustrate, an example based on the test data is described. The full nature of the scaling is discussed in section 7.2.2. Assuming the pixel height is 725 px and the real height is 1600 mm, the pixel errors are 6.27 px and 9.14 for intra- and inter-operator error. This results in a real-world error of less than 2 mm. The actual values will vary per image, but the example illustrates how small the errors can be. Errors of this magnitude result in highly precise landmarks.

5.4.4 Summary

Operators were found to be consistent in most of the tasks. However, for the model landmarks and WC landmarks, the landmarks were found to be less precise based on the defined criteria. The errors were also larger than some errors encountered in literature. The model and WC landmark errors were all larger than 5 mm, which is the threshold for high precision (Kouchi & Mochimaru, 2011). The image landmark errors were found to be small and are considered highly precise. The image real-world error differed from the model landmark errors. Several factors may be responsible. The image landmark software features crosshairs that span the height and width of the image. It also contains integrated

[3] https://www.samsung.com/africa_en/monitors/led-se390/

guide images. Additionally, placing the image landmarks does not require moving the image. The model landmark software has small crosshairs which makes it difficult to place landmarks relative to one another. Additionally, the object undergoes rotation when being landmarked. The lack of crosshairs, lack of guide images, the additional movement, and the difficulty in identifying certain landmarks may contribute to the larger model landmark errors. The landmark errors will limit the accuracy of WC measurements and reconstruction.

6. Body Measurements

Beyond 3D reconstruction, the system also needs to measure body dimensions for assessing body composition. This section describes the methods and tests used in the implementation of algorithms to measure body volume (BV), height, and waist circumference (WC).

6.1 Anatomical Planes

References are made to anatomical planes and axes in this chapter. Figure 6.1 below shows the planes and the axis system.

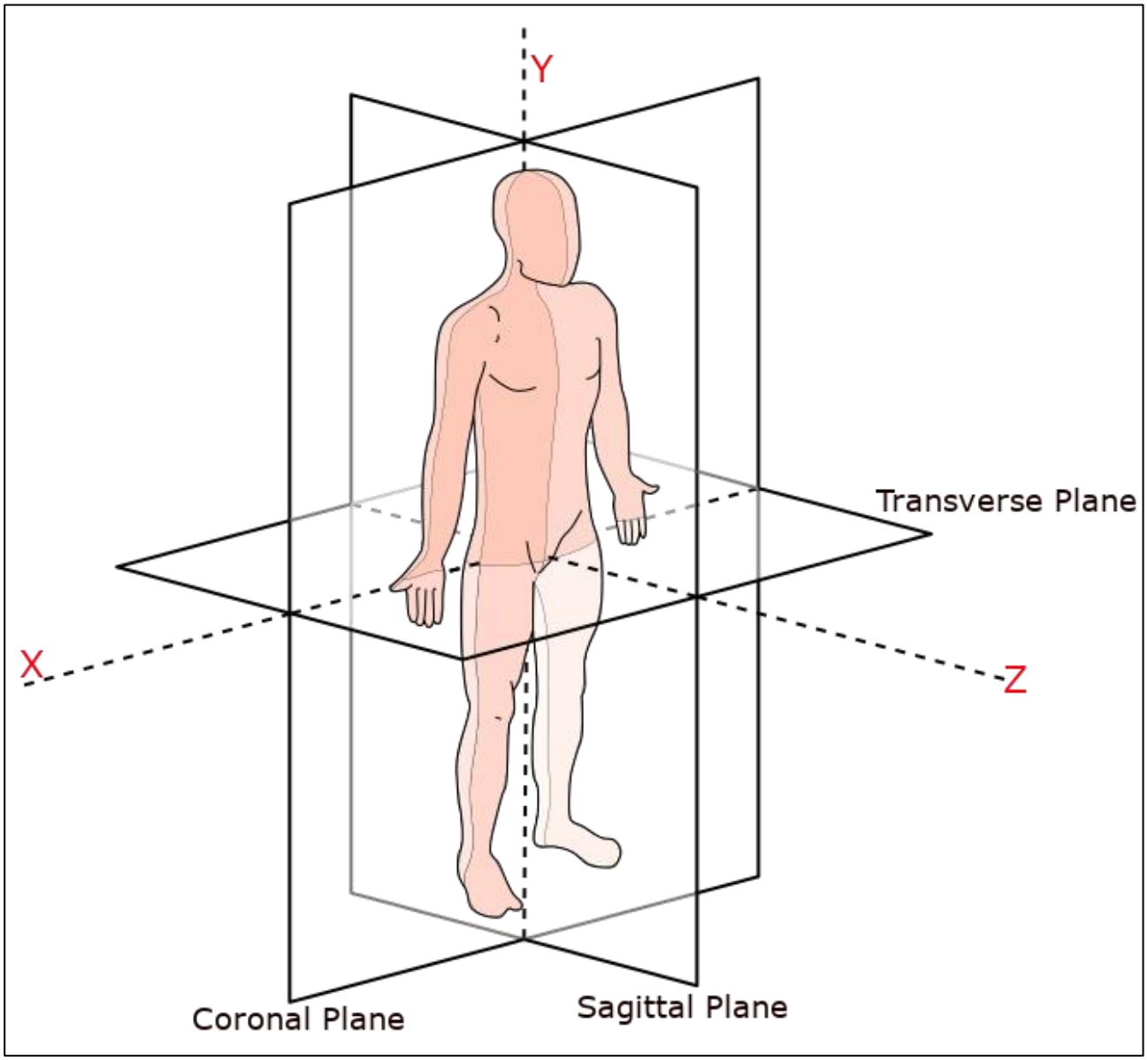

Figure 6.1: Anatomical planes and the axis system. (Image: (CFCF, 2014) Licensed under Creative Commons Attribution-Share Alike 3.0 Unported (Creative Commons, 2009))

6.2 Body Volume Measurement

This section describes the BV measurement dataset with descriptions of the different types of data and example images. A change in volume is expected when an object is discretised. The level of loss is dependent on the type of object. Thus, it is necessary to evaluate the different types of objects to assess how they affect the accuracy of the algorithm. Additionally, the algorithm used to measure volume and

the tests performed to validate the algorithm are also described. Part of the testing also considers the effect of the digitisation of objects into the STL format on the volume.

6.2.1 Dataset

The dataset consists of objects in four classes. These classes are:

- Cube
- Sphere
- Arbitrary
- Human body

The classes of objects will each experience different levels of discretisation during conversion to the STL format. The level of discretisation affects the volume of the STL object versus the regular object. The test sought to assess the accuracy of the volume measurement for different object classes.

i. Cubes

This class consists of two cubes with lengths of 100 mm and 1000 mm, respectively. Volume was calculated by taking the lengths to the power of 3.

ii. Sphere

This class consists of two spheres with radii of 50mm and 500mm, respectively. Volumes was calculated using the following equation (Olver et al., 2010):

$$\boldsymbol{V = \frac{4}{3}\pi r^3} \tag{6.1}$$

Where $\boldsymbol{V}$ is the volume and r is the radius.

iii. Arbitrary

This class consists of six human-generated objects. The objects were created using SolidWorks (*Dassault Systèmes, Vélizy-Villacoublay, Île-de-France, France)*. The volumes were determined using the volume measurement tool in SolidWorks. The volumes were measured before conversion to the STL format. Figure 6.2 below shows the objects in the class.

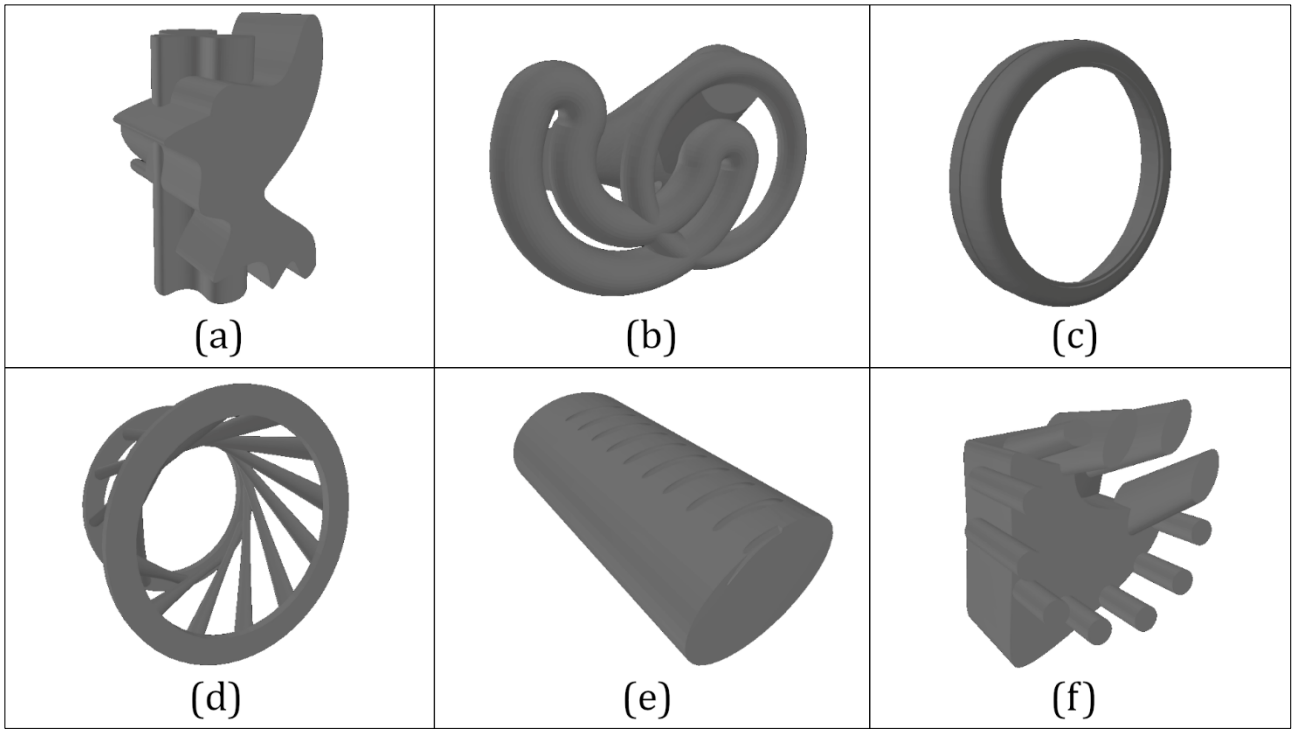

Figure 6.2: Objects in the arbitrary class.

iv. ***Human Body***

This class consists of 56 human bodies from the Inkreate dataset. The ground truth volumes come with the dataset.

6.2.2 ***Method***

The method to measure volume used the Visualization Toolkit (VTK)[4] (*Kitware, New York, New York, United States of America*) software library. The mesh was converted into a format compatible with the VTK library. The VTK volume measurement method[5] was then used to measure the volume. Testing compared measured volumes against ground truth volumes.

6.2.3 ***Results***

i. ***Cube***

The results of the cube volume tests are in Table 6.1 below. The measured volumes were the same as the ground truth volumes.

Table 6.1: Cube volumes showing the ground truth and measured volume.

Ground Truth (mm^3)	Measured Volume (mm^3)
$\mathbf{1 \times 10^9}$	1×10^9
$\mathbf{1 \times 10^6}$	1×10^6

ii. ***Sphere***

The results of the sphere volume test are in Table 6.2 below. The measured volumes were smaller for both spheres. The percentage difference was 0.273% for both spheres.

[4] https://gitlab.kitware.com/vtk/vtk
[5] https://vtk.org/doc/nightly/html/classvtkMassProperties.html#aaac0b71d49959de0d2ca8520d7c3ca54

Table 6.2: Sphere volumes showing the ground truth, measured volume, and percentage difference.

Ground Truth (mm^3)	Measured Volume (mm^3)	Difference
$\mathbf{5.24 \times 10^8}$	5.22×10^8	0.27%
$\mathbf{5.24 \times 10^5}$	5.22×10^8	0.27%

iii. Arbitrary

The results of the arbitrary object test are in Table 6.3 below. For every object the measured volume was lower than the ground truth.

Table 6.3: Arbitrary object volumes showing the ground truth, measured volume, and percentage difference.

Ground Truth (mm^3)	Measured Volume (mm^3)	Difference
$\mathbf{9.65 \times 10^4}$	9.64×10^4	0.19%
$\mathbf{2.48 \times 10^5}$	2.48×10^5	0.32%
$\mathbf{3.94 \times 10^5}$	3.94×10^6	0.00%
$\mathbf{2.41 \times 10^{11}}$	2.41×10^{11}	0.13%
$\mathbf{5.70 \times 10^5}$	5.44×10^5	4.50%
$\mathbf{2.33 \times 10^5}$	2.32×10^5	0.15%

iv. Human Body

Figure 6.3 below shows the percentage differences between the ground truth volumes and the measured volumes for the human body object class. For most cases the measured volumes were smaller than the ground truth. The largest difference was 1.28%. The average difference was 0.47%.

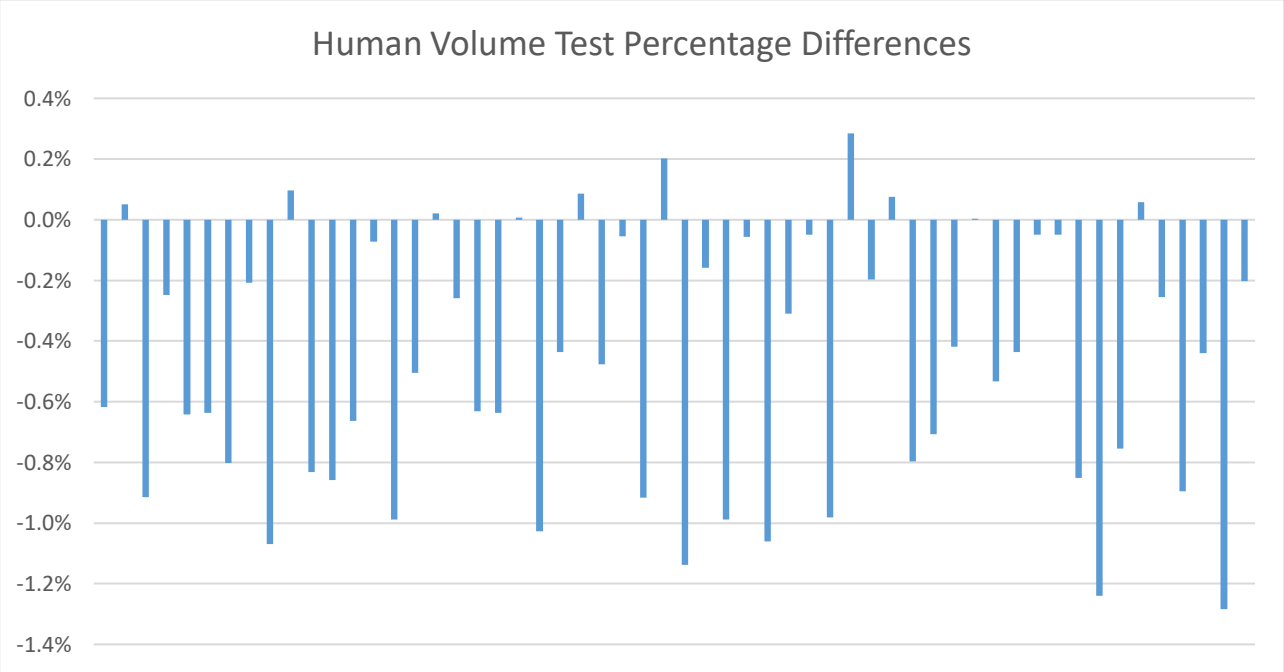

Figure 6.3: Human BV test percentage differences.

6.2.4 Discussion: Volume

The accuracy of the volume measurement method is a dependent on the complexity of the object. This can be seen with the cube volumes being 100% accurate regardless of the size and the sphere volume having a constant error. For arbitrary objects, the error varied from 0.00% up to 4.50%. For human bodies, the average error was very small in a negative direction. The small average error shows the suitability of the VTK volume measurement method to measure the volume of human bodies in the STL

format, since the magnitude of the error is in line with those in the literature. Errors have ranged from 0.12% for air displacement plethysmography (Dewit et al., 2000) to 1.5% for 3D scanners (Adler et al., 2017). The applicability of the method to other arbitrary objects varies and further analysis of the class of object being measured is required to draw further conclusions.

6.3 Height Measurement

This section describes the height measurement data, algorithm, and tests. Even though BMI is limited, it still has relevance when combined with other measurements. Thus, the measurement of height is necessary as it allows for calculation of BMI. The allowable error for height measurements is 6 mm as described in section 2.2.1.

6.3.1 Dataset

The dataset consists of 56 human body meshes from the Inkreate dataset. The ground truth height values were bundled with the dataset. Height is defined as the vertical distance between the landing heel point and the top head point in the standing position (International Organization for Standardization, 2016). The landing heel point is the lowest point of the posterior calcaneus and the top head point is the highest point of the head in the midsagittal plane. Figure 6.4 below shows an example of height measurement. The crown and landing heel point are indicated with red dots and labels. The height is measured in the sagittal plane which is the plane outlined in yellow through the middle of the body.

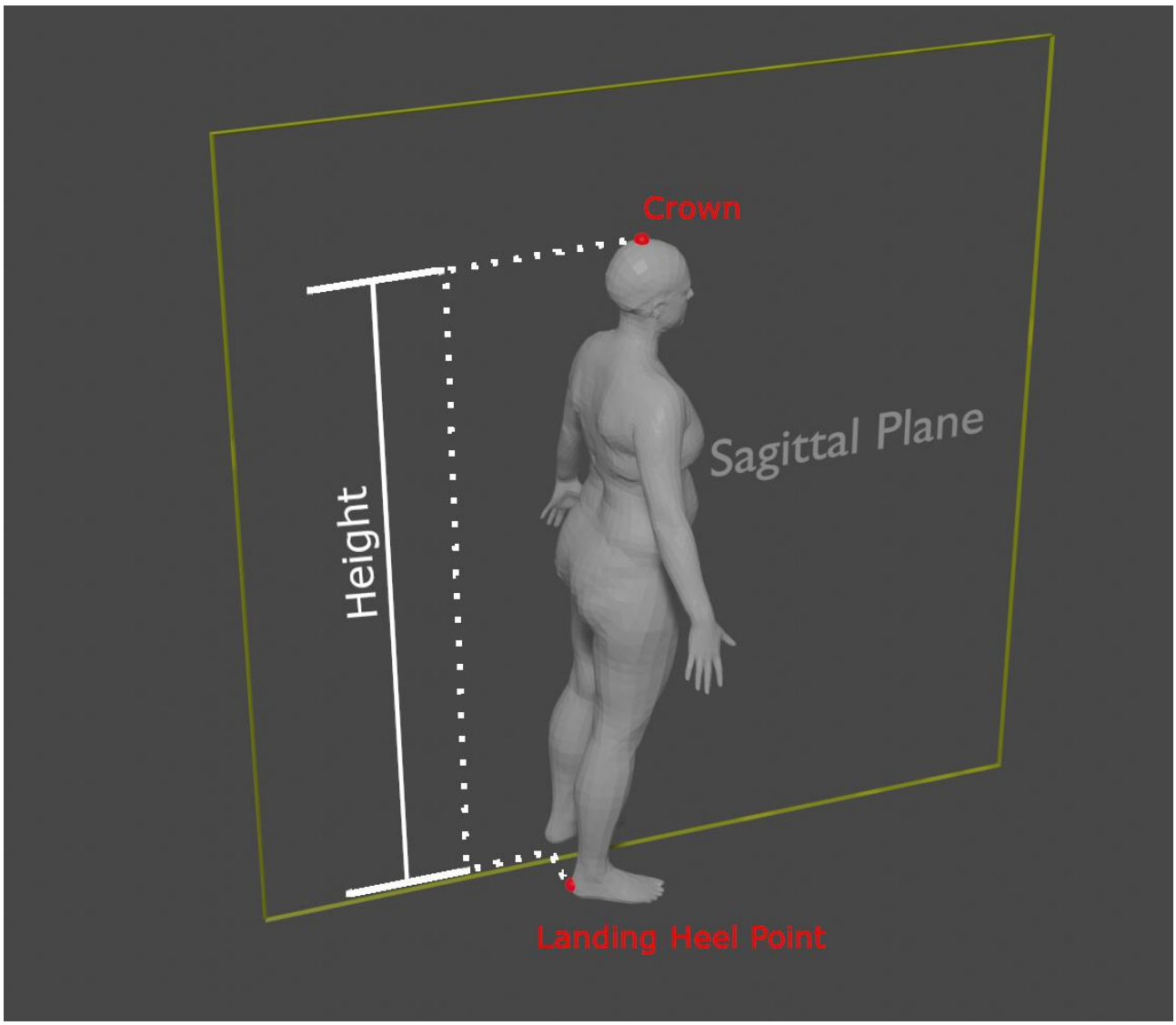

Figure 6.4: Example of height measurement showing the crown and landing heel point.

6.3.2 Method

The method to measure height from a mesh is dependent on the mesh being aligned as seen in Figure 6.1 above. If so, height can be determined using the minimum and maximum *y* coordinate values. The maximum *y* coordinate serves as the top head point and the minimum *y* coordinate serves as the posterior calcaneus. The absolute value of the difference between the maximum and minimum produces the height.

6.3.3 Results

The height for each mesh was measured and evaluated against the ground truth. The MD and MAD were then determined. Figure 6.5 below shows the percentage differences between the ground truth and measured heights for the human bodies test. The average difference was 0.02%. The error was mostly negative. The MD and MAD are shown in Table 6.4 below. The MD is 0.32 mm and the MAD is 0.36 mm.

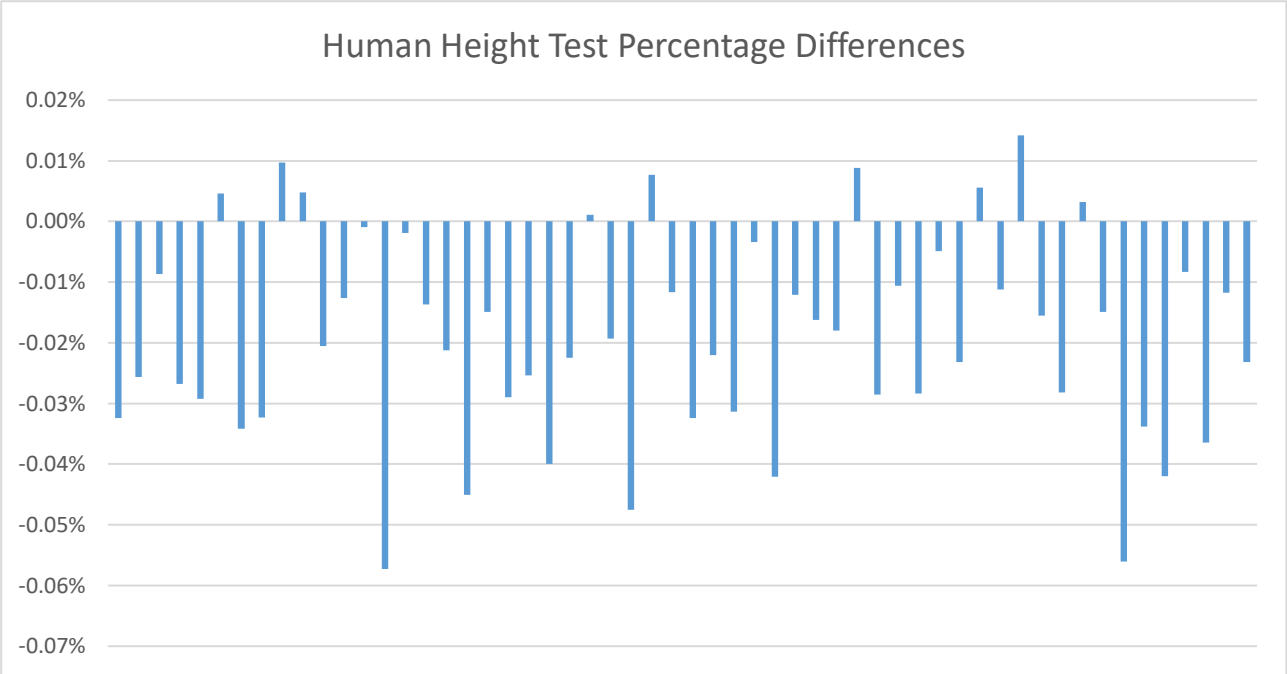

Figure 6.5: Human body height test percentage differences.

Table 6.4: MD and MAD for the human body height test.

MD (mm)	MAD (mm)
0.32	0.36

6.3.4 Discussion: Height

The method consistently underestimates the height. However, the small size of the error shows that the method is suitable to measure the height of human bodies provided the required conditions are met. The magnitude of the errors is smaller than the allowable error of 6 mm for height described by Gordon et al. (2014) and mentioned in section 2.2.1. In comparing the results to those of other studies, it is necessary to consider the error contained within the dataset itself. This is necessary as the method compared the height of a 3D mesh against the mesh heights provided with the dataset, whereas other studies typically compare the height of a 3D mesh against a real-world height. The dataset itself has an error of 2 mm (Bogo et al., 2014b) which results in an overall error of 2.36 mm. This is less than the error of 7.5 mm (Han, Hyunsook, Nam & Choi, 2010) seen in literature and comparable to the error of 2 mm reported by Koepke et al. (2017).

The limitation of this method is the requirement for the mesh to be aligned to the *x*, *y*, or *z* axis. If the mesh is not aligned to the mentioned axes, a different method is required. This method could make use of suitably placed landmarks to create a plane and calculate the perpendicular distance to the crown and posterior calcaneus.

6.4 Waist Circumference Measurements

This section describes the methods used to measure WC and the tests performed to assess the accuracy of the methods. Four methods were developed to measure WC. Three methods are based on pathfinding and the fourth method is an ellipse fitting method. The methods are:

- A* path distance
- XZ plane distance
- Plane projection method

- Ellipse fitting

This section defines WC as the horizontal girth passing through the side waist point (International Organization for Standardization, 2016). The side waist point is the most concave point of the (right) side waist when viewed from the front with the body in a standing position (International Organization for Standardization, 2016). Three landmarks are identified from this definition:

- Waist right - Marked on the subject's right side at the waist level.
- Waist anterior - Marked on the front of the subject at waist level
- Waist posterior - Marked on the back of the subject at waist level

Waist circumference was one of the measurements identified as a health indicator and the ability to measure it is an important part of the system. The allowable error for WC measurements is 12 mm as described in section 2.2.1.

6.4.1 Dataset

Six meshes from the Inkreate dataset were used for testing. The ground truth WC measurements were used to compare.

6.4.2 A* Pathfinding Algorithm

Each of the pathfinding methods rely on the A* algorithm (Hart, Nilsson & Raphael, 1968). The algorithm is a method for the determination of a minimum cost path. It operates on a graph G that is defined by a set of $\{n_i\}$ elements or nodes and a set of $\{e_i\}$ directed line segments or arcs. The arcs connect the graphs and each arc has an associated cost $\{c_{ab}\}$ that is the cost from n_a to n_b along arc e_{ab}. Figure 6.6 below shows an example graph.

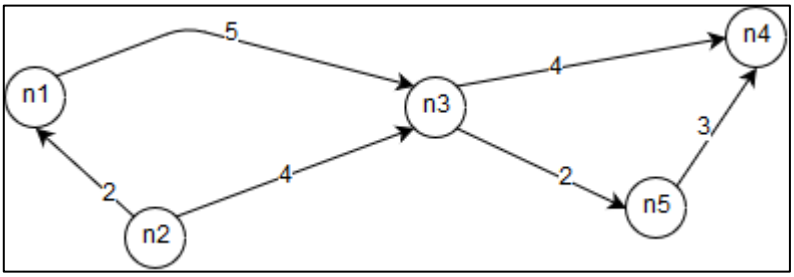

Figure 6.6: Example graph showing the nodes, arcs, and costs.

Assuming a start node sn and a goal node gn, the goal of the algorithm is to evaluate an optimal cost path $f(n)$. The cost path is a sum of two parts:

$$\boldsymbol{f(n) = g(n) + h(n)} \tag{6.2}$$

Where $g(n)$ is the optimal path cost from sn to gn and $h(n)$ is any estimate of the cost of an optimal path between a node n and gn. The algorithm operates as follows:

1. Start at sn and calculate $f(sn)$.
2. Select an open node connected to sn whose f is the smallest with an arbitrary method to resolve ties.
3. Mark the node as closed and terminate the algorithm if the node is gn, otherwise proceed to step 4.
4. Calculate f for each open successor node. Remark any successor closed nodes $n_i$as open if $f(n_i)$ is smaller now than when it was marked closed.
5. Go to step 2.

The calculation of $g(n)$ is based directly on the costs between nodes. The value of $h(n)$ is based on the problem domain. For example, consider determining the shortest path between two cities. The value of $g(n)$ is evaluated using the length of the roads and $h(n)$ can be evaluated as the straight-line distance between the current node (city) and the goal city. Thus, the algorithm penalises transitions that move further away from the goal even if they have the shortest $g(n)$. The algorithm can be applied to the meshes.

Each mesh is composed of vertices that are connected to one another to form faces. Each vertex is a 3D point, located in space, that has direct connections to neighbouring vertices. The algorithm treats meshes as graphs, vertices as nodes, and the connections between vertices as paths. The path cost, $g(n)$, was evaluated as the straight-line distance between the current node and a neighbour. The other cost, $h(n)$, was the straight-line distance between the current node and the end node. The start and ends points are landmarks selected on the mesh. The algorithm outputted a graph containing the optimal path. The length of that path was calculated to determine the distance. The implementation was tested on cubes of known size to determine the lengths of a different number of edges. Landmark were placed on the corners and the distance between them was determined. Additionally, it was tested on spheres to determine the circumference.

i. Results

Table 6.5 below shows the results for the tests performed on cubes and spheres. The distance for the cubes was exact. The distances for the spheres showed a slight error with the largest error being 3.636 mm and the smallest being 0.849 mm.

Table 6.5: A* algorithm shape size test results.

Shape	Ground Truth (mm)	Measured Distance (mm)
Cube	100	100
Cube	1000	1000
Sphere	314.16	317.80
Sphere	3141.59	3140.74

ii. Discussion

This section described the implementation of the A* pathfinding algorithm on meshes. The test results showed that the algorithm performs correctly. The distances for cubes was fully accurate. The distances for spheres were not fully accurate. However, the lack of accuracy can be ascribed to errors in landmark placement. When placing landmarks, it was observed to be easier to place landmarks on the corners of the cubes than on the spheres. The corners of the cubes are distinct and easy to find. The sphere landmarks are much more difficult to place as the sphere is an object without distinct features. Nonetheless, the small errors show that the implementation is suitable.

6.4.3 A Path Distance*

This section describes the basic A* path distance as implemented for human body meshes. The implementation is a custom adaptation created by the author for this research. It was adapted from the implementation available online here[6] (Red Blob Games, 2014).

i. Method

This method relied on two landmarks. These are waist anterior and waist posterior. The length of the optimal path was evaluated by calculating the distances between each node on the optimal path

[6] https://www.redblobgames.com/pathfinding/a-star/implementation.html

outputted by the algorithm and multiplied by two. This method is called A* path distance as it works out the distance using the path determined by the algorithm.

ii. ***Results***

Figure 6.7 below shows the A* path distance difference for each test mesh. The largest difference was 36.96 mm (4.78%) and the smallest was 9.87 mm (1.13%). The average difference was 23.78 mm.

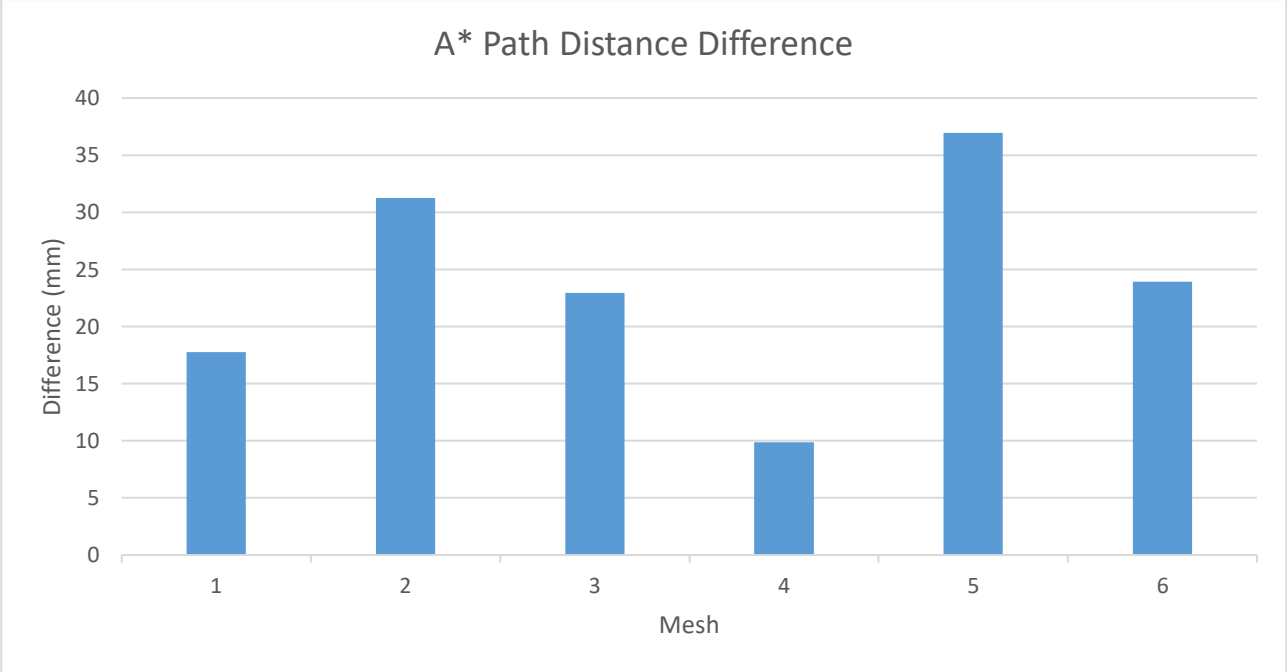

Figure 6.7: A* path distance errors.

iii. ***Discussion***

The algorithm overestimated the WC. This is possibly due to the nature of the graph compared to the definition of WC. Waist circumference is measured in a single horizontal plane whereas the algorithm's path is not restricted to any plane. Figure 6.8 below illustrates the difference between the WC definition and the A* path distance. The straight-line distance is used as an illustration tool and is not representative of the actual WC measurement.

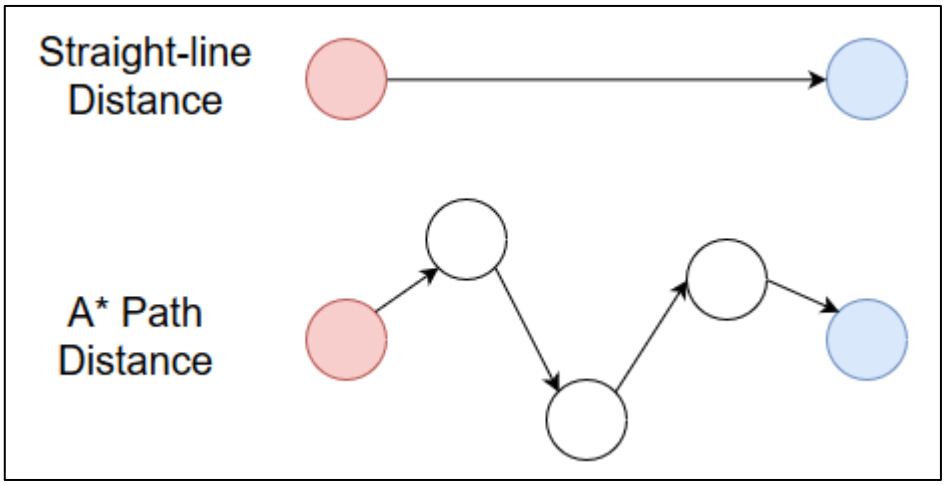

Figure 6.8: Straight-line distance versus A* path distance.

The red circle represents the start (waist anterior) and the blue circle represents the end (waist posterior). In the figure, the straight-line distance is similar to the WC measurement in that the distance

occurs in a single horizontal plane. The A* path distance allows for vertical displacement. This vertical displacement adds to the straight-line distance and partly accounts for the error in the distance. The other pathfinding methods apply different strategies to overcome this issue.

6.4.4 XZ Plane Distance

This method used of the same set of landmarks and the same optimal path as the A* path distance method. However, it differs in the calculation of the length of the path. The custom path length calculation was created by the author for this research.

i. Method

Assuming the meshes are aligned to the *y* axis, the *y* coordinate of each vertex is what solely accounts for vertical displacement. The method then calculated the distance by ignoring the y axis in calculating the path distance. This resulted in the path being projected onto the *XZ* plane. Figure 6.9 below shows the effect of the projection. The red circle represents the start (waist anterior) and the blue circle represents the end (waist posterior).

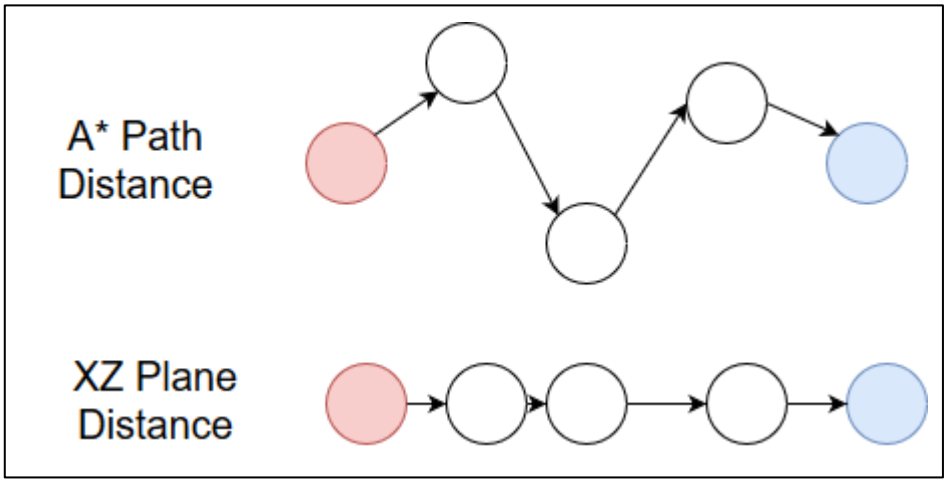

Figure 6.9: A* path distance versus XZ plane distance.

The vertical displacement is eliminated due to the projection. The XZ plane distance is similar to the straight-line distance seen in Figure 6.8. However, it still goes through the same nodes as the A* path distance.

ii. Results

Figure 6.10 below shows the A* XZ plane distance difference for each test mesh. The biggest difference was 44.35 mm (4.15%) and the smallest difference was 24.63 mm (2.92%). The average difference was 32.68 mm.

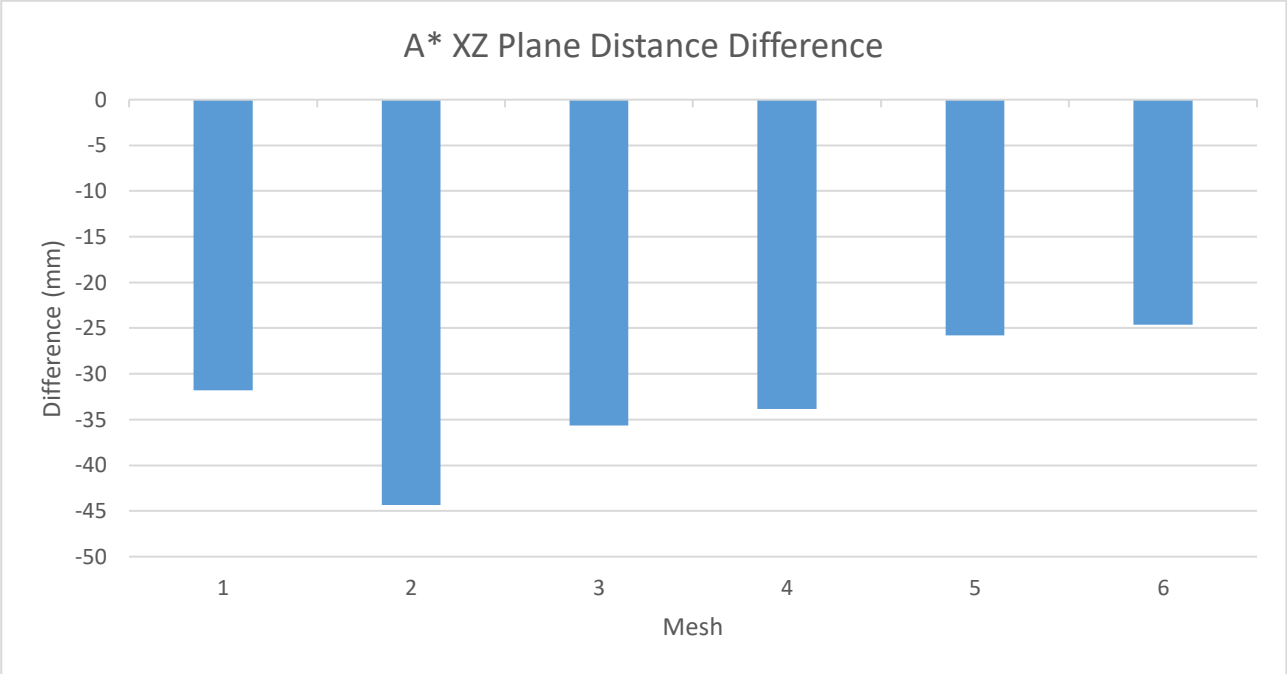

Figure 6.10: A* XZ plane distance errors.

iii. *Discussion*

This method performed worse than the A* path distance method. However, it underestimated the circumference whereas the A* path distance method overestimated the circumference. The method is limited by its reliance on the mesh being aligned to an axis. If aligned, the method can be applied with the elimination of the *x*, *y*, or *z* coordinate as required. However, if the mesh is not aligned, this method cannot be used.

6.4.5 *Plane Projection Distance*

This method used the waist anterior, posterior, and right landmarks as described above. It uses a method to project a point onto a plane (Weisstein, 2002) that was implemented by the author. Distances were then measured in that plane.

i. *Method*

The method calculated two optimal paths. The first between the anterior landmark and the right landmark and the second between the right landmark and the posterior landmark. Two separate distances were then calculated. These distances were added together and multiplied by two to get the WC. This method is like the XZ plane method in that it projects the path onto a plane. However, it created its own plane using the three landmarks. This makes the method invariant to the mesh alignment. The three landmarks were used to calculate the normal vector for the plane and calculate the plane equation. Each point was projected onto the plane and the straight-line distance between the points was calculated. Figure 6.11 below shows how the distance was calculated.

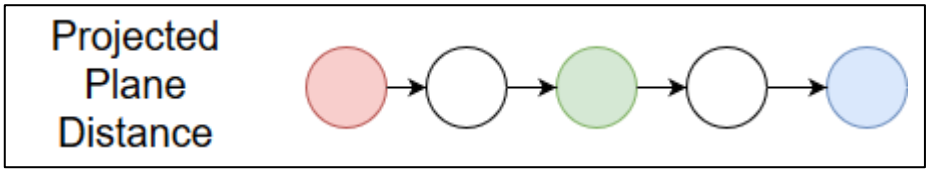

Figure 6.11: Projected plane distance showing the additional landmarks.

The red circle represents the waist anterior, the green waist right, and the blue circle waist posterior. An optimal path between the anterior and right is calculated and an optimal path between the right and posterior was calculated. These paths were projected onto the plane determined by the three points to calculate the distance.

ii. ***Results***

Figure 6.12 below shows the A* projection plane distance difference for each test mesh. The biggest difference was 53.09 mm (4.96%) and the smallest difference was 23.12 mm (2.76%). The average difference was 35.05 mm.

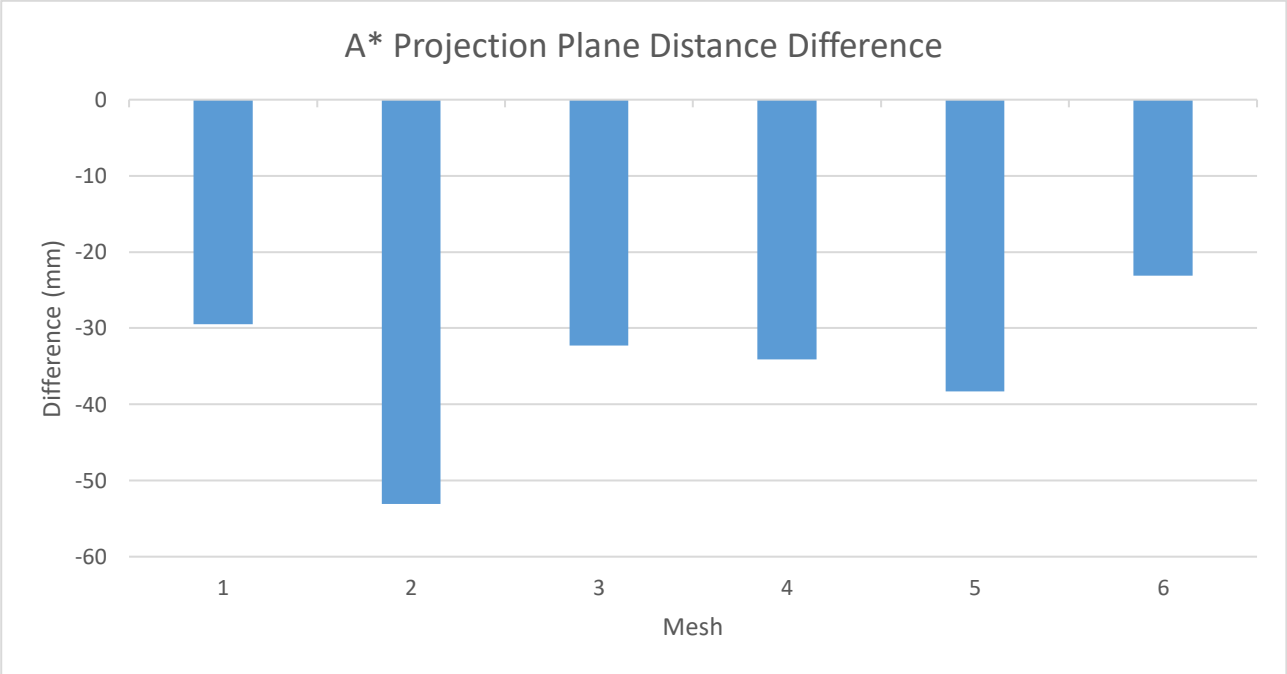

Figure 6.12: A* plane projection distance errors.

iii. ***Discussion***

This method produced the least accurate result out of the pathfinding methods. Similarly, to the *XZ* plane method, it underestimated the WC. The difference between the two methods stems from different methods to determine the plane. The use of a third landmark can result in a plane that is not aligned with the *XZ* plane and as a result, a different distance.

6.4.6 ***Ellipse Fitting***

The final method calculated the circumference by fitting an ellipse. According to Hanavan Jr (1964), the waist can be approximated using an ellipse.

i. ***Method***

This method used the waist anterior, posterior, and right landmarks as described above. The landmarks were used to calculate the length of the major and minor axes. The major axis was determined using the distance between the anterior and posterior landmarks. The minor axis was determined using the distance between the right landmark and the midpoint between the anterior and posterior landmarks. There are a variety of methods to approximate the circumference of an ellipse. The accuracy of each method is dependent on the ratio between the major and minor axis. A few methods have been selected based on those assessed by Almvist & Berndt (1988) and by Abbott (2008). The methods are:

- Cantrell (Sýkora, 2006)
- Holder for low and high eccentricities (Muir, 1902)

- Hudson (Hudson & Lipka, 1917)
- Integral (Abbott, 2008)
- Numerical (Abbott, 2008)
- Ramanujan 1 & 2 (Ramanujan, 1957)

The implementation of each method was tested versus ground truth values produced by Abbott (2008). Each was found to be implemented correctly.

ii. ***Results***

Figure 6.13 below shows the average difference for each of the ellipse fitting methods. Each method underestimated the WC. The largest difference was the Numerical approximation with a difference of -29.94 mm (3.36%). The smallest difference was the Holder approximation for high eccentricities with a difference of 29.62 mm (3.33%).

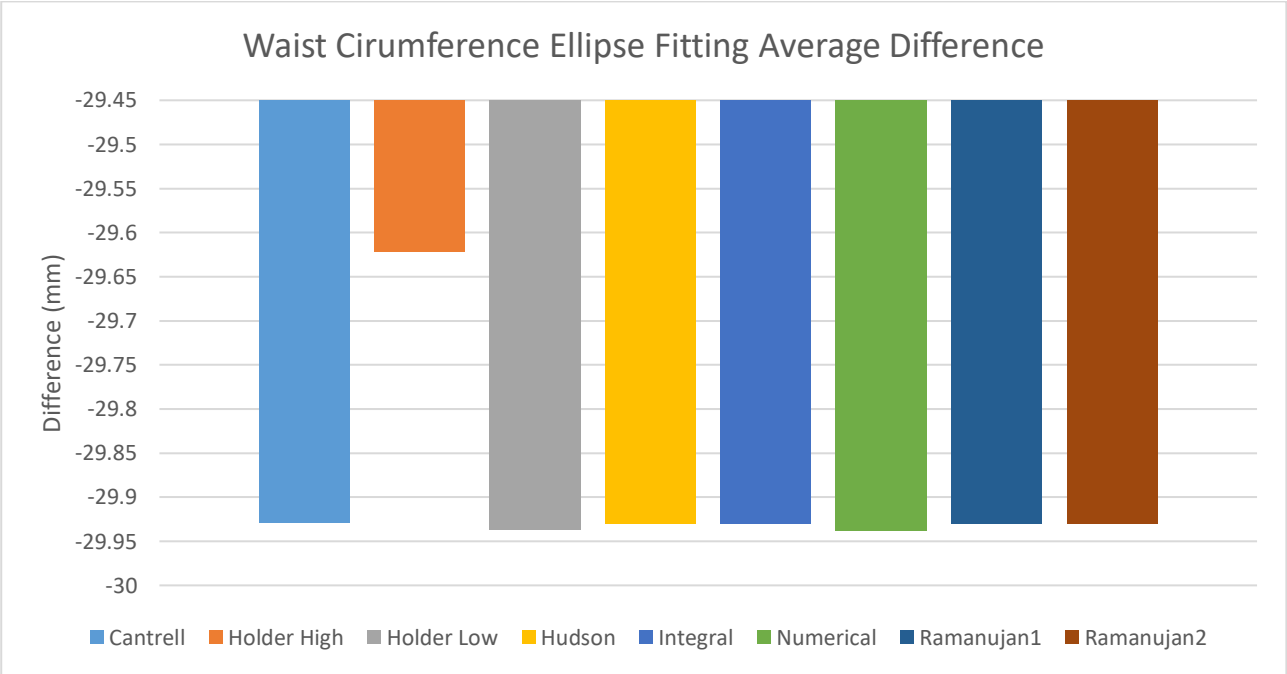

Figure 6.13: Waist circumference ellipse fitting average error for each method.

iii. ***Discussion***

The ellipse fitting methods all underestimated the circumference. The most accurate method is the Holder High approximation. The differences between the methods are in line with previous assessments of ellipse approximation methods that have found small differences (Abbott, 2008, Olver et al., 2010, Sýkora, 2006). The magnitude of these differences is considered negligible for the intended application. The difference of 0.30 mm is far smaller than the allowable error.

6.4.7 ***Discussion: Waist Circumference***

The best performing method for measuring waist circumference was the A* path distance. The best performing ellipse method was the Holder approximation for high eccentricities. However, the difference between it and the rest of the ellipse fitting methods was negligible. The *XZ* plane method and plane projection method both performed worse than the ellipse fitting method and both underestimated the circumference. The difference between the under- and overestimation is due to the vertical displacement when calculating the length of the optimal path. The A* path distance method had an average absolute error of 23.78 mm. This is unsatisfactory based on the allowable error of 12 mm for WC described by Gordon et al. (2014) and mentioned in section 2.2.1. This is also larger than the errors

of 11.7 mm (Koepke et al., 2017) and 20 mm (Han, Hyunsook, Nam & Choi, 2010) seen in literature. A potential source of error are the landmark positions. As shown in section 5, there are landmark errors with poor reliability displayed in the vertical position of the landmarks.

The implementation of the algorithms is unlikely to be a source of error. The A* algorithm implementation was found to implemented correctly based on its performance as demonstrated in section 6.4.2. Additionally, the A* distance being the largest pathfinding distance hints at the correctness of the plane projection methods. The plane distances were expected to be smaller than the A* distance as they both eliminate vertical displacement. Without vertical displacement, they both measure a distance in a horizontal plane. The small difference between the two methods indicates that they are measuring distance in similar planes. However, these distances do not match the WC. This indicates that the horizontal plane did not match the horizontal plane used to measure WC. The vertical position of the plane is dependent on the landmarks. Thus, any landmark errors will change the position of the plane and lead to circumference errors. The ellipse fitting implementation were found to perform satisfactorily versus ground truth values. The correct implementations of each algorithm further point to the landmarks as the source of error.

Additional assessments of the pathfinding methods are recommended using a ground truth measurement where landmark positions are visually marked. The presence of visual markers in the mesh will make manual landmark placement easier. This can be accomplished through painted targets on the subjects that are used when manually measuring WC. An alternative to manual placement is automatic placement as demonstrated by Xiaohui et al. (2018). They applied random forest regression of geodesic distances to place landmarks and found an average error of 0.62 mm. The landmarks would be considered highly precise and should not contribute to any measurement errors.

6.5 Chapter Summary

This section presented the implementation and testing of the algorithms to measure body volume, height, and waist circumference. The volume measurement method was found to be implemented correctly. However, the discretisation of objects caused a change in volume that affected the results. Nonetheless, the errors for human bodies were small. The height measurement method was found to perform satisfactorily with an error smaller than the allowable error. However, it requires the mesh to be aligned to the *x*, *y*, or *z* axis. The best performing WC was the A* path distance method. However, the error was larger than the allowable error. The pathfinding algorithm was shown to be implemented correctly and is unlikely to be the source of error. Thus, the landmark positions are the likely source of error as their positions are imprecise as shown in section 5.

7. Reconstruction Algorithm

The central component of the system is the 2D to 3D reconstruction algorithm. The ability to reproduce a 3D representation allows for the measurement algorithms to extract useful information for body composition assessment. The accuracy of the 3D reconstruction is vital as it affects the accuracy of the measurements. This chapter begins with descriptions of the data used for development and testing. This is followed by a detailed description of the reconstruction methodology, its implementation and the results.

7.1 Dataset

The testing of the reconstruction used two sets of data. The first is a subset of the SPRING data which was used to create the Gaussian process morphable models (GPMMs). The meshes selected were part of the GPMM development process. These data represent an ideal scenario where the training and test data are similar due to the same pose and having been captured by the same imaging machine. The second is the MPI-Faust dataset. The second set of data represents a generalised scenario of how the 3D from 2D would work in a real application; i.e. where the model training data is dissimilar to the test data.

7.2 Reconstruction Pipeline

This section describes the reconstruction pipeline. The reconstruction process used GP regression and required a reference and a target. The reference was the GPMM and the target were derived from the image landmarks.

7.2.1 Image Landmarks

Reconstruction required landmarks to be manually placed on the images. A subset of the landmarks was placed on the anteroposterior (AP) image and a subset on the lateral (LAT) image. The list of landmarks and images the landmarks appear in are in section 5.1. Landmarks were created and saved using a modified version of the Landmark Clicker software[7] (Graphics and Vision Research Group University of Basel, 2019). The software helps a user to manually specify landmarks on 2D images. Landmarks are described by a landmark ID and landmark coordinates in pixels.

7.2.2 Landmark Processing

The program took the landmarks, images, and the real height as inputs. The real height and images are necessary as the landmarks need to be appropriately scaled from pixels to mm. Scaling was performed as follows:

- Calculate the pixel height distance between the crown and a metatarsal.
- Calculate a scaling factor to convert the pixel height distance into the real height.
- Scale the coordinates of each landmark by the scaling factor.

Following scaling, 3D points were constructed using the scaled 2D landmarks. The third unknown coordinate was set to 0. For front images the third coordinate was the *z* coordinate and for LAT images it was the *x* coordinate.

7.2.3 3D Reconstruction

The 3D reconstruction performed in this research is a two-step process that reconstructs first using the AP image landmarks and produces a posterior. That posterior was then used to reconstruct using the LAT landmarks. The process began with the alignment of the 3D anteroposterior landmarks to the GPMM. Gaussian process regression was performed using the GPMM, the 3D anteroposterior landmarks

[7] https://github.com/unibas-gravis/landmarks-clicker

as the target, and the model landmarks as the reference. The output was a posterior model referred to as the AP posterior. The LAT 3D landmarks were then aligned to the AP posterior model. Regression was performed using the posterior model, the LAT 3D landmarks, and the AP posterior model. The output was another posterior referred to as the LAT posterior. The mean of the LAT posterior was returned as the best reconstruction as it is the most probable from the posterior distribution. The landmarks were rigidly aligned to their relevant GPMM using Generalized Procrustes analysis (GPA). Rigid alignment was performed to remove translation and rotation differences that affect regression. The Gaussian noise was set low for the known coordinates and set very high for the unknown coordinate during regression. The above description is a general overview of the process. Different methods that follow this general process, but differ in their approaches to regression or evaluation, were developed. They are described in the next subsections

i. Shape model with arms

This method used the shape model that was produced during the GPMM development. All the landmarks were present in this method and reconstruction began with the AP image.

ii. Modified shape model with arms

This method used the shape model with artificially induced shape variation. The introduction of artificial variation aimed to increase the range of shapes expressed by the model. The variation was changed through modifications to the kernel. The Gaussian kernel is defined as follows:

$$\boldsymbol{k}(\boldsymbol{x},\boldsymbol{y}) = \mathbf{exp}\left(\frac{-\|\boldsymbol{x}-\boldsymbol{y}\|^{\mathbf{2}}}{\boldsymbol{\sigma}^{\mathbf{2}}}\right) \tag{7.1}$$

Variation can be changed by altering σ. The value of σ acts inversely on the frequency of the leading eigenfunctions. An increase in σ results in a decrease in the variation contained in the leading eigenfunctions, and conversely, an increasing in the trailing eigenfunctions. The effect is the smoothing of the sample functions (Lüthi et al., 2016). Changing the distribution associated with the eigenvalues and eigenfunctions also alters variation. The distribution is defined as follows:

$$\boldsymbol{p}(\boldsymbol{x}) \sim \boldsymbol{N}\left(\mathbf{0}, \boldsymbol{s}^{\mathbf{2}}\right) \tag{7.2}$$

Changing the variance s^2 affects the decay of the eigenvalues. Variance changes suitable for reconstruction are implemented by modifying σ and s^2**.**

iii. Modified shape model with arms removed for assessment

This method used the modified shape model with the arms removed when testing the reconstruction accuracy. The arms were removed through manual identification of the point IDs corresponding to those of the arms. The points were removed from each mesh using methods within the Scalismo library. The removal of arms was due to pose differences within the data used for development and testing. There are pose differences with the arms that are not accounted for during development. Figure 7.1 below shows three overlaid meshes from the development dataset. Each mesh is in a different colour. The pose differences can be seen on the left of Figure 7.1 with differences in the position of the arms relative to one another. Pose differences in the coronal plane are also visible with the asymmetric pose differences.

iv. Marginalised modified model without arms

This method marginalised the arms of the model. The pose issues seen in Figure 7.1 below and described above also apply. Marginalisation enables the disregarding of selected information from the statistics (Graphics and Vision Research Group University of Basel, 2017). Given jointly distributed random variables *X* and *Y,* they can be modelled using a joint multivariate distribution:

$$\boldsymbol{P(X,Y) = N\left(\begin{pmatrix}\mu_X\\ \mu_Y\end{pmatrix}, \begin{pmatrix}\Sigma_{XX} & \Sigma_{XY}\\ \Sigma_{YX} & \Sigma_{YY}\end{pmatrix}\right)} \quad (7.3)$$

A marginal distribution $p(X)$ is given by:

$$\boldsymbol{p(X) = N(\mu_X, \Sigma_{XX})} \quad (7.4)$$

As applied in this instance, the effect of marginalisation was to define a GPMM in which the arms, and the associated variance, were not present; while retaining the learned statistics in the remaining region.

v. Normal shape model with other modifications

In addition to modifying the shape model, other changes were made to the pipeline. Each change made use of the shape model. The changes either reconstructed using the side image first then the AP image or made use of a different number of landmarks. These methods are:

- Side image then AP image
- Minimal number of landmarks
- Intermediate number of landmarks

The maximum landmark version used all 22 landmarks in Table 5.1 above. The intermediate version used the following 13 landmarks:

- crown
- acromion.rt
- acromion.lt
- waist.anterior
- waist.rt
- waist.lt
- waist.posterior
- trochanterion.rt
- trochanterion.lt
- radial-styloid.rt
- radial-styloid.lt
- metatarsal-phalangeal.v.rt
- metatarsal-phalangeal.v.lt

The minimum version used the following nine landmarks:

- crown
- waist.anterior
- waist.rt
- waist.lt
- waist.posterior
- radial-styloid.rt
- radial-styloid.lt
- metatarsal-phalangeal.v.rt
- metatarsal-phalangeal.v.lt

The landmarks used in the maximum version were selected based on those use in traditional and 3D anthropometry as required for the measurements being performed. The list was refined to consider landmarks on the silhouette in the AP and LAT views. The intermediate and minimum landmarks were selected from that list with a reduction in the number of landmarks on the silhouette in the AP and LAT views. Figure 7.2 below shows the differences between the minimum, intermediate, and maximum number of landmarks. Reconstruction with the maximum landmarks is in green, the intermediate in

pink, and the minimum in red. The maximum number of landmarks was used for all the other reconstruction methods.

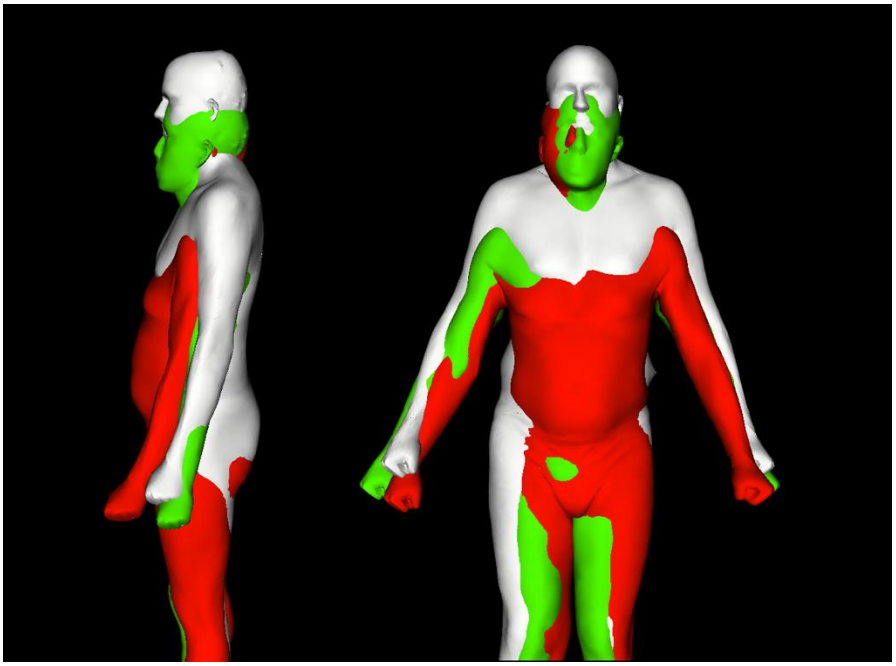

Figure 7.1: Three training meshes overlaid to show the differences in arm pose.

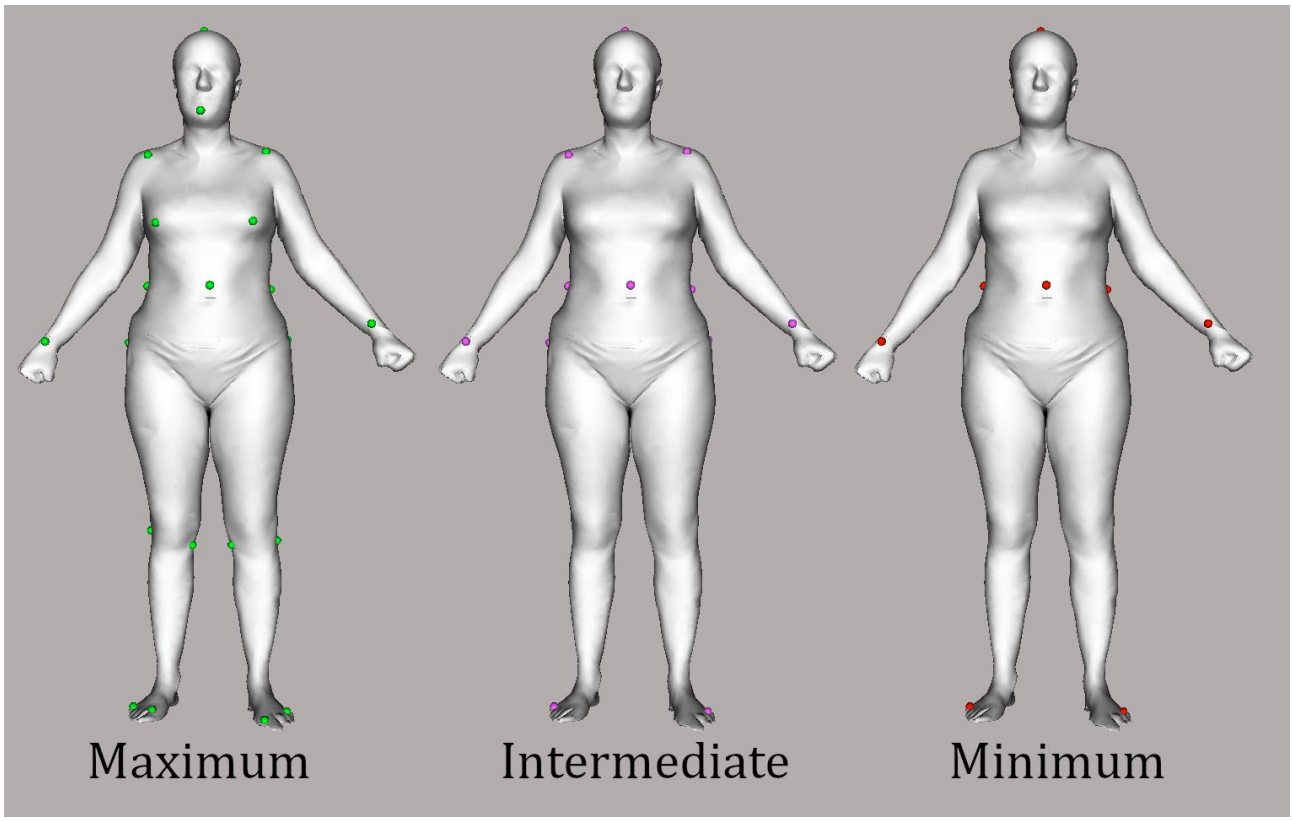

Figure 7.2: Body model landmarks showing the different landmark sets.

In addition to the three landmark sets, a separate test was conducted to assess the ability to reconstruct a mesh with the correct height when given the landmarks used to measure height in scaling. These landmarks were crown and the fifth metatarsal on the left foot. These tests were performed using the SPRING data.

7.2.4 *Summary*

Figure 7.3 below summarises the reconstruction pipeline. Input images are opened in the Landmark Clicker software and an image landmark set is produced as output. The landmark set contains AP and LAT landmarks. The figure only shows the AP image, but the LAT image also goes through the Landmark Clicker. The landmark set is sent to landmark processing where pixel height calculation, scaling factor calculation, landmark scaling, and 3D landmark creation are determined. The output is a 3D landmark set that is input to 3D reconstruction. The 3D reconstruction has two possible paths. The first path begins with the AP landmarks and the second with the LAT landmarks. On the first path, the anteroposterior 3D landmark set go through GP regression to produce an AP posterior. This AP posterior is used with the side 3D landmarks in GP regression. The output is a LAT posterior whose mean is taken as the best reconstruction. The second path is the same except the AP and LAT landmarks are exchanged and the relevant outputs change as well.

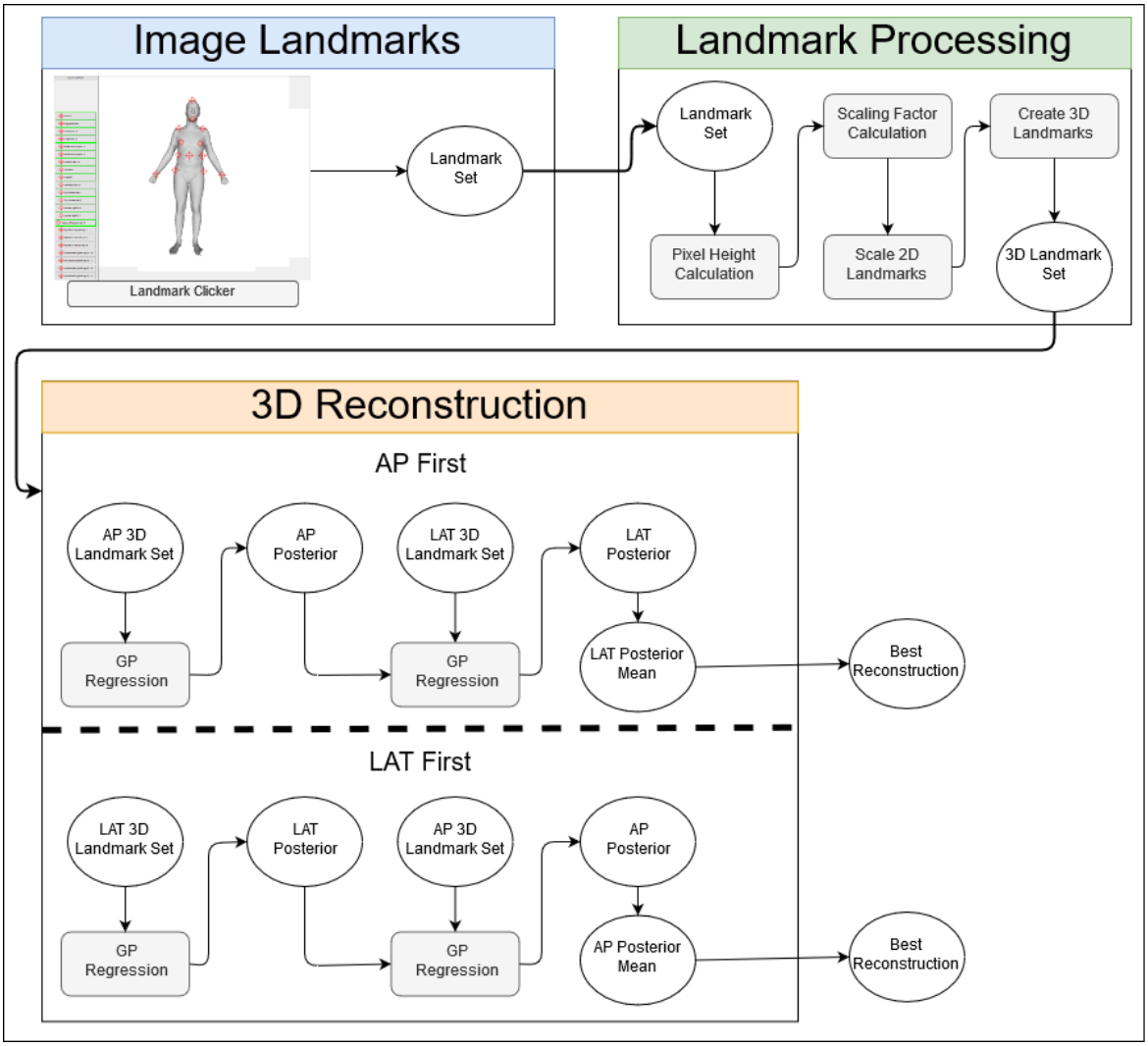

Figure 7.3: Reconstruction pipeline showing the processes of each stage. The two 3D reconstruction approaches are in labelled as AP first and LAT first.

7.3 Testing

The SPRING test data and the MPI-FAUST test data each contain 5 female and 5 male meshes. The following metrics were evaluated to test the accuracy of the reconstructions:

- Surface-to-surface distance per vertex
- Modified Hausdorff surface-to-surface distance (Dubuisson & Jain, 1994)

- Height
- Waist circumference (WC) [A* path distance]
- Body volume (BV)

The surface distance metrics were evaluated to assess the overall accuracy of the reconstruction. The surface-to-surface distance per vertex evaluates the average distance from vertices on one mesh to the surface on the other mesh. The modified Hausdorff distance performs a similar operation but takes the maximum of the average when measuring both was. It is defined as:

$$\max\big(\boldsymbol{dis}(\boldsymbol{A},\boldsymbol{B}),\boldsymbol{dis}(\boldsymbol{B},\boldsymbol{A})\big) \tag{7.5}$$

$$\boldsymbol{dis}(\boldsymbol{A},\boldsymbol{B}) = \frac{\mathbf{1}}{\boldsymbol{N_a}}\sum_{\boldsymbol{a}\epsilon\boldsymbol{A}} \boldsymbol{d}(\boldsymbol{a},\boldsymbol{B})$$

Where meshes are A and B, a is a vertex on a mesh, and $d(a,B)$ evaluates the distance from vertex a to a given mesh. This distance was used for completeness as surface-to-surface per vertex is not necessarily symmetrical. The final three metrics were evaluated to assess the suitability for the intended applications. Waist circumference was measured using the A* path distance as it was the best performing method of those evaluated in section 6.4. The allowable error for height is 6 mm and for WC it is 12 mm as described in section 2.2.1.

7.4 SPRING Results

This section describes the results from the SPRING test data. These meshes are part of the GPMM. These results represent an ideal scenario for the reconstruction; that is, where the test data and the training data are very similar in how they are acquired, post processed, and the acquisition pose is standardised.

7.4.1 Female Model

i. Qualitative Assessment

Figure 7.4 below shows the mean mesh, original mesh, reconstructed mesh, and an overlap of the original and reconstructed meshes for a given mesh from the female test data. The meshes shown are those from the shape model method. The reconstructed meshes are visually consistent with the shape of the human body. There are slight pose differences between the original and the reconstruction.

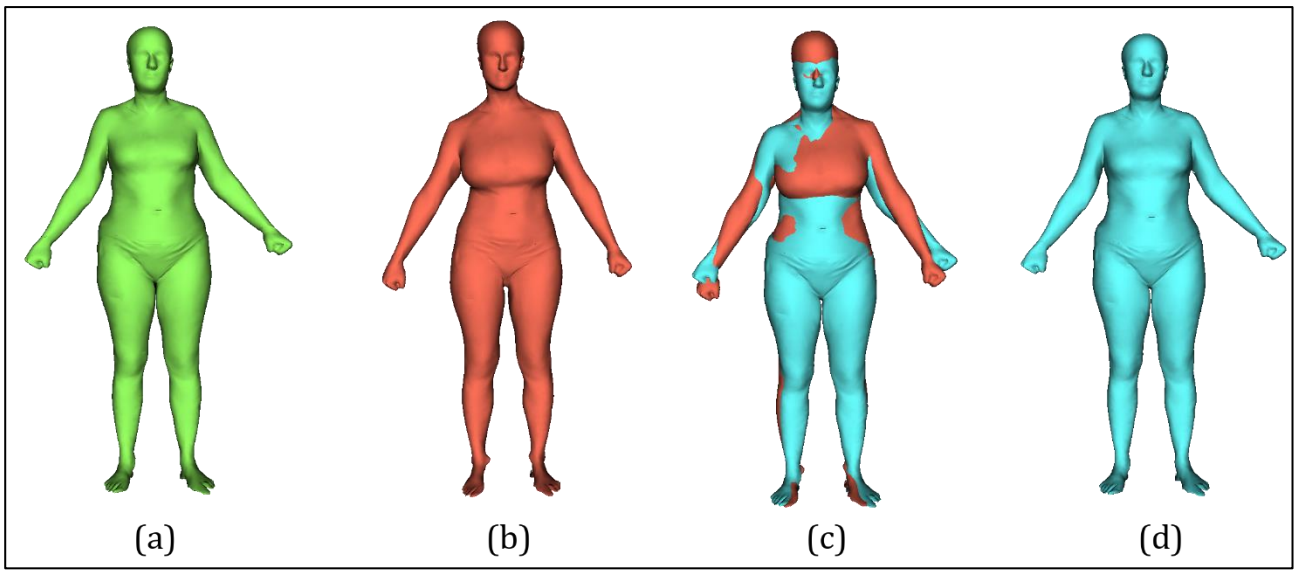

Figure 7.4: The model mean mesh (a), original mesh (b), the reconstructed mesh (d), and an overlap of the original and reconstruction (c) are shown for a SPRING male test mesh using the shape model method.

ii. Surface Distances

Figure 7.5 below shows the surface-to-surface distances. The inverse fitting approach had the largest distances with 19.28 mm for the surface-to-surface distance per vertex and 23.40 mm for the modified Hausdorff distance. The modified model without arms had the smallest distances with 14.27 mm for the surface-to-surface distance per vertex and 15.64 mm for the modified Hausdorff distance. Of the models with arms, the intermediate landmark model had the smallest distances with 15.47 mm for the surface-to-surface distance per vertex and 16.82 mm for the modified Hausdorff distance.

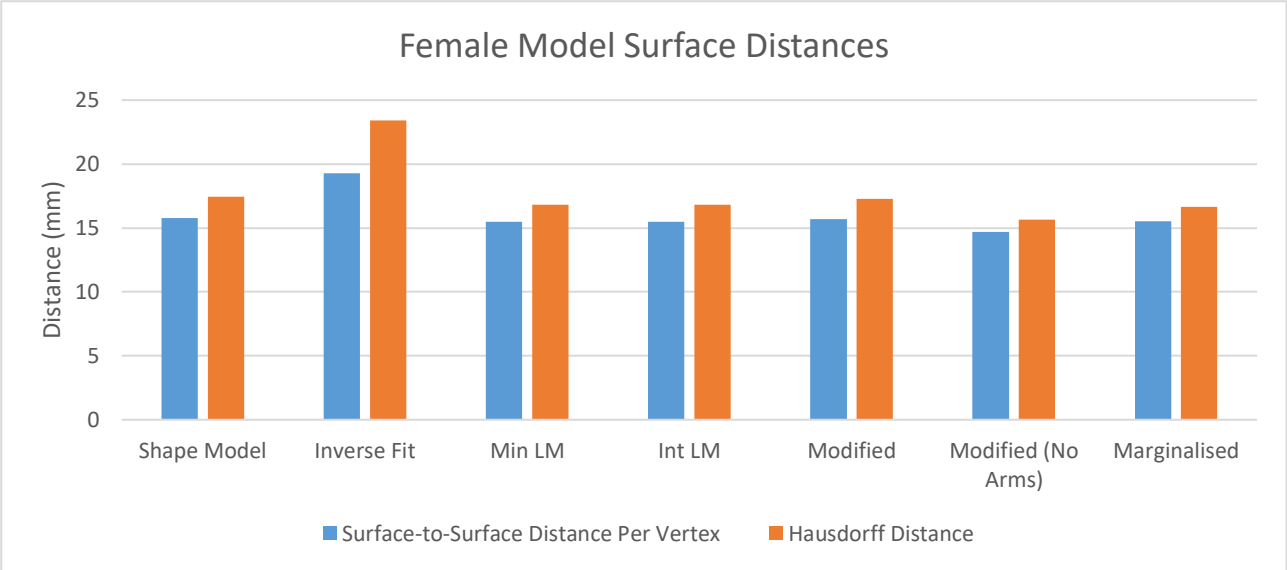

Figure 7.5: Female model surface-to-surface distances for SPRING test data.

Figure 7.6 and Figure 7.7 below show heatmaps for the best and worst test results from the shape model for SPRING test data. The heatmap shows the surface distance for each vertex with colour correlating to the scale displayed. For the best result, the errors do not exceed 100 mm and are most prominent on the hands, upper back, and head. For the worst result, the errors do not exceed 100 mm and are most prominent on the arms, anterior trunk, and anterior upper leg.

Figure 7.6: Female model best reconstruction heatmap for SPRING test data.

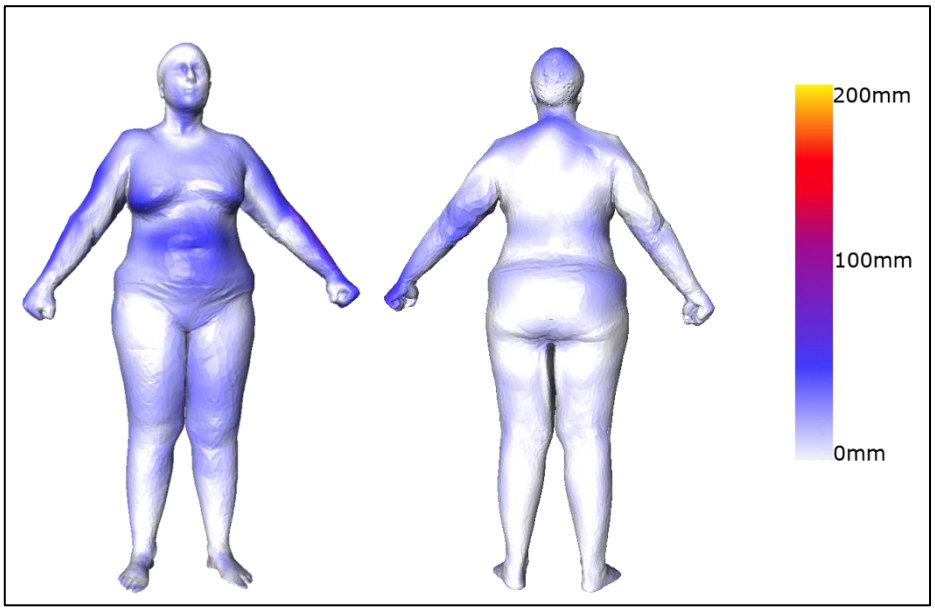

Figure 7.7: Female model worst reconstruction heatmap for SPRING test data.

iii. ***Body Measurements***

Figure 7.8 below shows the MD and MAD for height and WC. For each approach, the height MD and MAD were the same indicating the error was always an overestimation of height. For WC, the MD was small and, in some instances, negative. The MAD indicates errors due to under- and overestimation with a slight skew towards overestimation for the positive MDs and underestimation for the negative MDs. The best performing approach for height was the intermediate landmark model with a MAD of 37.57 mm. The best for WC was the inverse fit with a MAD of 81.04 mm. The worst for height was the inverse fit and the worst for WC was the intermediate landmark model. Additionally, the reconstruction using only the height landmarks produced a MAD of 37.60 mm.

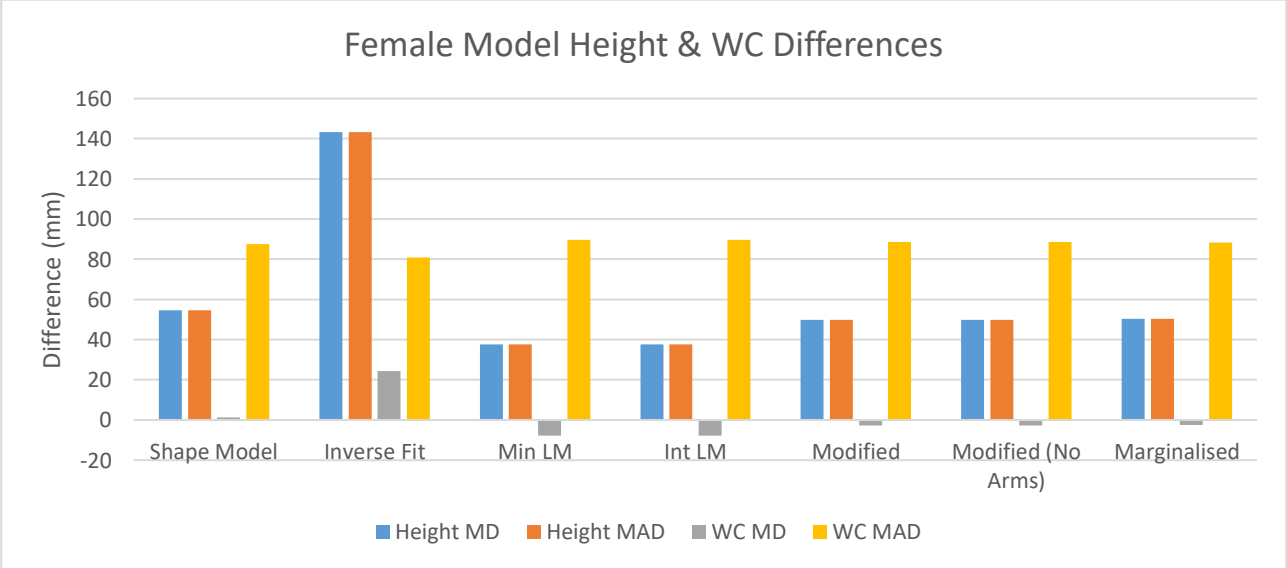

Figure 7.8: Female model height and WC differences for SPRING test data.

Figure 7.9 below shows the volume MD and MAD values. The MAD values indicate an error due to under- and overestimation with a skew towards underestimation due to the negative MD. The best performing approach was the marginalised model with a MAD of 9.93 litres (l). The worst performing approach was the inverse fit.

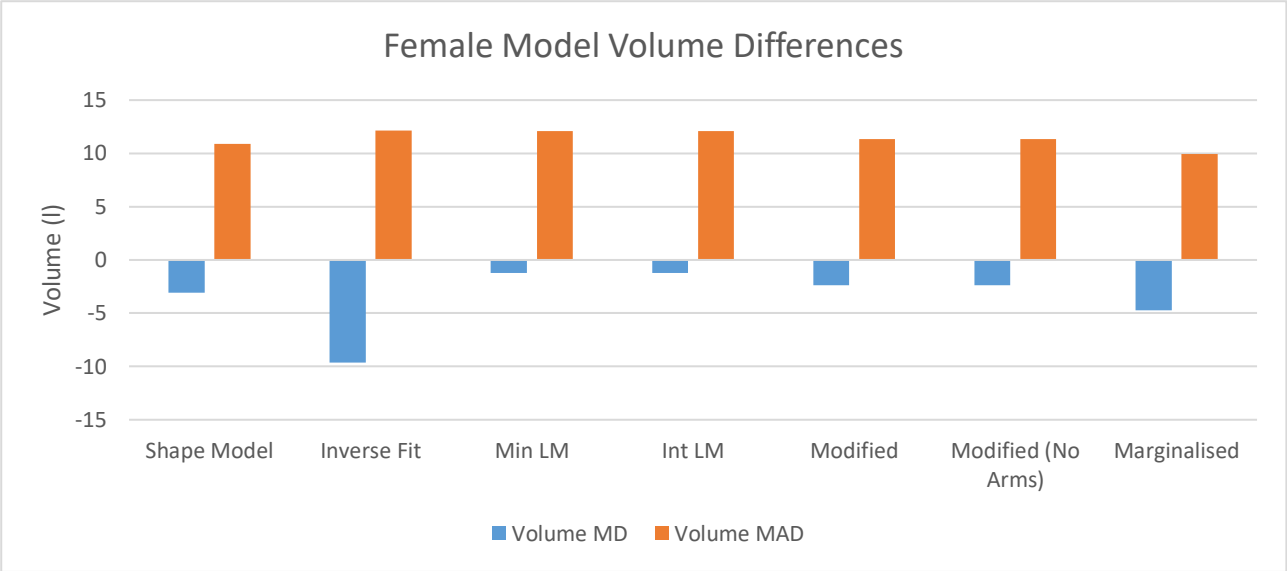

Figure 7.9: Female model volume differences for SPRING test data.

7.4.2 Male Model

i. Qualitative Assessment

Figure 7.10 below shows the mean mesh original mesh, reconstructed mesh, and an overlap of the original and reconstructed meshes for a given mesh from the male test data. The meshes shown are those from the shape model method. The reconstructed meshes are visually consistent with the shape of the human body.

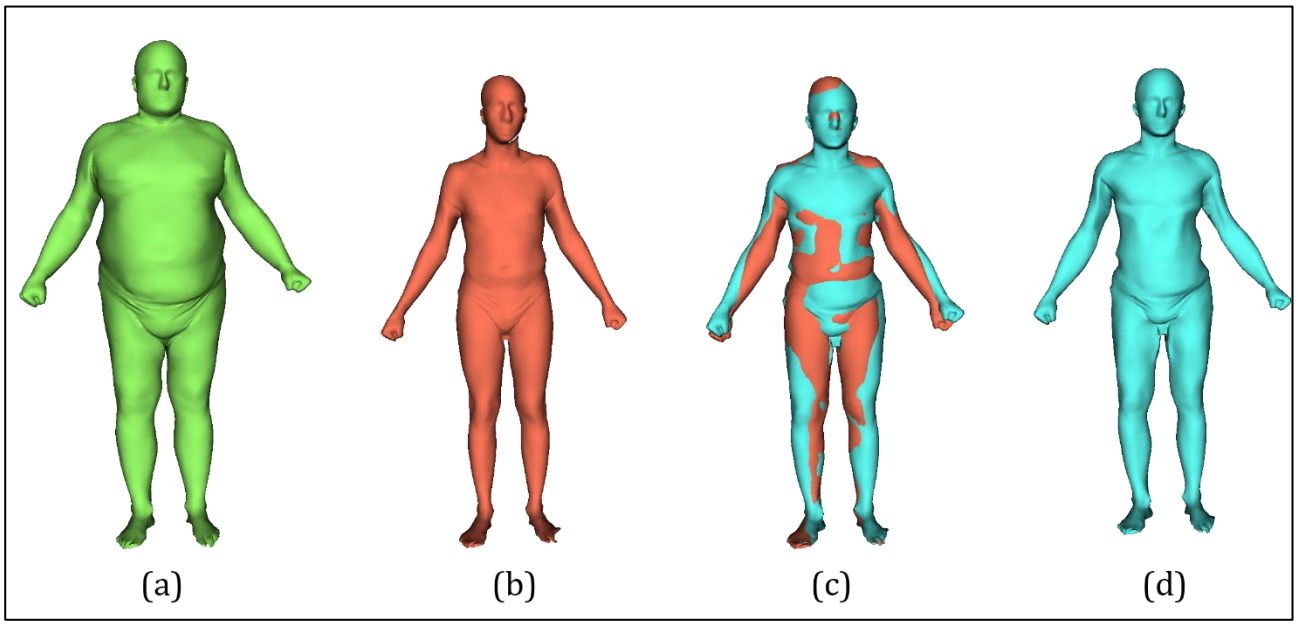

Figure 7.10: The model mean mesh (a), original mesh (b), the reconstructed mesh (d), and an overlap of the original and reconstruction (c) are shown for a SPRING male test mesh using the shape model method.

ii. Surface Distances

Figure 7.11 below shows the surface-to-surface distances. The inverse fitting approach had the largest distances with 19.47 mm for the surface-to-surface distance per vertex and 26.87 mm for the modified Hausdorff distance. The modified model without arms had the smallest distances with 12.88 mm for the surface-to-surface distance per vertex and 12.93 mm for the modified Hausdorff distance. Of the models

with arms, the modified model had the smallest distances with 14.16 mm for the surface-to-surface distance per vertex and 14.22 mm for the modified Hausdorff distance.

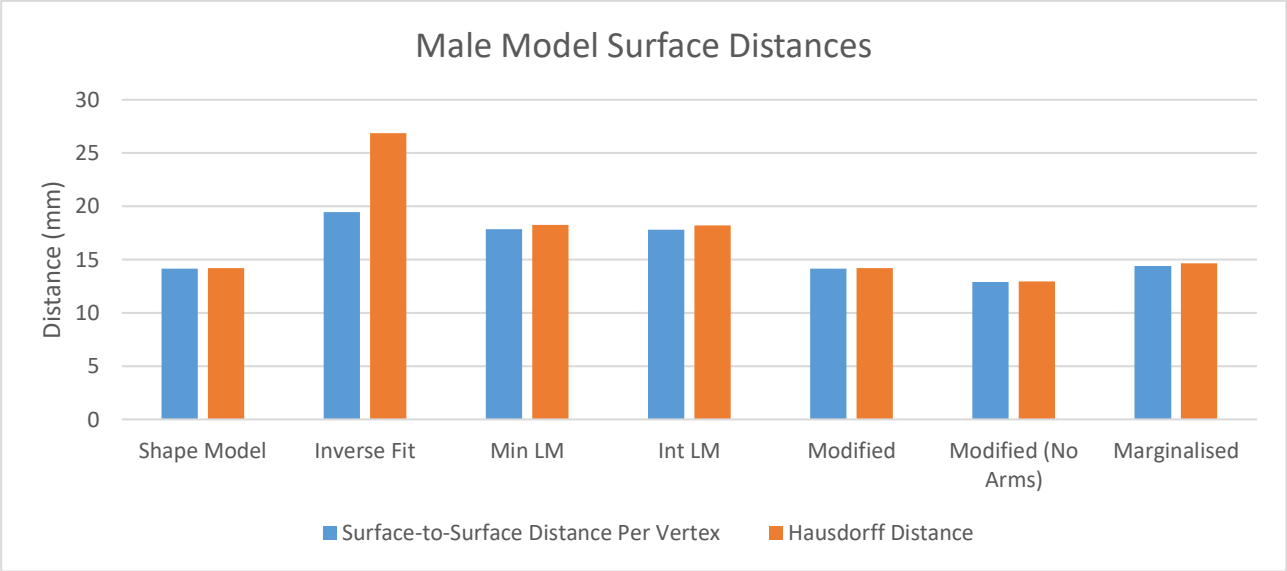

Figure 7.11: Male model surface-to-surface distances for SPRING test data.

Figure 7.12 and Figure 7.13 below show heatmaps for the best and worst test results from the shape model for SPRING test data. The heatmap shows the surface distance for each vertex with colour correlating to the scale displayed. For the best and worst results, some errors exceed 100 mm, but most are below 100 mm, and the errors are most prominent on the posterior. The worst result has error on the anterior with the most prominent being in the arms.

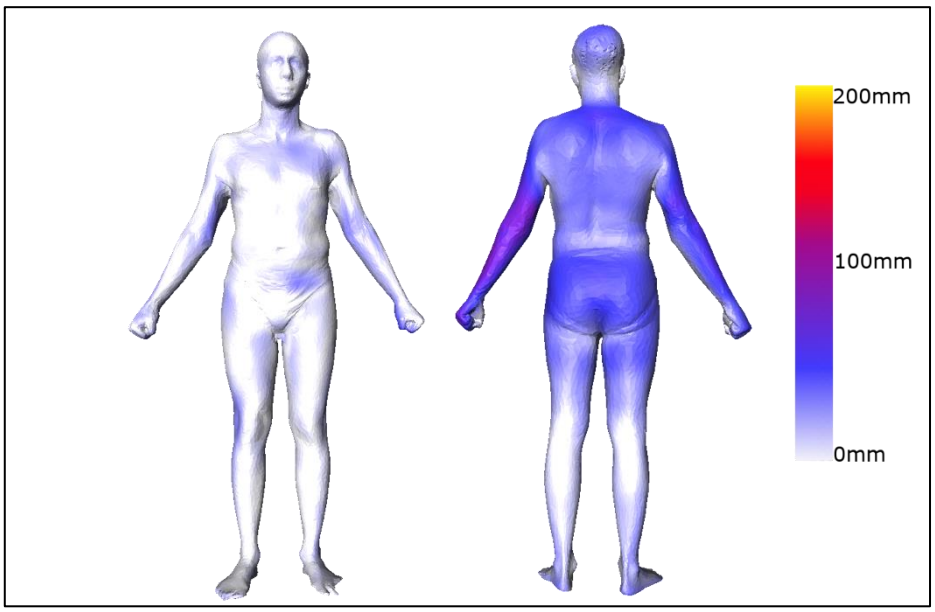

Figure 7.12: Male model best reconstruction heatmap for SPRING test data.

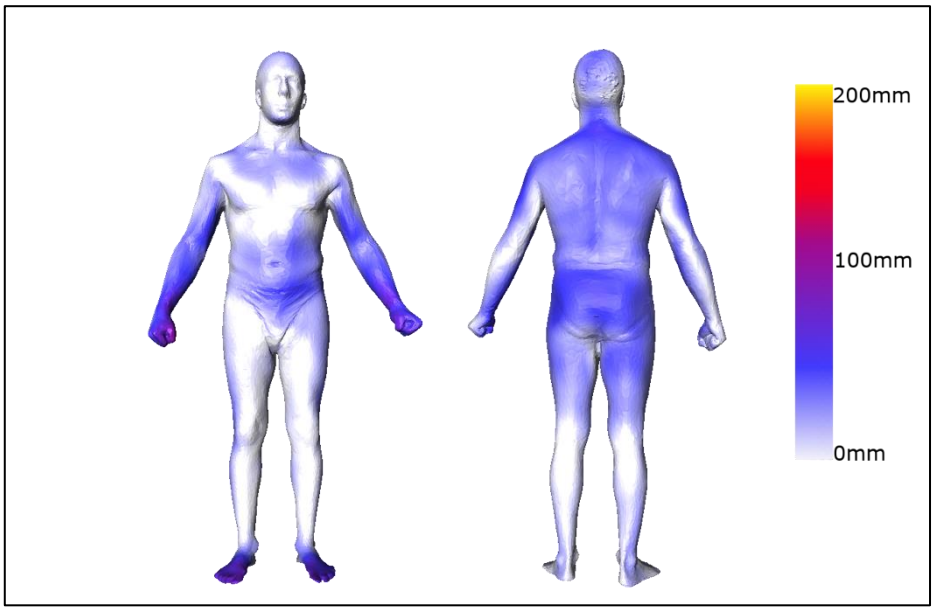

Figure 7.13: Male model worst reconstruction heatmap for SPRING test data.

iii. Body Measurements

Figure 7.14 below shows the MD and MAD for height and WC. For most approaches, the height MD was negative, and the MAD was larger indicating errors due to underestimation. For WC, the MD was generally negative, and the MAD larger indicating errors due to underestimation. The best performing approaches for height were the shape model and modified models with a MAD of 44.12 mm. The best for WC was the intermediate landmark model with a MAD of 95.94 mm. The worst for height and WC was the inverse fit. Additionally, the reconstruction using only the height landmarks produced a MAD of 99.76 mm.

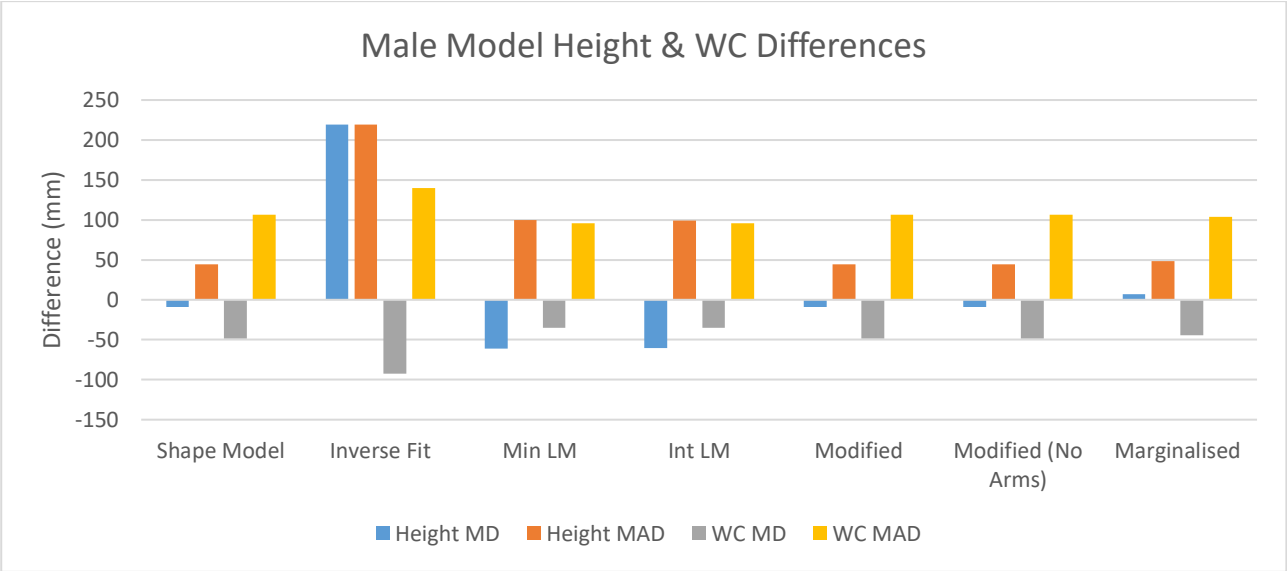

Figure 7.14: Male model height and WC differences for SPRING test data

Figure 7.15 below shows the volume MD and MAD values. The MAD values indicate an error due to under- and overestimation with a skew towards overestimation due to the mostly positive MDs. The best performing approach was the marginalised model with a MAD of 5.59 l. The worst performing approach was the inverse fit.

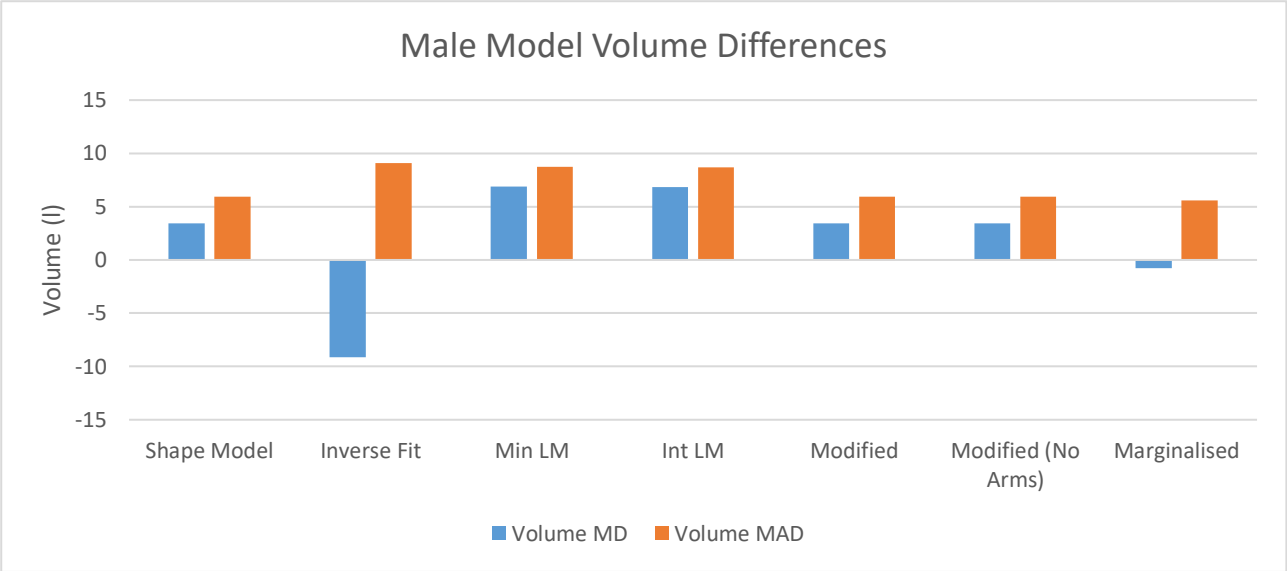

Figure 7.15: Male model volume differences for SPRING test data.

7.5 MPI-Faust Results

This section describes the results from the MPI-Faust test data. The meshes are not included in the GPMMs. Additionally, they feature pose differences in the form of open hand versus closed fist. These results represent a generalised scenario for the reconstruction algorithm.

7.5.1 Female Model

This section presents the results of the female model reconstruction. In addition to the measurements, the human-like quality of the reconstructions was visually inspected.

i. Qualitative Assessment

Figure 7.16 below shows the mean mesh, original mesh, reconstructed mesh, and an overlap of the original and reconstructed meshes for a given mesh from the female test data. The meshes shown are those from the shape model method. The reconstructed meshes are visually consistent with the shape of the human body. The pose differences in the arms between the original and reconstruction are also clear in the figure.

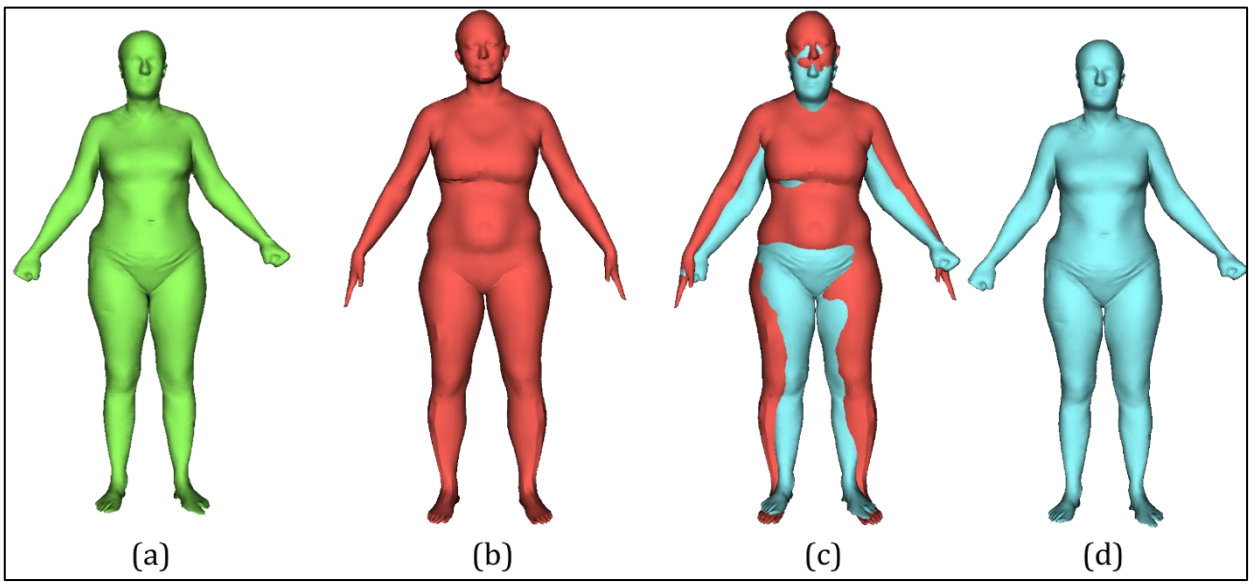

Figure 7.16: The model mean mesh (a), original mesh (b), the reconstructed mesh (d), and an overlap of the original and reconstruction (c) are shown for a MPI-FAUST female test mesh using the shape model method.

ii. Surface Distances

Figure 7.17 below shows the surface-to-surface distances. The inverse fitting approach had the largest distances with 23.93 mm for the surface-to-surface distance per vertex and 40.86 mm for the modified Hausdorff distance. The modified model without arms had the smallest distances with 18.26 mm for the surface-to-surface distance per vertex and 20.59 mm for the modified Hausdorff distance. Of the models with arms, the intermediate landmark model had the smallest distances with 19.44 mm for the surface-to-surface distance per vertex and 31.02 mm for the modified Hausdorff distance.

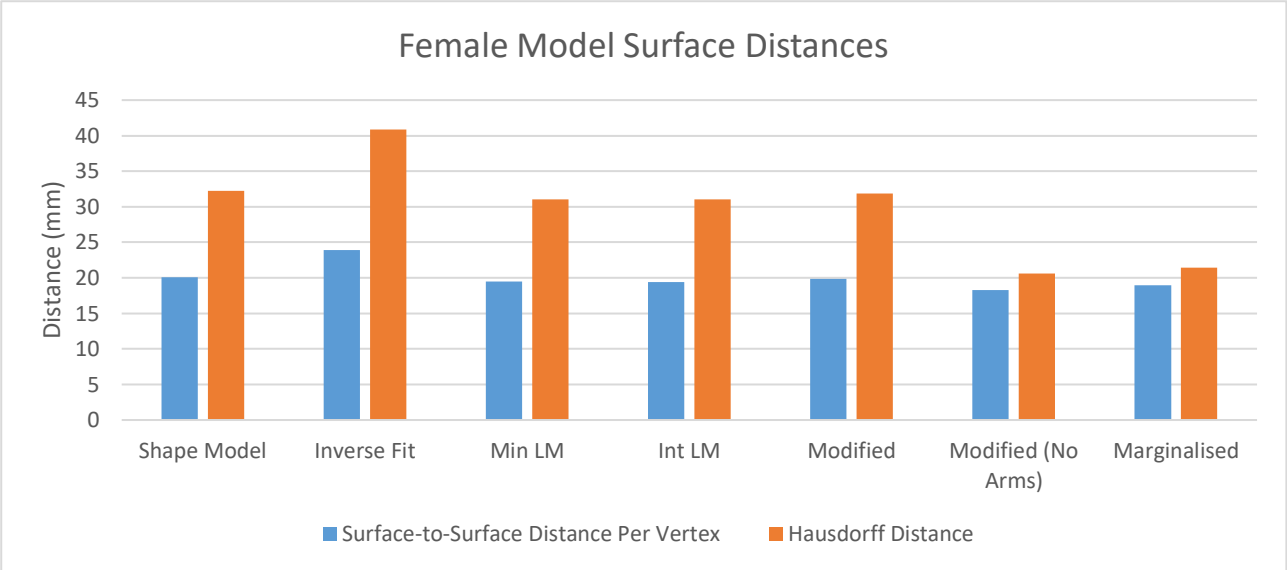

Figure 7.17: Female model surface-to-surface distances for MPI-Faust test data.

Figure 7.18 and Figure 7.19 below show heatmaps for the best and worst test results from the shape model for MPI-Faust test data. The heatmap shows the surface distance for each vertex with colour correlating to the scale displayed. For the best result, the errors do not exceed 100 mm and are prominently present on the head, chest, and lateral portion of the limbs. For the worst result, the errors exceed 100 mm with prominent errors in the arms and lateral portion of the legs. There are prominent errors on the anterior trunk in contrast to the best result.

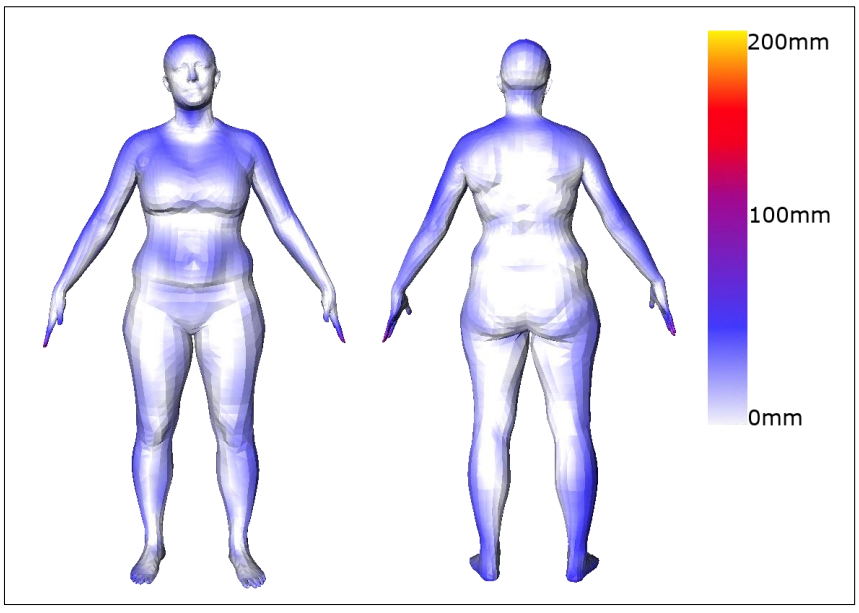

Figure 7.18: Female model best reconstruction heatmap for MPI-FAUST test data.

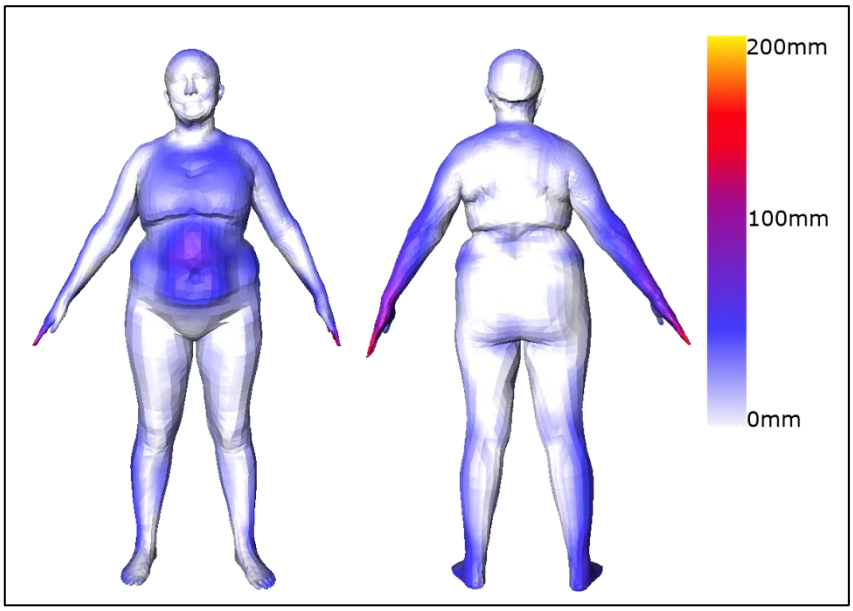

Figure 7.19: Female model worst reconstruction heatmap for MPI-Faust test data.

iii. Body Measurements

Figure 7.20 below shows the MD and MAD for height and WC. For each approach, the height MD and MAD were the same indicating the error was always an overestimation of height. For WC, the MD was small and the MAD large indicating large errors due to under- and overestimation with a slight skew towards overestimation. The best performing approach was the intermediate landmark model with a height MAD of 112.60 mm and a waist circumference MAD of 15.83 mm. The worst performing approach was the inverse fit approach.

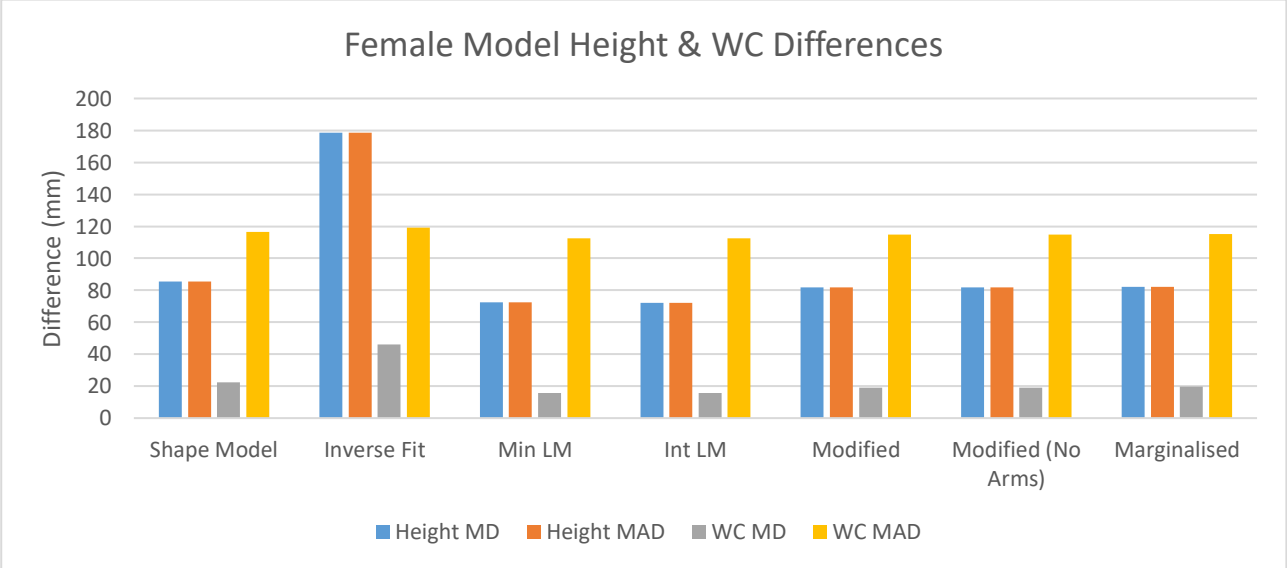

Figure 7.20: Female model height and WC differences for MPI-Faust test data.

Figure 7.21 below shows the volume MD and MAD values. The MAD values were larger indicating an error due to under- and overestimation with a skew towards underestimation due to the negative MD. The best performing approach was the intermediate landmark model with a MAD of 10.75 l. The worst performing approach was the inverse fit.

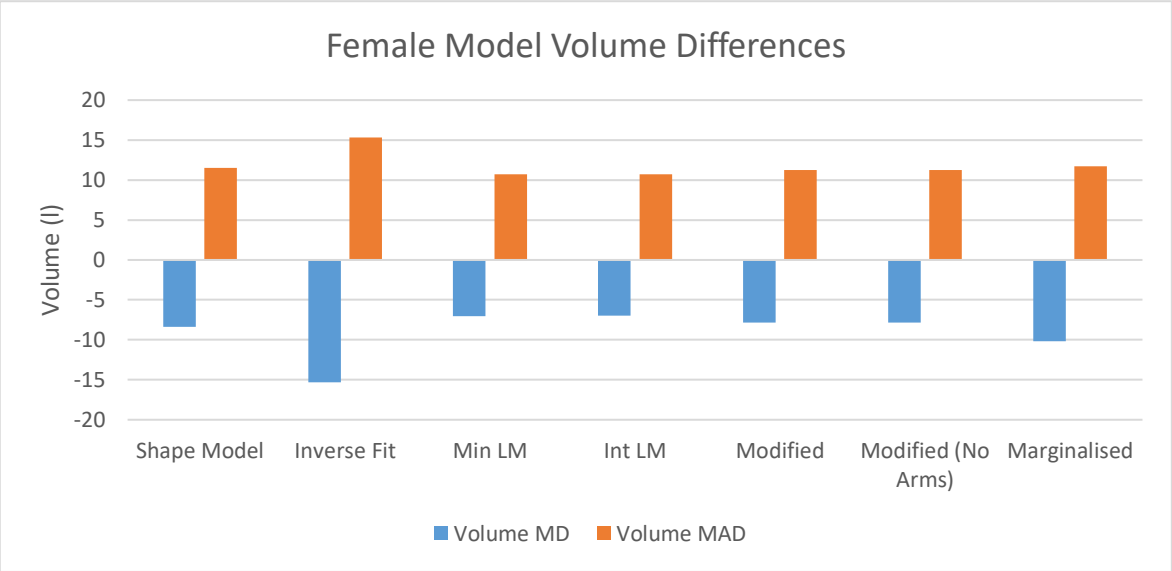

Figure 7.21: Female model volume differences for MPI-Faust test data.

7.5.2 Male Model

This section presents the results of the male model reconstruction. In addition to the measurements, the human-like quality of the reconstructions was visually inspected.

i. Qualitative Assessment

Figure 7.22 below shows the mean mesh original mesh, reconstructed mesh, and an overlap of the original and reconstructed meshes for a given mesh from the male test data. The meshes shown are those from the shape model method. The reconstructed meshes are visually consistent with the shape of the human body. Similarly to the female model, the pose differences in the arms between the original and reconstruction are clear.

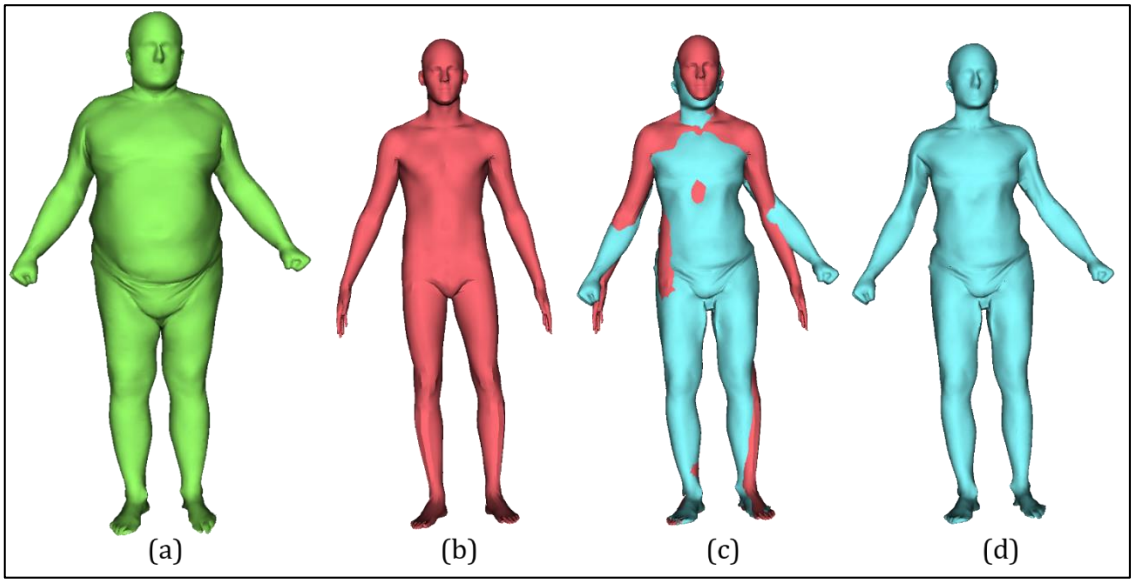

Figure 7.22: The model mean mesh (a), original mesh (b), the reconstructed mesh (d), and an overlap of the original and reconstruction (c) are shown for a MPI-FAUST male test mesh using the shape model method.

ii. Surface Distances

Figure 7.23 below shows the surface-to-surface distances. The inverse fitting approach had the largest distances with 32.73 mm for the surface-to-surface distance per vertex and 62.94 mm for the modified Hausdorff distance. The modified model without arms had the smallest distances with 21.41 mm for the

surface-to-surface distance per vertex and 23.65 mm for the modified Hausdorff distance. Of the models with arms, the intermediate landmark model had the smallest distances with 26.70 mm for the surface-to-surface distance per vertex and 40.99 mm for the modified Hausdorff distance.

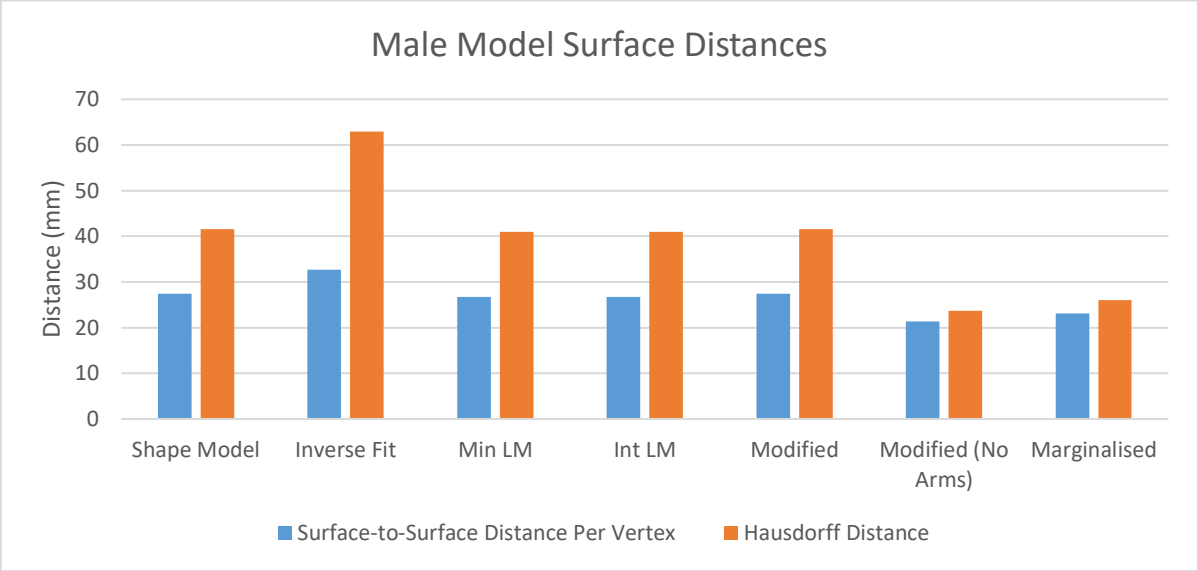

Figure 7.23: Male model surface-to-surface distances for MPI-FAUST test data.

Figure 7.24 and Figure 7.25 below show heatmaps for the best and worst test results from the shape model for MPI-Faust test data. The heatmap shows the surface distance for each vertex with colour correlating to the scale displayed. For the best result, most of the errors do not exceed 100 mm. Those that do and are on the forearms. There is very little error in the trunk and legs. For the worst result, the errors exceed 100 mm with extremely prominent errors in the arms and the lower legs. There are prominent errors on the trunk in contrast to the best result.

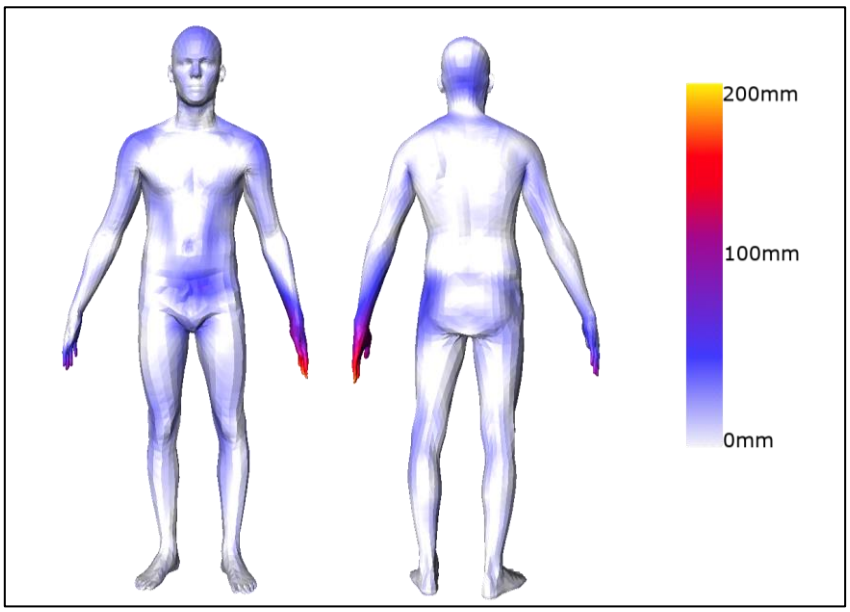

Figure 7.24: Male model best reconstruction heatmap for MPI-FAUST test data.

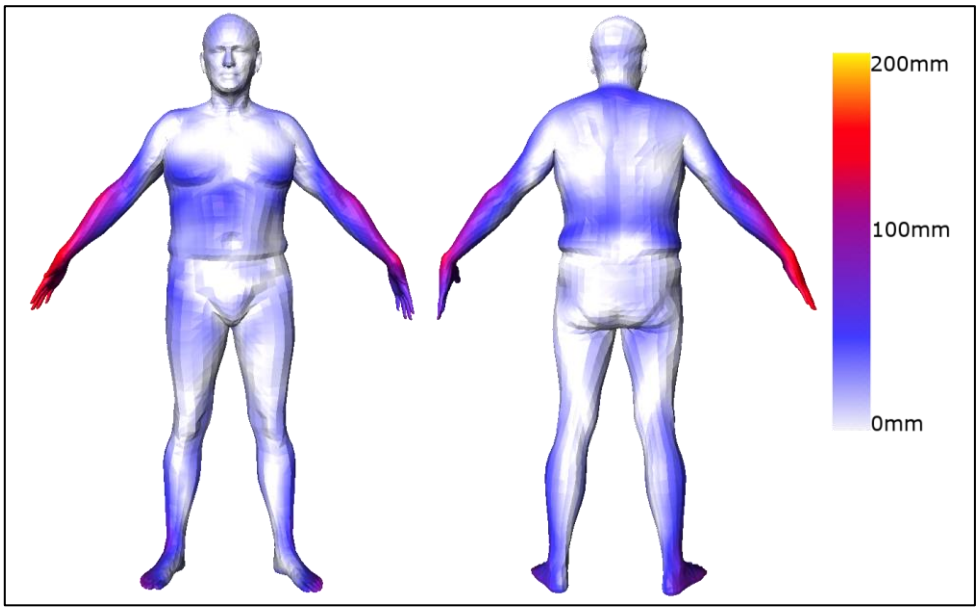

Figure 7.25: Male model worst reconstruction heatmap for MPI-FAUST test data.

iii. Body Measurements

Figure 7.26 below shows the MD and MAD for height and WC. For height, the MD was smaller than the MAD for all approaches bar the inverse fit. This indicates errors due to under- and overestimation. For the shape model, modified, and no arm approaches, the error skewed towards overestimation. For the minimal and intermediate landmark approaches, the error skewed towards underestimation. For WC, the MD was negative and the MAD large indicating large errors due to under- and overestimation with a skew towards underestimation. The best performing approaches for height were the shape model and the modified models with MADs of 41.06 mm. The best approach for WC was the inverse fit model with a MAD of 107.40 mm. The worst approach for height was the inverse fit approach and the worst for WC was shape model.

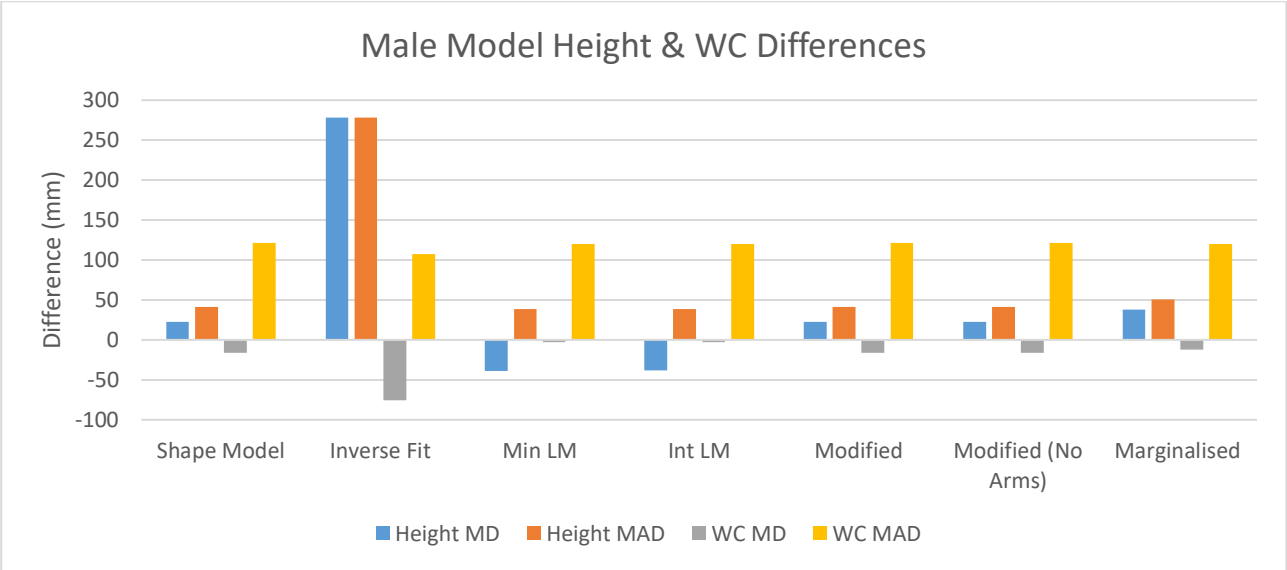

Figure 7.26: Male model height and WC differences for MPI-FAUST test data.

Figure 7.27 below shows the volume MD and MAD values. The MAD values were larger indicating an error due to under- and overestimation with a skew towards underestimation due to the negative MD. The best approach was the minimal landmark model with a MAD of 10.24 l. The worst performing approach was the inverse fit.

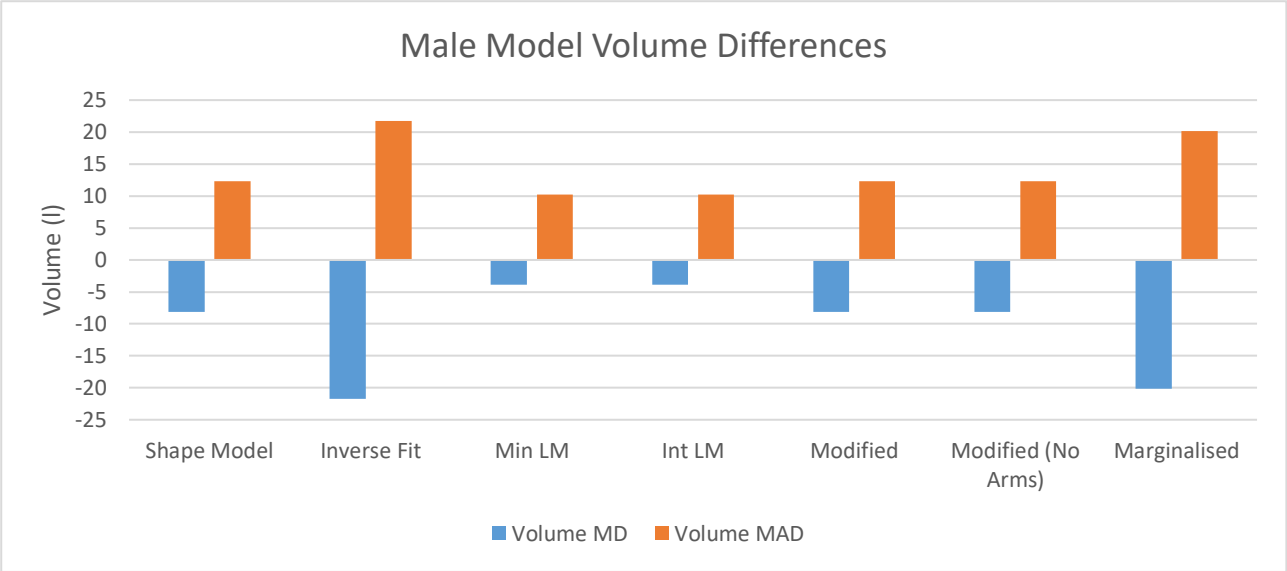

Figure 7.27: Male model volume differences for MPI-FAUST test data.

7.6 Chapter Discussion

7.6.1 Image Landmarks

As seen in section 5, the image landmarks are shown to be placed reliably. Nonetheless, manual landmarking is time consuming and the lack of a ground truth is a limitation. Thus, automatic landmarking is recommended. This can be done using an autoencoder framework (Zhang et al., 2018) or a manually placed silhouette can be used to guide an automatic landmarking system as demonstrated previously in a smartphone application (Song et al., 2018).

7.6.2 Landmark Processing

The current landmark scaling approach is dependent on the real height being known. If it is unknown, a different approach will have to be applied. The first is to use a phantom of known height. Once the phantom's pixel height is known, the same scaling approach can be used. A second approach relies on the subject distance and camera parameters. The real height can be calculated as follows (Young, 2015):

$$\boldsymbol{real\ height}\ (\boldsymbol{mm}) = \frac{\boldsymbol{subject\ distance}\ (\boldsymbol{mm}) \times \boldsymbol{object\ height}\ (\boldsymbol{px}) \times \boldsymbol{sensor\ height}\ (\boldsymbol{mm})}{\boldsymbol{focal\ length}\ (\boldsymbol{mm}) \times \boldsymbol{image\ height}\ (\boldsymbol{px})} \quad (7.6)$$

This approach relies on the subject distance being known. The distance can be set as part of the instructions to use the system. The object height is read from the pixel distance of the landmarks. The sensor height and focal length are read from the camera parameters. This information may be including in the Exchangeable Image File format (EXIF) (Technical Standardization Committee on AV & IT Storage Systems and Equipment, 2002) data of the image but can also be read from a smartphone if using an app. An additional advantage of a smartphone app is the ability to correct for camera orientation issues by reading accelerometer data as demonstrated previously (Ballester et al., 2016).

7.6.3 3D Reconstruction

As can be seen in sections 7.4 and 7.5, the perceptual accuracy of the reconstruction is satisfactory. The reconstructions are recognisable 3D body shapes in a natural pose. However, reconstruction errors can be seen with the reconstructed mesh not completely overlapping with the original mesh. This is true for both the SPRING data and MPI-FAUST data. Part of the lack of overlap is due to pose differences with the differences visibly larger for the MPI-FAUST results. For the male model, the deformations from the mean show the variability contained within the model with there being large visual differences between

the mean and the original and reconstructed meshes. However, the overall accuracy was unsatisfactory when considering surface-to-surface distance per vertex. The modified model without arms performed best across all tests. For the SPRING test data, the errors were less than 15 mm and for the MPI-FAUST data the errors were in the 20 mm range. Of the models with arms, the female intermediate and the male shape model performed best for SPRING test data with errors in the 15 mm range. Of the models with arms, the female intermediate landmark model and the male intermediate landmark model performed best for MPI-FAUST data with errors in the 25 mm range. This is unsatisfactory as the errors are larger than the errors of 2.1 mm and 8 mm encountered in literature (Ballester et al., 2016, Boisvert et al., 2013). Even in the ideal case with the SPRING data, the models performed unsatisfactorily compared to literature.

Based on the surface-to-surface distance per vertex, it is difficult to assess whether the model performs satisfactorily for the intended application of medical anthropometry. However, comparisons to shape models in the literature can assist. Both Boisvert et al. (2013) and Ballester et al. (2016) developed full body shape models and stated that their work may be suitable for garment fitting. The errors in the current study are larger than the errors found by Boisvert et al. (2013) and Ballester et al. (2016) when comparing surface-to-surface distance per vertex. The measurement errors suitable for garment fitting (Song et al., 2018) are larger than those described for medical anthropometry (Gordon et al., 1989, Gordon et al., 2014). The errors found in the current study therefore show the method is neither suitable for garment fitting nor for medical anthropometry.

For body measurements, the best performing models varied with different models performing best for different cases. Regardless, the errors as measured by MAD were above the allowable errors. Additionally, the WC errors were larger than the errors of 40 mm, 18 mm, 22 mm, 19.3 mm seen in literature (Bălan & Black, 2008, Ballester et al., 2016, Song et al., 2018, Song et al., 2016). The height errors were also larger than errors of 10 mm seen in literature (Bălan & Black, 2008, Song et al., 2016). Additionally, the separate assessment of reconstruction using height landmarks also produced errors above the allowable errors and the literature errors when measuring height. As expected, the ideal scenario test cases produced superior results to the generalised test cases. However, the errors are larger than the allowed errors and those seen in literature. There are several potential error sources that extend beyond the idealness of the test case.

As seen in section 5, the landmark positions are a source of error due to inter- and intra-operator error. Furthermore, the lack of correlation between fitting accuracy and the number of landmarks indicates an issue with the landmarks. Theoretically, the number of landmarks and fitting precision should correlate because of the posterior variance. The posterior variance is always smaller than the model variance and is dependent on the number of inputs (Rasmussen, 2003). Thus, inputting more landmarks should reduce the variance and increase reconstruction accuracy. However, that relationship was not seen in the results. If the landmark errors can be made negligible, then increasing the number of landmarks should reduce the error. The method described in 6.4.7 is an example of an automatic method that produces small errors.

The GPMM models only shape differences and does not account for pose differences. The inability to understand pose differences presents a problem when performing 3D reconstruction. Pose differences are interpreted as shape differences and reduce the accuracy of the reconstruction. This can be seen in Figure 7.16 where the tilted head of the original mesh is not replicated in the reconstructed mesh and in Figure 7.22 where the difference in arm pose is clear. These pose issues even appeared with the SPRING results. The meshes are a part of the model data yet Figure 7.4 and Figure 7.10 show pose differences in the arms. The heatmaps also show the inability to interpret pose. For all test cases, the

most prominent errors were in the arms and to a lesser extent the trunk. The arms are again a source of error due to pose differences. This shows the need for a shape and pose model.

There are several methods that model shape and pose. Some methods model them separately (Anguelov et al., 2005b) and others model them jointly (Chen, Liu & Zhang, 2013, Hasler et al., 2009, Loper et al., 2015). Cheng et al. (2018) analysed a variety models that model shape and pose either jointly or separately. They found that the shape and joint errors were similar for each of the models assessed. However, they found the Skinned Multi-Person Linear model (SMPL) (Loper et al., 2015) to be the best performing model.

The SMPL model decomposes shape into identity-dependent shape and nonrigid pose-dependent shape. These components are blended with pose and joint parameters to describe the shape and pose model in a low-dimensional linear manner. It has been applied to 3D reconstruction from 2D images with an automatic 2D joint predictor (Bogo et al., 2016). The surface-to-surface distance per vertex was less than 2.5 mm when considering a known pose. The errors are smaller than those described by Boisvert et al. (2013) and comparable to those described by Ballester et al. (2016). Additionally, the system can cope with an initial unknown pose. The performance of such a system shows the advantages of integrating 2D and 3D information in modelling. Possible additions to the system include attempts to further integrate 2D and 3D prediction. As demonstrated by Kanazawa et al. (2018), a convolutional image encoder is combined with SMPL and a discriminator network in a regressive manner. The regression module seeks 3D parameters that best describe the 2D image when considering pose, shape, and camera position. These are taken as SMPL parameters and are sent to the discriminator. Approved parameters are then used for mesh reconstruction. The advantage of this approach is the ability to train on unpaired annotated 2D images and annotated 3D meshes. Omran et al. (2018) apply a convolutional neural network (CNN) to process and segment images into 12 parts. They then use SMPL to obtain a pose-defining projection to 2D points whose loss is propagated back into the network. These systems show the possibilities of using convolutional methods to better model 2D information with existing 3D modelling frameworks and represent a potential path to better 3D reconstructions.

8. Discussion & Conclusion

The goal of this research was to develop a Gaussian process morphable model (GPMM) for 3D body reconstruction from 2D images that can measure body volume (BV), height, and waist circumference (WC). The GPMM development was successful. However, in testing the quality of the models it was found that the models showed less generalisation and specificity compared to those in literature (Loper et al., 2015, Pishchulin et al., 2017). Nonetheless, the models produced shapes that were consistent with the human body. However, the accuracy of the reconstructions by the model and the accuracy of some of the measurements were unsatisfactory.

8.1 Body Measurements

The methods implemented for volume and height showed good performance. The volume differences were less than 0.5%. The height differences were within the allowed MAD value. Thus, the methods used to measure height and volume are suitable for use in a future system. The WC methods were unsuccessful. The test results showed errors larger than the allowed MAD value. A potential source of error are landmarks which were shown to be reliably placed but less precise in their positions. This lack of precision effects the measurements and reconstruction (Kouchi & Mochimaru, 2011).

The lack of accuracy for some of the measurements presents a challenge towards a full implementation. The list of body measurements extends beyond the scope of those presented in this research. Other measurements used for health assessment include hip circumference, arm girth, and thigh girth amongst others (Heymsfield et al., 2018, Jaeschke, Steinbrecher & Pischon, 2015, World Health Organization, 2000). The list of possible dimensions has extended to 132 in anthropometric studies (Gordon et al., 1989). Increasing the number of dimensions measured is an important part towards a full solution and can increase usage in other industries such as the fashion industry (Bălan & Black, 2008, Song et al., 2018).

8.2 Reconstruction Accuracy

The reconstruction errors were larger than those seen in literature for both the ideal and generalised scenarios. Landmarks have already been identified as a source of error in prior sections. Additionally, there was no correlation between reconstruction errors and the number of landmarks. This is further evidence of landmark errors. Another source of error is the inability to interpret pose differences. The model used only considers shape and the inability to process pose can be clearly seen in the generalised scenario where pose differences contributed to the error. The results show the limitations of models that only consider shape. The models from literature perform well but they are limited in their usability as they rely on a person being in a fixed position to produce silhouettes for reconstruction (Ballester et al., 2016, Boisvert et al., 2013). A better approach is through models that consider 2D joint information along with 3D shape and pose information (Kanazawa et al., 2018, Omran et al., 2018). These approaches, that make use of convolutional methods, present a possible path for better 3D reconstructions in real-world conditions. Improved reconstruction will also increase the areas where the system can be applied. This includes areas such as shape analysis and biometric identification (Hasler et al., 2009, Heimann & Meinzer, 2009, Pishchulin et al., 2017). The increased functionality is particularly relevant for resource constrained environments.

8.3 Limitations & Future Work

The main limitations identified relate to modelling pose and landmark accuracy. The major recommendations for future work aim to address these limitations. The first recommendation is to use

a method that models pose and shape jointly. This can be further extended by using convolutional methods to incorporate 2D joint and 3D shape information through new or existing models. The second recommendation is to make use of automatic 2D, and 3D landmarking methods to reduce error and increase the number of landmarks. Automatic landmarking methods show better precision (Xiaohui et al., 2018). This should result in better measurements, reconstructions, and improve the quality of information provided by the system. The relevant measurements that can be performed using adaptations of the current set of algorithms should also be investigated.

Regarding the pathway towards a smartphone app, there a few recommendations. These relate to image acquisition, landmarking, and other issues as well. The first recommendation is to implement a scaling method that incorporates camera parameter information. This will remove the need to manually input height for reconstruction. The second is to incorporate orientation sensor data to correct for distortions due to a titled phone when taking the picture. This has been demonstrated previously (Ballester et al., 2016) and will contribute towards improving the quality of the image data.

Regarding landmarking, the aforementioned landmarking methods can be used, provided the image is transported to a central server. However, privacy considerations would have to be addressed. An alternative is to make use of silhouettes to either guide a user to manually landmark the images (Ballester et al., 2016) or to make use of the silhouette directly in reconstruction (Boisvert et al., 2013). The limitation with the latter method is that changes will have to be made to the reconstruction algorithm. Additional considerations for an app include data security, data transport, local versus offsite processing, user interface design, and smartphone specification requirements. The last point is particularly relevant for less-resourced settings as the specifications of the smartphones commonly in use may be lower than those in well-resourced settings.

8.4 Outputs

This project produced the following outputs:

- Database compiled from multiple sources.
- Female and male human body shape models.
- Reusable code developed for future use and available online[8].

[8] https://github.com/KZM26/body-volume-application

References

3D Systems. 2018. *Sense 3D Scanner | Order My Sense | 3D Systems*. Available: https://www.3dsystems.com/3d-scanners/sense-scanner [2018, 4 October].

Abbott, P. 2008. On the Perimeter of an Ellipse. *Mathematica Journal.* 11(2):172. DOI:10.3888/tmj.11.2-4.

Abramowitz, M.K., Hall, C.B., Amodu, A., Sharma, D., Androga, L. & Hawkins, M. 2018. Muscle mass, BMI, and mortality among adults in the United States: A population-based cohort study. *PloS One.* 13(4):e0194697. DOI:10.1371/journal.pone.0194697.

Adler, C., Steinbrecher, A., Jaeschke, L., Mähler, A., Boschmann, M., Jeran, S. & Pischon, T. 2017. Validity and reliability of total body volume and relative body fat mass from a 3-dimensional photonic body surface scanner. *PloS One.* 12(7):e0180201. DOI:10.1371/journal.pone.0180201.

Aldrian, O. & Smith, W.A.P. 2013. Inverse rendering of faces with a 3D morphable model. *IEEE Transactions on Pattern Analysis and Machine Intelligence.* 35(5):1080-1093. DOI:10.1109/TPAMI.2012.206.

Allen, J.K., Stephens, J., Dennison Himmelfarb, C.R., Stewart, K.J. & Hauck, S. 2013. Randomized controlled pilot study testing use of smartphone technology for obesity treatment. *Journal of Obesity.* 2013:7. DOI:10.1155/2013/151597.

Almvist, G. & Berndt, B. 1988. Gauss, Landen, Ramanujan, the Arithmetic-Geometric Mean, Ellipses, π, and the Ladies Diary. *The American Mathematical Monthly.* 95(7):585-608. DOI:10.1080/00029890.1988.11972055.

Altman, D.G. & Bland, J.M. 1983. Measurement in medicine: the analysis of method comparison studies. *Journal of the Royal Statistical Society: Series D (The Statistician).* 32(3):307-317. DOI:10.2307/2987937.

Amazon. 2018a. *Amazon - XYZprinting Handheld 3D Scanner 1.0 Pro*. Available: https://tinyurl.com/vtfnxyb [2018, 4 Oct].

Amazon. 2018b. *Amazon - Occipital Wireless Other for Apple 10.5 Inch Ipad Pro - Dark Grey* Available: https://tinyurl.com/u2ruw8d [2018, 4 October].

Amazon. 2018c. *Amazon - Xbox One Kinect Sensor*. Available: https://tinyurl.com/qrkdum4 [2018, 4 October].

Amberg, B., Romdhani, S. & Vetter, T. 2007. Optimal step nonrigid ICP algorithms for surface registration. *IEEE Conference on Computer Vision and Pattern Recognition (CVPR)*. Minneapolis, MN, 2007. 1-8.

Amfucla. 2017. *BMI chart*. Available: https://upload.wikimedia.org/wikipedia/commons/b/b0/BMI_chart.svg [2018, 7 September].

An, Y., Yi, S., Fitzpatrick, A., Gupta, V., Prak, P.R., Oum, S. & LoGerfo, J.P. 2013. Appropriate body mass index and waist circumference cutoff for overweight and central obesity among adults in Cambodia. *PloS One.* 8(10):e77897. DOI:10.1371/journal.pone.0077897.

Anguelov, D., Srinivasan, P., Pang, H.-C., Koller, D., Thrun, S. & Davis, J. 2005a. The correlated correspondence algorithm for unsupervised registration of nonrigid surfaces. In *Advances in Neural Information Processing Systems.* L.K. Saul, Y. Weiss and L. Bottou, Eds. Vancouver, Canada: MIT Press. 33-40.

Anguelov, D., Srinivasan, P., Koller, D., Thrun, S., Rodgers, J. & Davis, J. 2005b. SCAPE: shape completion and animation of people. *ACM Transactions on Graphics (TOG).* 24(3):408-416. DOI:10.1145/1073204.1073207.

Azouz, Z.B., Shu, C. & Mantel, A. Eds. 2006. Automatic locating of anthropometric landmarks on 3D human models. Chapel Hill, NC: IEEE. 750-757.

Bălan, A.O. & Black, M.J. 2008. The naked truth: Estimating body shape under clothing. In *Computer Vision – ECCV 2008.* D. Forsyth, P. Torr and A. Zisserman, Eds. Berlin, Germany: Springer. 15-29.

Ballester, A., Parrilla, E., Piérola, A., Uriel, J., Pérez, C., Piqueras, P., Nácher, B., Vivas, J.A. et al. 2016. Data-driven three-dimensional reconstruction of human bodies using a mobile phone app. *International Journal of the Digital Human.* 1(4):361-388. DOI:10.1504/IJDH.2016.084581.

Bemis, S.P., Micklethwaite, S., Turner, D., James, M.R., Akciz, S., Thiele, S.T. & Bangash, H.A. 2014. Ground-based and UAV-based photogrammetry: A multi-scale, high-resolution mapping tool for structural geology and paleoseismology. *Journal of Structural Geology.* 69(Part A):163-178. DOI:10.1016/j.jsg.2014.10.007.

Besl, P.J. & McKay, N.D. 1992. A method for registration of 3-D shapes. *IEEE Transactions on Pattern Analysis and Machine Intelligence.* 14(2):239-256. DOI:10.1109/34.121791.

Bigaard, J., Spanggaard, I., Thomsen, B.L., Overvad, K. & Tjønneland, A. 2005. Self-reported and technician-measured waist circumferences differ in middle-aged men and women. *The Journal of nutrition.* 135(9):2263-2270. DOI:10.1093/jn/135.9.2263.

Blanz, V. & Vetter, T. 1999. A morphable model for the synthesis of 3D faces. In *Proceedings of the 26th Annual Conference on Computer Graphics and Interactive Techniques.* W. Waggenspack, Ed. New York, NY: ACM Press/Addison-Wesley Publishing Co. 187-194.

Body Volume. 2018. *BVI as a health indicator*. Available: https://tinyurl.com/qn3kq2a [2018, 12 September].

Bogo, F., Romero, J., Loper, M. & Black, M.J. 2014a. *FAUST: Dataset and evaluation for 3D mesh registration.*

Bogo, F., Romero, J., Loper, M. & Black, M.J. 2014b. FAUST: Dataset and evaluation for 3D mesh registration. *IEEE Conference on Computer Vision and Pattern Recognition (CVPR)*. Columbus, OH, 2014b. 3794-3801.

Bogo, F., Kanazawa, A., Lassner, C., Gehler, P., Romero, J. & Black, M.J. 2016. Keep it SMPL: Automatic estimation of 3D human pose and shape from a single image. In *Computer Vision – ECCV 2016.* B. Leibe, J. Matas, N. Sebe and M. Welling, Eds. Cham, Switzerland: Springer. 561-578.

Boisvert, J., Shu, C., Wuhrer, S. & Xi, P. 2013. Three-dimensional human shape inference from silhouettes: reconstruction and validation. *Machine vision and applications.* 24(1):145-157. DOI:10.1007/s00138-011-0353-9.

Bragança, S., Arezes, P.M. & Carvalho, M. 2015. An overview of the current three-dimensional body scanners for anthropometric data collection. In *Occupational Safety and Hygiene III.* P.M. Arezes, J.S. Baptista, M.P. Barroso, P. Carneiro, P. Cordeiro, N. Costa, R.B. Melo, A.S. Miguel et al., Eds. London, United Kingdom: CRC Press. 149-154.

Brownell, K.D. & Walsh, B.T. 2017. *Eating disorders and obesity, third edition: A comprehensive handbook.* New York, NY: Guilford Publications. Available: https://books.google.co.za/books?id=b85EDwAAQBAJ.

CFCF. 2014. *Anatomical Planes.* Wikimedia,.

Chen, Y., Liu, Z. & Zhang, Z. 2013. Tensor-based human body modeling. *IEEE Conference on Computer Vision and Pattern Recognition (CVPR)*. Portland, OR, 2013. 105-112.

Cheng, Z.-Q., Chen, Y., Martin, R.R., Wu, T. & Song, Z. 2018. Parametric modeling of 3D human body shape—A survey. *Computers & Graphics.* 71:88-100. DOI:10.1016/j.cag.2017.11.008.

Chin, S.O., Keum, C., Woo, J., Park, J., Choi, H.J., Woo, J.-t. & Rhee, S.Y. 2016. Successful weight reduction and maintenance by using a smartphone application in those with overweight and obesity. *Scientific Reports.* 6:34563. DOI:10.1038/srep34563.

Clarkson, S., Wheat, J., Heller, B. & Choppin, S. 2016. Assessment of a Microsoft Kinect-based 3D scanning system for taking body segment girth measurements: a comparison to ISAK and ISO standards. *Journal of Sports Sciences.* 34(11):1006-1014. DOI:10.1080/02640414.2015.1085075.

Cootes, T.F., Taylor, C.J., Cooper, D.H. & Graham, J. 1995. Active shape models-their training and application. *Computer vision and image understanding.* 61(1):38-59. DOI:10.1006/cviu.1995.1004.

Creative Commons. 2009. *Creative Commons Attribution-Share Alike 3.0 Unported.*

Daanen, H.A.M. & van de Water, G.J. 1998. Whole body scanners. *Displays.* 19(3):111-120. DOI:10.1016/S0141-9382(98)00034-1.

Daanen, H.A.M. & ter Haar, F.B. 2013. 3D whole body scanners revisited. *Displays.* 34(4):270-275. DOI:10.1016/j.displa.2013.08.011.

Dai, H., Pears, N., Smith, W. & Duncan, C. Eds. 2017. A 3d morphable model of craniofacial shape and texture variation. Venice, Italy: IEEE. 3085-3093.

Davies, R.H. 2002. Learning shape: optimal models for analysing natural variability. University of Manchester.

de Wilde, J.A., van Dommelen, P. & Middelkoop, B.J.C. 2013. Appropriate body mass index cut-offs to determine thinness, overweight and obesity in South Asian children in the Netherlands. *PloS One.* 8(12):e82822. DOI:10.1371/journal.pone.0082822.

Dee, A., Kearns, K., O'Neill, C., Sharp, L., Staines, A., O'Dwyer, V., Fitzgerald, S. & Perry, I.J. 2014. The direct and indirect costs of both overweight and obesity: a systematic review. *BMC Research Notes.* 7(1):242-250. DOI:10.1186/1756-0500-7-242.

Dehghan, M. & Merchant, A.T. 2008. Is bioelectrical impedance accurate for use in large epidemiological studies? *Nutrition Journal.* 7(1):26-32. DOI:10.1186/1475-2891-7-26.

Dessery, Y. & Pallari, J. 2018. Measurements agreement between low-cost and high-level handheld 3D scanners to scan the knee for designing a 3D printed knee brace. *PloS One.* 13(1):e0190585. DOI:10.1371/journal.pone.0190585.

Dewit, O., Fuller, N., Fewtrell, M.S., Elia, M. & Wells, J.C.K. 2000. Whole body air displacement plethysmography compared with hydrodensitometry for body composition analysis. *Archives of Disease in Childhood.* 82(2):159-164. DOI:10.1136/adc.82.2.159.

Discovery Limited. 2017. *The Vitality ObeCity Index 2017*. Available: https://tinyurl.com/wthpsjo.

Dryden, I.L. & Mardia, K.V. 2016. *Statistical shape analysis with applications in R.* 2nd. Chichester, United Kingdom: John Wiley & Sons.

Dubuisson, M.-P. & Jain, A.K. 1994. A modified Hausdorff distance for object matching. In *Proceedings of 12th International Conference on Pattern Recognition.* S. Peleg and S. Ullman, Eds. New York, NY: IEEE. 566-568.

Durá-GIl, J.V., Piérola-Orcero, A., Ballester, A., Ruescas-Nicolau, A.V. & Parrilla-Bernabé, E. 2018. *3D body shapes - INKREATE.*

Engel, S. 2012. *Zylindrisches Modell der bioelektrischen Impedanzanalyse BIA*. Available: https://upload.wikimedia.org/wikipedia/commons/d/d1/BIA_Zylindrisches_Modell_pro_toto.jpg [2018, 7 September].

Furukawa, Y. & Hernández, C. 2015. Multi-view stereo: A tutorial. *Foundations and Trends® in Computer Graphics and Vision.* 9(1-2):1-148. DOI:10.1561/0600000052.

GBD Obesity Collaborators. 2017. Health effects of overweight and obesity in 195 countries over 25 years. *New England Journal of Medicine.* 377(1):13-27. DOI:10.1056/NEJMoa1614362.

Gerig, T., Morel-Forster, A., Blumer, C., Egger, B., Lüthi, M., Schönborn, S. & Vetter, T. 2018. Morphable face models-an open framework. *IEEE International Conference on Automatic Face & Gesture Recognition*. Xi'an, China, 2018. 75-82.

Gordon, C.C., Churchill, T., Clauser, C.E., Bradtmiller, B. & McConville, J.T. 1989. *Anthropometric survey of US army personnel: methods and summary statistics 1988*. Available: https://apps.dtic.mil/docs/citations/ADA225094.

Gordon, C.C., Blackwell, C.L., Bradtmiller, B., Parham, J.L., Barrientos, P., Paquette, S.P., Corner, B.D., Carson, J.M. et al. 2014. *2012 Anthropometric survey of US Army personnel: Methods and summary statistics*. Available: https://apps.dtic.mil/docs/citations/ADA611869.

Gower, J.C. 1975. Generalized procrustes analysis. *Psychometrika.* 40(1):33-51. DOI:10.1007/BF02291478.

Graphics and Vision Research Group University of Basel. 2017. *The marginalisation property - Statistical Shape Modelling.*

Graphics and Vision Research Group University of Basel. 2018. *Github - unibas-gravis/scalismo: Scalable Image Analysis and Shape Modelling*. Available: https://github.com/unibas-gravis/scalismo [2018, 11 October].

Graphics and Vision Research Group University of Basel. 2019. *Github - unibas-gravis/landmark-clicker: A landmark clicker for 2d images. The clicked landmarks are in the format of scalismo-faces*. Available: https://github.com/unibas-gravis/landmarks-clicker [2019, 11 February].

GSMA Intelligence. 2017a. *Accelerating affordable smartphone ownership in emerging markets*. Available: https://tinyurl.com/y9xhouvx.

GSMA Intelligence. 2017b. *Global Mobile Trends 2017*. Available: https://tinyurl.com/rpa8hcb.

Gulliford, C. 2006. *Air Force fosters worldwide anthropometry resources*. Available: https://tinyurl.com/ufbdjly [2018, 14 September].

Haehnel, D., Thrun, S. & Burgard, W. 2003. An extension of the ICP algorithm for modeling nonrigid objects with mobile robots. In *Proceedings of the 18th International Joint Conference on Artificial Intelligence.* D. Hahnel, S. Thrun and W. Burgard, Eds. San Francisco, CA: Morgan Kaufmann Publishers Inc. 915-920.

Häming, K. & Peters, G. 2010. The structure-from-motion reconstruction pipeline–a survey with focus on short image sequences. *Kybernetika.* 46(5):926-937. Available: https://www.kybernetika.cz/.

Han, H., Nam, Y. & Choi, K. 2010. Comparative analysis of 3D body scan measurements and manual measurements of size Korea adult females. *International Journal of Industrial Ergonomics.* 40(5):530-540.

Han, J., Shao, L., Xu, D. & Shotton, J. 2013. Enhanced computer vision with microsoft kinect sensor: A review. *IEEE Transactions on Cybernetics.* 43(5):1318-1334. DOI:10.1109/TCYB.2013.2265378.

Hanavan Jr, E. 1964. *A mathematical model of the human body*. Available: https://apps.dtic.mil/docs/citations/AD0608463.

Hart, P., Nilsson, N. & Raphael, B. 1968. A Formal Basis for the Heuristic Determination of Minimum Cost Paths. *IEEE Transactions on Systems Science and Cybernetics.* 4(2):100-107. DOI:10.1109/TSSC.1968.300136.

Hasler, N., Stoll, C., Sunkel, M., Rosenhahn, B. & Seidel, H.-P. 2009. A statistical model of human pose and body shape. *Conference of the Eurographics Association*. München, Germany, 2009. 337-346.

Hastings, W.K. 1970. Monte Carlo sampling methods using Markov chains and their applications. *Biometrika.* 57(1):97-109. DOI:10.1093/biomet/57.1.97.

Heimann, T. & Meinzer, H.-P. 2009. Statistical shape models for 3D medical image segmentation: a review. *Medical Image Analysis.* 13(4):543-563. DOI:10.1016/j.media.2009.05.004.

Heymsfield, S.B., Bourgeois, B., Ng, B.K., Sommer, M.J., Li, X. & Shepherd, J.A. 2018. Digital anthropometry: a critical review. *European Journal of Clinical Nutrition.* 72(5):680-687. DOI:10.1038/s41430-018-0145-7.

Hudson, R.G. & Lipka, J. 1917. *A manual of mathematics.* London, United Kingdom: John Wiley & Sons.

International Organization for Standardization. 2010. *ISO 20685:2010*. Available: https://www.iso.org/standard/54909.html Geneva, Switzerland: International Organization for Standardization.

International Organization for Standardization. 2016. *ISO 18825-2:2016*. Available: https://www.iso.org/standard/63494.html Geneva, Switzerland: International Organization for Standardization.

Jaeschke, L., Steinbrecher, A. & Pischon, T. 2015. Measurement of waist and hip circumference with a body surface scanner: feasibility, validity, reliability, and correlations with markers of the metabolic syndrome. *PloS One.* 10(3):e0119430. DOI:10.1371/journal.pone.0119430.

Jain, A., Thormählen, T., Seidel, H.-P. & Theobalt, C. 2010. Moviereshape: Tracking and reshaping of humans in videos. *ACM Transactions on Graphics (TOG).* 29(6):148. DOI:10.1145/1882261.1866174.

Janssen, I., Katzmarzyk, P.T. & Ross, R. 2004. Waist circumference and not body mass index explains obesity-related health risk. *The American Journal of Clinical Nutrition.* 79(3):379-384. DOI:10.1093/ajcn/79.3.379.

Kanazawa, A., Black, M.J., Jacobs, D.W. & Malik, J. 2018. End-to-end recovery of human shape and pose. *IEEE Conference on Computer Vision and Pattern Recognition (CVPR)*. Salt Lake City, UT, 2018. 7122-7131.

Karhunen, K. 1946. *Zur spektraltheorie stochastischer prozesse.* Helsinki, Finland: Mathematica-physica.

Kelly, T.L., Berger, N. & Richardson, T.L. 1998. DXA body composition: theory and practice. *Applied Radiation and Isotopes.* 49(5-6):511-513. DOI:10.1016/S0969-8043(97)00226-1.

Knoops, P.G.M., Beaumont, C.A.A., Borghi, A., Rodriguez-Florez, N., Breakey, R.W.F., Rodgers, W., Angullia, F., Jeelani, N.U.O. et al. 2017. Comparison of three-dimensional scanner systems for craniomaxillofacial imaging. *Journal of Plastic, Reconstructive & Aesthetic Surgery.* 70(4):441-449. DOI:10.1016/j.bjps.2016.12.015.

Koepke, N., Zwahlen, M., Wells, J.C., Bender, N., Henneberg, M., Rühli, F.J. & Staub, K. 2017. Comparison of 3D laser-based photonic scans and manual anthropometric measurements of body size and shape in a validation study of 123 young Swiss men. *PeerJ.* 5:e2980. DOI:10.7717/peerj.2980.

Koo, T.K. & Li, M.Y. 2016. A guideline of selecting and reporting intraclass correlation coefficients for reliability research. *Journal of Chiropractic Medicine.* 15(2):155-163. DOI:10.1016/j.jcm.2016.02.012.

Kouchi, M. & Mochimaru, M. 2011. Errors in landmarking and the evaluation of the accuracy of traditional and 3D anthropometry. *Applied Ergonomics.* 42(3):518-527. DOI:10.1016/j.apergo.2010.09.011.

Kyle, U.G., Bosaeus, I., De Lorenzo, A.D., Deurenberg, P., Elia, M., Gómez, J.M., Heitmann, B.L., Kent-Smith, L. et al. 2004a. Bioelectrical impedance analysis—part I: review of principles and methods. *Clinical Nutrition.* 23(5):1226-1243. DOI:10.1016/j.clnu.2004.06.004.

Kyle, U.G., Bosaeus, I., De Lorenzo, A.D., Deurenberg, P., Elia, M., Gómez, J.M., Heitmann, B.L., Kent-Smith, L. et al. 2004b. Bioelectrical impedance analysis—part II: utilization in clinical practice. *Clinical Nutrition.* 23(6):1430-1453. DOI:10.1016/j.clnu.2004.09.012.

Lean, M.E.J., Han, T.S. & Morrison, C.E. 1995. Waist circumference as a measure for indicating need for weight management. *BMJ.* 311(6998):158-161. DOI:10.1136/bmj.311.6998.158.

Lehmann, L.A., Alvarez, R.E., Macovski, A., Brody, W.R., Pelc, N.J., Riederer, S.J. & Hall, A.L. 1981. Generalized image combinations in dual KVP digital radiography. *Medical Physics.* 8(5):659-667. DOI:10.1118/1.595025.

Loève, M. 1955. *Probability theory: Foundations, random sequences.* Toronto, Canada: Van Nostrand.

Loper, M., Mahmood, N., Romero, J., Pons-Moll, G. & Black, M.J. 2015. SMPL: A skinned multi-person linear model. *ACM Transactions on Graphics (TOG).* 34(6):248. DOI:10.1145/2816795.2818013.

Lukaski, H.C., Johnson, P.E., Bolonchuk, W.W. & Lykken, G.I. 1985. Assessment of fat-free mass using bioelectrical impedance measurements of the human body. *The American Journal of Clinical Nutrition.* 41(4):810-817. DOI:10.1093/ajcn/41.4.810.

Lüthi, M., Jud, C. & Vetter, T. 2011. Using landmarks as a deformation prior for hybrid image registration. In *Pattern Recognition.* R. Mester and M. Felsberg, Eds. Berlin, Germany: Springer. 196-205.

Lüthi, M., Jud, C., Gerig, T. & Vetter, T. 2016. Gaussian process morphable models. *ArXiv e-prints.* abs/1603.07254. Available: https://arxiv.org/.

Lüthi, M., Gerig, T., Jud, C. & Vetter, T. 2018. Gaussian process morphable models. *IEEE Transactions on Pattern Analysis and Machine Intelligence.* 40(8):1860-1873. DOI:10.1109/TPAMI.2017.2739743.

McGraw, K.O. & Wong, S.P. 1996. Forming inferences about some intraclass correlation coefficients. *Psychological Methods.* 1(1):30-46. DOI:10.1037/1082-989X.1.1.30.

Medina-Inojosa, J., Somers, V., Jenkins, S., Zundel, J., Johnson, L., Grimes, C. & Lopez-Jimenez, F. 2017. Validation of a white-light 3D body volume scanner to assess body composition. *Obesity: Open Access.* 3(1):13-16. DOI:10.16966/2380-5528.127.

Metropolis, N., Rosenbluth, A.W., Rosenbluth, M.N., Teller, A.H. & Teller, E. 1953. Equation of state calculations by fast computing machines. *The Journal of Chemical Physics.* 21(6):1087-1092. DOI:10.1063/1.1699114.

Mialich, M.S., Sicchieri, J.M.F. & Junior, A.A.J. 2014. Analysis of body composition: a critical review of the use of bioelectrical impedance analysis. *International Journal of Clinical Nutrition.* 2(1):1-10. DOI:10.12691/ijcn-2-1-1.

Microsoft. 2009. *Project Natal Fact Sheet May 09*. Available: https://tinyurl.com/wgatxtq [2018, 31 October].

Muir, T. 1902. Formula for the Perimeter of an Ellipse. *Nature.* 66(1703):174-175. DOI:10.1038/066174c0.

Mutsvangwa, T.E.M., Smit, J., Hoyme, H.E., Kalberg, W., Viljoen, D.L., Meintjes, E.M. & Douglas, T.S. 2009. Design, construction, and testing of a stereo-photogrammetric tool for the diagnosis of fetal alcohol syndrome in infants. *IEEE Transactions on Medical Imaging.* 28(9):1448-1458. DOI:10.1109/TMI.2009.2017375.

Nyström, E.J. 1930. Über die praktische auflösung von integralgleichungen mit anwendungen auf randwertaufgaben. *Acta Mathematica.* 54(1):185-204. DOI:10.1007/BF02547521.

Odersky, M., Altherr, P., Cremet, V., Emir, B., Maneth, S., Micheloud, S., Mihaylov, N., Schinz, M. et al. 2004. *An overview of the Scala programming language*. Available: https://tinyurl.com/t9degk9.

OECD. 2018. PPPs and exchange rates. *OECD National Accounts Statistics (database).* 10.1787/data-00004-en[26 July 2018].

Olver, F.W.J., Lozier, D.W., Boisvert, R.F. & Clark, C.W. 2010. *NIST handbook of mathematical functions.* New York, NY: Cambridge University Press.

Omran, M., Lassner, C., Pons-Moll, G., Gehler, P. & Schiele, B. 2018. Neural body fitting: Unifying deep learning and model based human pose and shape estimation. *International Conference on 3D Vision*. Verona, Italy, 2018. 484-494.

Pishchulin, L., Wuhrer, S., Helten, T., Theobalt, C. & Schiele, B. 2017. Building statistical shape spaces for 3d human modeling. *Pattern Recognition.* 67:276-286. DOI:10.1016/j.patcog.2017.02.018.

Pishchulin, L., Insafutdinov, E., Tang, S., Andres, B., Andriluka, M., Gehler, P.V. & Schiele, B. Eds. 2016. Deepcut: Joint subset partition and labeling for multi person pose estimation. 4929-4937.

Plank, L.D. 2005. Dual-energy X-ray absorptiometry and body composition. *Current Opinion in Clinical Nutrition and Metabolic Care.* 8(3):305-309. DOI:10.1097/01.mco.0000165010.31826.3d.

Ploumpis, S., Ververas, E., O'Sullivan, E., Moschoglou, S., Wang, H., Pears, N., Smith, W., Gecer, B. et al. 2020. Towards a complete 3D morphable model of the human head. *IEEE Transactions on Pattern Analysis and Machine Intelligence (Early Access).* 1(1). DOI:10.1109/TPAMI.2020.2991150.

Plourde, G. & Prud'homme, D. 2012. Managing obesity in adults in primary care. *Canadian Medical Association Journal.* 184(9):1039-1044. DOI:10.1503/cmaj.111640.

Poushter, J., Bishop, C. & Chwe, H. 2018. *Social media use continues to rise in developing countries but plateaus across developed ones*. Available: https://tinyurl.com/tp88xau.

Prentice, A.M. & Jebb, S.A. 2001. Beyond body mass index. *Obesity Reviews.* 2(3):141-147. DOI:10.1046/j.1467-789x.2001.00031.x.

Prior, B.M., Cureton, K.J., M., M.C., M., E.E., Sloniger, M.A., Michael, S. & D., L.R. 1997. In vivo validation of whole body composition estimates from dual-energy X-ray absorptiometry. *Journal of Applied Physiology.* 83(2):623-630. DOI:10.1152/jappl.1997.83.2.623.

Prospective Studies Collaboration. 2009. Body-mass index and cause-specific mortality in 900 000 adults: collaborative analyses of 57 prospective studies. *The Lancet.* 373(9669):1083-1096. DOI:10.1016/S0140-6736(09)60318-4.

Ramanujan, S. 1957. *Notebooks of Srinivasa Ramanujan.* Berlin, Germany: Springer.

Rasmussen, C.E. 2003. Gaussian processes in machine learning. In *Advanced Lectures on Machine Learning.* O. Bousquet, U. von Luxburg and G. Rätsch, Eds. Berlin, Germany: Springer. 63-71.

Red Blob Games. 2014. *Implementation of A**. Available: https://tinyurl.com/y7rfc75u [2019, 1 July].

Renehan, A.G., Tyson, M., Egger, M., Heller, R.F. & Zwahlen, M. 2008. Body-mass index and incidence of cancer: a systematic review and meta-analysis of prospective observational studies. *The Lancet.* 371(9612):569-578. DOI:10.1016/S0140-6736(08)60269-X.

Robinette, K.M., Blackwell, S., Daanen, H., Boehmer, M. & Fleming, S. 2002a. *Civilian American and European Surface Anthropometry Resource (CAESAR), Final Report. Volume 1. Summary*.

Robinette, K.M., Blackwell, S., Daanen, H.A.M., Boehmer, M., Fleming, S., Brill, T., Hoeferlin, D. & Burnsides, D. 2002b. *Civilian American and European Surface Anthropometry Resource (CAESAR) Final Report, Vol. II: Description*. Available: https://apps.dtic.mil/docs/citations/ADA406704.

Samsung. 2019. *24" LED Monitor S24E390HL with a Slim narrow bezel | LS24E390HL/XA | Samsung Africa*. Available: https://www.samsung.com/africa_en/monitors/led-se390/ [2019, 23 September].

Schönborn, S., Egger, B., Morel-Forster, A. & Vetter, T. 2017. Markov chain monte carlo for automated face image analysis. *International Journal of Computer Vision.* 123(2):160-183. DOI:10.1007/s11263-016-0967-5.

Select Research. 2018. *Select Research Home*. Available: https://www.selectresearch.com/ [2018, 11 October].

Simenko, J. & Cuk, I. 2016. Reliability and validity of NX-16 3D body scanner. *International journal of Morphology.* 34(4):1506–1514. DOI:10.4067/S0717-95022016000400053.

Smith, N. 2011. *A Dual-energy X-ray absorptiometry (DEXA) scan being administered.* Available: https://upload.wikimedia.org/wikipedia/commons/c/c8/DEXA_scanner_in_use_ALSPAC.jpg [2018, 7 September].

Song, D., Tong, R., Du, J., Zhang, Y. & Jin, Y. 2018. Data-driven 3-D human body customization with a mobile device. *IEEE Access.* 6:27939-27948. DOI:10.1109/ACCESS.2018.2837147.

Song, D., Tong, R., Chang, J., Yang, X., Tang, M. & Zhang, J.J. 2016. 3D Body Shapes Estimation from Dressed-Human Silhouettes. *Pacific Conference on Computer Graphics and Applications*. Okinawa, Japan, 2016. 147-156.

Spencer, E.A., Roddam, A.W. & Key, T.J. 2004. Accuracy of self-reported waist and hip measurements in 4492 EPIC–Oxford participants. *Public Health Nutrition.* 7(6):723-727. DOI:10.1079/PHN2004600.

Spencer, E.A., Appleby, P.N., Davey, G.K. & Key, T.J. 2002. Validity of self-reported height and weight in 4808 EPIC–Oxford participants. *Public Health Nutrition.* 5(4):561-565. DOI:10.1079/PHN2001322.

Styner, M.A., Rajamani, K.T., Nolte, L.-P., Zsemlye, G., Székely, G., Taylor, C.J. & Davies, R.H. 2003. Evaluation of 3D correspondence methods for model building. In *Information Processing in Medical Imaging.* C. Taylor and J.A. Noble, Eds. Berlin, Germany: Springer. 63-75.

Sumner, R.W. & Popović, J. 2004. Deformation transfer for triangle meshes. *ACM Transactions on Graphics (TOG).* 23(3):399-405. DOI:10.1145/1015706.1015736.

Sýkora, S. 2006. Algebraic Approximations of Ellipse Perimeters. *Stan's Library.* I. DOI:10.3247/SL1Math06.004.

Technical Standardization Committee on AV & IT Storage Systems and Equipment. 2002. *Exchangeable image file format for digital still cameras: Exif Version 2.2*. (JEITA CP-3451). Japan Electronics and Information Technology Industries Association.

Tong, J., Zhou, J., Liu, L., Pan, Z. & Yan, H. 2012. Scanning 3d full human bodies using kinects. *IEEE transactions on visualization and computer graphics.* 18(4):643-650. DOI:10.1109/TVCG.2012.56.

Tzou, C.-H.J., Artner, N.M., Pona, I., Hold, A., Placheta, E., Kropatsch, W.G. & Frey, M. 2014. Comparison of three-dimensional surface-imaging systems. *Journal of Plastic, Reconstructive & Aesthetic Surgery.* 67(4):489-497. DOI:10.1016/j.bjps.2014.01.003.

Victor, J., Van Doninck, D., Labey, L., Innocenti, B., Parizel, P.M.P. & Bellemans, J. 2009. How precise can bony landmarks be determined on a CT scan of the knee? *The Knee.* 16(5):358-365. DOI:10.1016/j.knee.2009.01.001.

Weisstein, E.W. 2002. *Point-plane distance*. Available: http://mathworld.wolfram.com/Point-PlaneDistance.html [2019, 2 December].

Wells, J.C.K., Ruto, A.C. & Treleaven, P.C. 2008. Whole-body three-dimensional photonic scanning: a new technique for obesity research and clinical practice. *International Journal of Obesity.* 32(2):232-238. DOI:10.1038/sj.ijo.0803727.

WHO Expert Consultation. 2004. Appropriate body-mass index for Asian populations and its implications for policy and intervention strategies. *The Lancet.* 363(9403):157-163. DOI:10.1016/S0140-6736(03)15268-3.

Wilson, J.P., Mulligan, K., Fan, B., Sherman, J.L., Murphy, E.J., Tai, V.W., Powers, C.L., Marquez, L. et al. 2011. Dual-energy X-ray absorptiometry–based body volume measurement for 4-compartment body composition–. *The American Journal of Clinical Nutrition.* 95(1):25-31. DOI:10.3945/ajcn.111.019273.

Wollner, M., Roberto, B.-B.P., Roncally, S.C.A., Jurandir, N. & Edil, L.S. 2017. Accuracy of the WHO's body mass index cut-off points to measure gender-and age-specific obesity in middle-aged adults living in the city of Rio de Janeiro, Brazil. *Journal of public health research.* 6(2):904-908. DOI:10.4081/jphr.2017.904.

World Health Organization. 2000. *Obesity: preventing and managing the global epidemic*. (9241208945). Available: https://tinyurl.com/srm4gpk.

Xiaohui, T., Xiaoyu, P., Liwen, L. & Qing, X. 2018. Automatic human body feature extraction and personal size measurement. *Journal of Visual Languages & Computing.* 47:9-18. DOI:10.1016/j.jvlc.2018.05.002.

Xiong, X. & De la Torre, F. 2013. Supervised descent method and its applications to face alignment. *IEEE Conference on Computer Vision and Pattern Recognition (CVPR)*. Portland, OR, 2013. 532-539.

Yang, Y., Yu, Y., Zhou, Y., Du, S., Davis, J. & Yang, R. 2014. Semantic parametric reshaping of human body models. *International Conference on 3D Vision*. Tokyo, Japan, 2014. 41-48.

Young, W. 2015. *f/Calc Manual.* Toronto, Canada: Warren Young. Available: http://fcalc.net/manual.pdf.

Yujiri, L., Shoucri, M. & Moffa, P. 2003. Passive millimeter wave imaging. *IEEE microwave magazine.* 4(3):39-50. DOI:10.1109/MMW.2003.1237476.

Yumuk, V., Tsigos, C., Fried, M., Schindler, K., Busetto, L., Micic, D. & Toplak, H. 2015. European guidelines for obesity management in adults. *Obesity facts.* 8(6):402-424. DOI:10.1159/000442721.

Zancanaro, C., Milanese, C., Lovato, C., Sandri, M. & Giachetti, A. 2015. Reliability of three-dimensional photonic scanner anthropometry performed by skilled and naïve operators. *International Journal of Ergonomics.* 5(1):1-11. Available: https://www.cscjournals.org/journals/IJEG/description.php.

Zhang, Y., Guo, Y., Jin, Y., Luo, Y., He, Z. & Lee, H. 2018. Unsupervised discovery of object landmarks as structural representations. *IEEE Conference on Computer Vision and Pattern Recognition (CVPR)*. Salt Lake City, UT, 2018. 2694-2703.

Appendix

Table 11.1 shows a price comparison an average smartphone and selected 3D scanners. The average price is for emerging markets as determined by (GSMA Intelligence, 2017b). The prices for the scanner are based on the manufacturer website or the cheapest price listed on Amazon. Prices have been converted using PPP based on OECD (2018) values. The average smartphone costs the same as a low-end scanner which excludes some equipment.

Table 11.1: Smartphone vs 3D Scanner price comparison

Device Type	Device Name	Cost ($)	Cost (R' PPP)	Reference
Smartphone	Average smartphone	$115	R698.74	(GSMA Intelligence, 2017a)
3D Scanner	Xbox Kinect 3D Scanner (Excludes Adapter)	$105.00	R637.98	(Amazon, 2018c)
3D Scanner	Occipital Structure Sensor (Excludes iPad)	$379.00	R2 302.80	(Amazon, 2018b)
3D Scanner	Sense 3D Scanner	$499.00	R3 031.92	(3D Systems, 2018)
3D Scanner	XYZprinting Full Color Handheld Scanner	$250.00	R1 519.00	(Amazon, 2018a)